Barriers to Tuberculosis Drug Discovery: The Mycobacterial Cell Wall

Caitlin Rosemarie Whittaker

SAMRC/NHLS/UCT Molecular Mycobacteriology Research Unit

Thesis Presented for the Degree of
Doctor of Philosophy
in the Department of Pathology
Faculty of Health Sciences
University of Cape Town
September 2022

DECLARATION

I declare that this thesis is my own unaided work. It is being submitted for the degree of Doctor of Philosophy at the University of Cape Town. It has not been submitted for any degree or examination at any other university.

Signature Signed by candidate Date: 28.09.2022

ABSTRACT

The mycobacterial cell wall is a highly complex macromolecular structure that provides intrinsic resistance to several anti-tuberculosis drugs, making it critical in the success of *Mycobacterium tuberculosis* infection. Multiple layers encapsulate the cell membrane, including arabinogalactan chains and mycolic acids that are covalently bonded to the peptidoglycan layer, resulting in a highly selectively permeable barrier that is unique to this genus. The current treatment for tuberculosis (TB) utilizes antibiotics that weaken the structural integrity of the cell wall to allow easier access for drugs that have intracellular targets. Although this approach is theoretically effective, patient adherence is often poor owing to the lengthy treatment times and negative side effects associated with the multidrug combination regimen. As such, rational drug design to develop more potent, faster-acting anti-TB compounds requires a comprehensive understanding of the composition and functioning of the mycobacterial cell envelope to ensure effective penetration through this barrier. Bioinformatic approaches to compound validation provide a crucial foundation for drug development, but empirical validation of these molecules can present a serious bottleneck in the drug discovery pipeline. Here, we investigated fluorescent click chemistry as a rapid and inexpensive means of ascertaining molecular properties that impact compound permeation of the mycobacterial cell envelope. The variability in permeation of different click-reactive moieties could be rapidly determined using fluorescent read-outs; this, in combination with the availability of a wide array of click-reactive side chains, presents a potentially powerful platform for establishing the properties required by a compound to effectively cross the mycomembrane. Enzymatic degradation of cell wall components further revealed the resilience of mycobacteria as the resulting organisms, spheroplasts, were capable of surviving in the absence of this seemingly essential protective layer. This presents a potentially novel form of intrinsic resistance whereby stripping of the cell wall could allow for tolerance to cell wall active antibiotics, a previously under-appreciated strategy that has been reported in other pathogenic bacteria. Together, these findings highlight the highly dynamic nature of the mycobacterial cell envelope and the need for further investigation into the properties of this structure that allow for such efficient antibiotic evasion.

ACKNOWLEDGEMENTS

Digby, thank you for your unwavering faith in my abilities and for your constant encouragement. This work has presented many setbacks which left me feeling hopeless at times, but your steadfast support and consistent reassurance enabled me to persevere.

Val, I feel very privileged to have worked in your lab and am grateful for your invaluable insights into my work over the years.

In memory of Prof. Egan, a truly spectacular chemist, who taught me how to interpret the chemistry-related aspects of my project and offered instrumental suggestions on how best to proceed with my work.

This work would not have been possible without the financial support provided by the National Health and Laboratory Services (NHSL) grant and funding from the Wellcome Trust through CIDRI-Africa.

To my family, thank you for your support throughout all the tough times and days in which I questioned my place in research. Susan, I would have been lost without your guidance and will be eternally grateful to have had another doctor in the family to whom I could turn in times of need.

Lastly, to my husband Russell, you have stuck by my side through the good and the bad and somehow always knew the right thing to say to calm me down in times of distress. I am so grateful to have had you by my side to provide the encouragement I needed to complete this work.

TABLE OF CONTENTS

LIST OF TABLES

LIST OF FIGURES

CHAPTER 1: INTRODUCTION

MYCOBACTERIAL EVOLUTION

Tuberculosis is a disease that has been present in the human population for millennia and is still a major contributor to annual mortality today[1,2]. Although *Mycobacterium tuberculosis* (*Mtb*) was only identified as causative agent in 1882, estimates indicate co-evolution with the human host for as long as 500 000 years[1,2]. The *Mycobacterium tuberculosis* Complex (MTBC) consists of a group of highly genetically similar mycobacterial species that cause tuberculosis in humans or animals[3]. The MTBC originated in Africa and spread across to other continents during the Neolithic expansion, developing distinct clades associated with different human settlements[4]. The nature of tuberculosis infection is interesting in that it displays characteristics suggestive of its existence in the human population before the Neolithic expansion; namely, slow progression to disease, latency and reactivation[4]. However, tuberculosis has also developed a mode of transmission that is optimal in high density populations, and can have a high death rate when left untreated, these traits reflect a disease that arose after the Neolithic expansion when human populations began living in more crowded settlements and airborne transmission became a highly effective method of spreading disease[4].

The MTBC has undergone many horizontal gene transfer (HGT) events during the course of its evolution, acquiring genes beneficial to its survival in the various environmental niches of its human host and concurrently losing genes deemed dispensable for the lifestyle of an obligate pathogen[5]. Although differing in many ways from other mycobacteria, current species of the MTBC show incredibly low genetic diversity and recent evolution provides little to no evidence of further HGT, rather, adaptations arise solely from nucleotide substitutions and deletions, and chromosomal rearrangements, and even these occur at a curiously low rate[2,5,6]. These findings suggest that the MTBC has co-evolved with its human host for such a great expanse of time that it has a near perfect set of genes for its persistence and survival when it comes to host interactions[7]. This is observed when studying not only the mechanisms by which the pathogen has increased its virulence over time but also the evolution of beneficial traits, such as stress tolerance, that have arisen as a result of adaptive pressures experienced within the host[8,9]. Genetic variation within the host contributes towards the variability of clinical phenotypes associated with TB infection, supporting the hypothesis of co-evolution and providing an evidential basis for the evolutionary adaptations experienced by humans to combat this long-standing pathogen[9]. Geographical isolation of certain *Mtb* lineages suggests co-evolution with specific host populations, whereby other strains exhibit wide-spread distribution, this underscores the importance of host factors and the role they play in determining outcome of disease[10,11]. Further evidence suggests that the heterogeneous nature of *Mtb*,

both within the host and on a phylogeographical basis, is a potent contributor to antibiotic evasion, making the development of a universally effective treatment regimen all but impossible[12].

The highly dynamic properties of the cell envelope allow for effective adaptation to different host environments, through alterations in lipid composition[7]. This variation in cell wall composition can be observed within a single infecting *Mtb* population and across different variants, confounding our understanding of host-pathogen interactions[13]. As the cell wall is exposed to host immune factors, it is vital to fully appreciate its composition within various environmental niches to better understand the route of infection and the inflammatory responses elicited in the host[13]. The exceptionally hydrophobic nature of the mycomembrane further bolsters in-host survival by providing protection in harsh environmental niches and posing a robust barrier to the entry of many anti-TB drugs[7,14]. This intrinsic resistance to antimicrobials is augmented by resistance acquired through chromosomal mutations, which act in one or more of three mechanisms; namely, target modification, antimicrobial inactivation and increased drug efflux[12,14]. Acquired resistance is both complex and dynamic, and likely involves the interplay of several genes as well as epigenetic effects on the organism which, combined, result in robust and efficient evasion of antibiotics and immune factors[7,12]. Of further consequence is the ability of the pathogen to develop resistance mutations with no reduction in fitness or transmissibility, negating the dogma that acquired drug-resistance is accompanied by fitness costs[7,12]. In light of these unique disease traits, it is important to highlight that *Mtb* has developed a long-lasting relationship with humans as both a host and sole reservoir, emphasizing the need for further study of ancient mycobacterial evolution in order to gain clarity about the evolution of *Mtb* pathogenesis[2,6]. Critical to this is a comprehensive grasp of cell wall structure and adaptations that contribute to host-pathogen interactions and facilitate intrinsic resistance to antimicrobials, in addition to the inexorable emergence of acquired resistance following the advent of tuberculosis chemotherapy[13,15].

EVOLUTION OF THE BACTERIAL CELL WALL

Prior to the acquisition of a cell wall, ancestral bacterial cells would have had to possess sufficient functionality in major physiological processes such as DNA replication, translation and central metabolism to ensure robust growth capabilities[16]. In order to accommodate the increased osmotic pressure resultant from such metabolic success, the last common ancestor of bacteria evolved an additional lipid layer to provide resilience in the face of turgor stress[17]. Modern bacteria are classified by their ability to retain the Gram stain; the thick peptidoglycan layer of monoderm bacteria gives them the ability to retain this stain, making them Gram positive; whereby Gram negative cells contain much less peptidoglycan, flanked on

either side by cell wall components, classifying these organisms as diderms[18,19]. The question remains, how did these variations in cell wall composition arise from the prokaryotic progenitor? Most researchers agree that the last common ancestor of the bacterial domain was a monoderm, whereby studying the composition of modern bacterial cell walls provides insufficient information due to observations of near-identical structure in distantly related phyla and a wide diversity of structure in closely related phyla, this theory is largely supported by phylogenetic analyses[16,20,21]. A recent study of phylogenetic classification and rooting of modern bacteria found that with several different modelling approaches, the last common ancestor can be traced back to an organism possessing a single outer layer[20]. Further modelling postulated that gaining an additional outer layer is much easier than losing one, a concept previously supported based on the growth strategy of monoderms being far simpler than that of diderms[16,20]. This hypothesis is intriguing in that it indicates evolution of diderms was not a unique event, but rather an example of convergent evolution. Substantiating this claim are observations of antibiotic selection driving diderm evolution and alternate mechanisms involving endospore formation giving rise to the second cell wall layer[19,22].

Most bacterial species can be classified as canonical monoderms and diderms; however, there are some atypical organisms that do not exhibit conventional cell wall architecture[19,20]. Mollicutes are the sole class belonging to the phylum Tenericutes, pleomorphic organisms that lack a peptidoglycan layer altogether, being defined by their cholesterol-containing triple-layer cell membrane and a unique internal cytoskeleton for maintenance of cell shape[23,24]. These organisms have extremely small genomes in comparison to other bacterial species, having undergone degenerative evolution in response to unknown environmental pressures[23,24]. *Mycoplasma pneumoniae* is a prominent species within this phylum as its role in pneumonia pathogenicity has made it the best known and most widely studied member of Tenericutes[25]. Of particular relevance to this study, was the early concept proposed by Emmy Klieneberger of mycoplasmas representing a cell wall deficient state of known bacterial species[25,26]. Although later classified as a unique class of bacteria, the absence of a cell wall in *Mycoplasma spp*. drove Klieneberger to dedicate her research to proving the existence of cell wall deficient variants, termed L-forms, and several other researchers contributed towards these investigations to elucidate their potential role in pathogenicity[27–31]. These findings are discussed in detail in Chapter 3.

THE MYCOBACTERIAL CELL WALL

Whereas Tenericutes exhibit complete absence of a cell wall, species of the suborder Corynebacterineae (including *Mtb*) possess an additional lipid layer composed of arabinogalactan and mycolic acids (**FIGURE 1.1**)[32]. Members of this group are highly impermeable to a vast array of molecules, exhibiting impermeability to antibiotics such as β-lactams that is up to 1000-fold greater than that of Gram negatives, making it unsurprising that we see pronounced drug resistance of pathogenic species within this suborder[33,34]. A prominent example of this is the intrinsic drug resistance observed in *Mtb* that arises from the tight regulation of cytoplasmic access conferred by this additional layer of encapsulation[35,36]. The *Mtb* bacillus possesses a plasma membrane homologous to that of most other bacteria and is separated from the cell wall by a periplasmic space containing mannose-derived glycophospholipids[37,38]. The periplasm precedes a tripartite layer of covalently linked constituents that form a single macromolecular structure which is referred to here as the cell wall (**FIGURE 1.1**)[37,39]. The innermost layer of the mycobacterial cell wall is composed of cross-linking peptidoglycan chains, various forms of which are present in almost all bacteria[38]. However, the composition of the outer cell wall layers is largely unique to mycobacteria, although, as previously mentioned, is present in a limited number of Corynebacterineae species[32]. The arabinogalactan layer is a highly-branched macromolecule, consisting of arabinose and galactose sugar molecules which form covalent bonds with the peptidoglycan layer and bind mycolic acid chains that extend towards the outer leaflet of the mycomembrane[38]. The outer leaflet of mycolic acids and trehalose conjugates is interspersed with free lipids, providing a uniquely hydrophobic environment which is intrinsically resistant to the entry of a multitude of compounds[32,38]. The cell wall constituents, in combination with the periplasmic space and plasma membrane, form the mycobacterial cell envelope (**FIGURE 1.1**)[33,39]. Furthermore, a capsule composed of proteins and polysaccharides is present in infection models of *Mtb*, this capsule is severely diminished in conventional culture media that contains detergents such as Tween 80, meaning the study of its role in pathogenicity and host survival is of particular difficulty[37]. The wealth of protective layers possessed by mycobacteria makes these organisms all but impenetrable and seemingly inexorable in the face of antibiotic treatment[33,37].

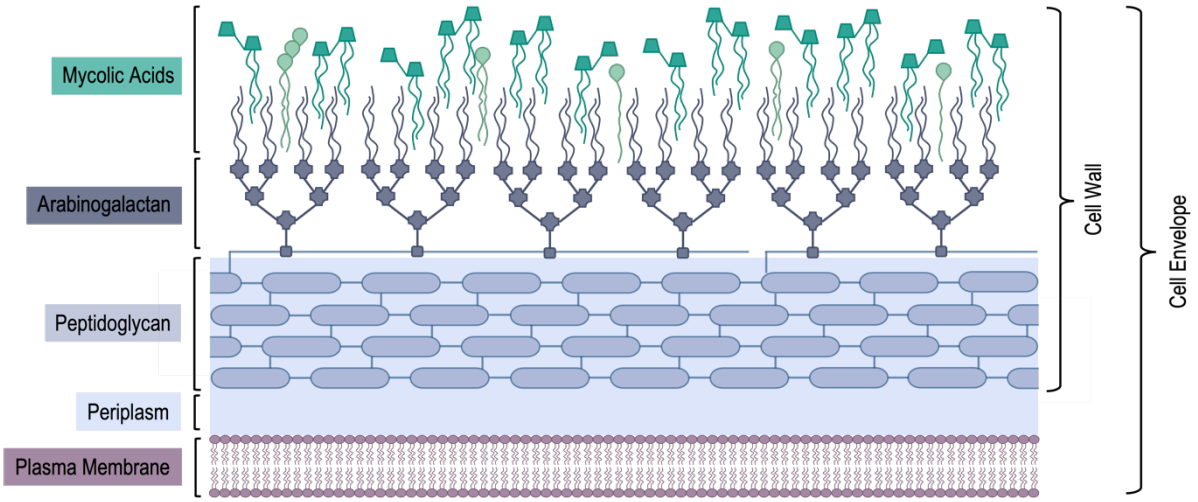

FIGURE 1.1. Model of the mycobacterial cell envelope. The mycolic acid layer (green), arabinogalactan layer (blue-grey), peptidoglycan layer (blue), periplasm (pale blue) and plasma membrane (purple) form the constituents of the mycobacterial cell envelope; whereas the cell wall component of the envelope is comprised of mycolic acids, arabinogalactan and peptidoglycan alone.

PERMEATION

Christopher Lipinski most famously defined the physio-chemical properties required by a molecule to penetrate a membrane in what is known as the Lipinski rule of 5[40,41]. This rule defines the molecular weight, lipophilicity and number of hydrogen donors and acceptors required by a compound to diffuse passively across a cell membrane[40]. Although a very useful starting point to determine drug-likeness of a molecule, the Lipinski rule of 5 should be used in combination with other determining factors. Hopkins and colleagues proposed a system they termed the quantitative estimate of drug-likeness (QED) that they believe to build upon the concept of Lipinski's rules[42]. The QED outlines eight physical properties that confer desirability (including those defined by Lipinski) to determine the drug-likeness of a compound along a continuum scored from zero (no desirable properties) to one (all desirable properties)[40,42]. This method of analysis enhances the ability to differentiate drug from non-drug in a target-specific manner by allowing for weighting of property values relative to the desirability required[40]. Quantitative structure-activity relationship (QSAR) models are widely implemented during drug design to assess the physicochemical properties of lead compounds, several software packages containing various descriptor sets exist, achieving predictive modelling to effectively quantify 3D molecular surface properties[43]. The MycPermCheck bioinformatic tool developed by Sotriffer and colleagues is an example of QSAR software designed to address the specific permeation parameters necessary for passage across the mycobacterial cell envelope. This technique involves collating data from enzyme inhibition assays and bacterial killing efficacy to provide detailed information on permeability[44]. A compound with poor permeation capabilities may exhibit high inhibitory potency in the enzyme-based assay but variable killing efficacy data, providing

vital insight into compounds that display high target affinity but inability to reach the target site effectively[44]. A comprehensive understanding of the physicochemical properties that enhance both entry into host infection sites and across the bacterial cell wall is essential in developing efficacious drug compounds to combat infectious disease[44,45].

THE MYCOBACTERIAL CELL WALL IN INTRINSIC DRUG RESISTANCE

The cell wall of *Mtb* is crucial in its survival as this complex compartment provides a rigid outer layer that maintains cell structure, plays an active role in cell division, protects against unfavourable environmental conditions and is essential for cellular transport and adhesion to host receptors[39,46]. The cell wall makes up to 60% of the lipid content of the bacillus, contributing to a unique abundance in overall lipid content that constitutes 40% of its dry mass[39,46]. This high lipid content plays an important role in the impermeability of mycobacteria to many small molecules, presenting a hydrophobic environment that confers intrinsic resistance to antibiotics[34,39,46].

The substantial barrier to tuberculosis treatment posed by the impermeability of the *Mtb* cell wall is further complicated by the plasticity of the various constituting layers and the temporal and spatial changes an individual cell can undergo, able to exhibit differences in lipid composition of drug-resistant vs. drug-sensitive strains. Phthiocerol dimycocerosate (PDIM) is a potent virulence factor that is only present in pathogenic mycobacteria, this surface lipid is able to mask pathogen-associated molecular patterns (PAMPs) of the cell wall, allowing for highly effective immune evasion[13,33,47]. The combination of virulence factors such as PDIMs and the adaptability of the cell wall to differing host environments are key in establishing infection and show active participation in the development of drug resistance[7]. As the cell wall is the *Mtb* compartment to most frequently encounter host immune cells, it stands to reason that such alterations in lipid profile and expression of virulence factors can significantly impact disease state, making the dynamics of cell wall composition a critical determinant in registering the state of an *Mtb* infection[33].

Beyond the intrinsic drug resistance posed by the architecture of the mycobacterial cell wall, *Mtb* encodes several drug efflux pumps[48,49]. Drug efflux transporters are categorized into five families, two of these, ATP-binding cassette (ABC) transporters and major facilitator superfamily (MFS) transporters, represent a large number of efflux pumps and are considered superfamilies[50]. The other three families are the multidrug and toxic compound extrusion (MATE) family, the small multidrug resistance (SMR) family and the resistance-nodulation-cell division (RND) family[50]. The *Mtb* genome exploits efflux pumps from all five

families, providing an impressive repertoire for intrinsic drug resistance to a wide range of antitubercular compounds[49]. The innate presence and promiscuity of some efflux pumps presents a severe threat to drug discovery, exemplified by the efflux-mediated resistance to Bedaquiline shortly after its approval as the first drug with a novel mechanism of action to be clinically implemented in the past 40 years[51]. The efflux pump accountable for Bedaquiline resistance was MmpL5 (Mycobacterial membrane protein Large 5), a member of the RND family and part of a group of proteins thought to be unique to mycobacteria[49,52]. MmpLs have also been implicated in transport of virulence factors, such as PDIM, and mycolic acids across the plasma membrane, making them potentially promising drug targets[49,53]. It is essential to remain aware of the critical role of efflux pumps in intrinsic, non-specific resistance to drugs, making development of efflux pump inhibitors a promising avenue of rational drug design[48].

The inability of antibiotics to gain access to the interior of bacilli necessitates co-treatment with drugs that permeabilize the mycobacterial cell wall. The current first line of treatment for drug-susceptible TB consists of four antibiotics, two of which target cell wall components[54]. Isoniazid is a prodrug that was discovered and first implemented in 1952; it inhibits mycolic acid synthesis via the InhA enzyme upon activation by a catalase-peroxidase enzyme encoded by *katG*[55,56]. Ethambutol was discovered to have anti-tubercular effects a few years later in 1961; acting on an arabinosyl transferase (EmbB) to inhibit arabinogalactan synthesis and reduce mycolylation sites in the mycomembrane[32,54]. These two drugs impair cell wall integrity to enhance entry of the other two first line drugs – rifampicin and pyrazinamide – which inhibit transcription and translation, respectively[54,57]. Second and third-line drugs exist for treatment of multi-drug resistant (MDR) and extensively drug resistant (XDR) TB, but these treatments do not have high rates of implementation or success and regimens have to be specifically modified for maximal benefit to individual patients, incurring considerable costs and prolonged treatment times[54]. Resistance to frontline drugs is therefore an enduring concern requiring development of more effective drugs that can either target or easily permeate the mycobacterial cell wall.

Moving beyond the obstacle of permeability in the efficacious treatment of TB, the mycobacterial cell wall also undergoes dynamic changes throughout the infective cycle, allowing it to evade host immune responses, tolerate drug treatment and adapt to changing host environments[33]. Mycobacteria undergo asymmetric division, resulting in daughter cells of differing length, growth rate and macromolecular composition, this variability is considered one of the factors that contribute towards the heterogeneous response *Mtb* shows to both host immune factors and antibiotics[33,58]. The elements driving heterogeneity in cell wall structure across a seemingly clonal population of *Mtb* can be both temporal and spatial[33]. Although we are aware of such cell-to-cell variations in cell wall composition, the mechanisms underlying

such alterations remain unclear. Further investigation into the adaptability of the mycolic acid and arabinogalactan layers is crucial in the development of novel drug targets that can impact cell wall stability in this heterogeneous population of infecting *Mtb*, allowing for effective permeation of the cell envelope and easier access for drugs with cytoplasmic targets.

PHENOTYPIC HETEROGENEITY IN MYCOBACTERIA

In recent years, the rapid increase in drug resistance, including multi-drug resistance, in mycobacteria has led to major research efforts into understanding the genetics behind the evasion of antibiotics[59]. However, there are other evasive mechanisms inherent to bacteria that allow for survival in harsh environments[60,61]. These mechanisms were first observed in the 1940s, when bacteria were found to survive extensive exposure to penicillin without developing resistance mutations[62,63]. This survival phenotype - distinguishable from genetic resistance - came to be known as tolerance or persistence[62]. The ambiguity surrounding these two terms is gradually dissipating but conflicting definitions still exist[61,62,64]. Here, I will apply the definitions suggested by Brauner and colleagues in using "tolerance" to refer to the phenomenon occurring at a population level where bacteria are capable of surviving transient exposure to lethal concentrations of bactericidal drugs by entering a slow or non-growing state[62]. Persistence, on the other hand, is a non-heritable, reversible physiological state of non or slow-growth, allowing a subpopulation of bacteria to tolerate lethal concentrations of antibiotic and resuscitate once the environmental stress has been alleviated[61,62]. As such, persistence, which has previously been defined as "heterotolerance" can be considered a subcategory of tolerance[65,66].

The tolerance phenotype of arrested cell division accompanied by filamentation promotes development of genetic resistance mutations[67]. Phenotypic heterogeneity within bacillary populations allows for recrudescence of disease resultant from survival of these few antibiotic tolerant bacteria[68]. Persisters are currently distinguished from viable but non-culturable (VBNC) cells within a bacterial population but these two states of metabolic and/or replicative stasis are considered to be phenotypes along the same 'growth-arrested state' continuum[61,68]. It is hypothesized that this state allows for recalcitrance of *Mtb* infection following antibiotic treatment, making persister and/or VBNC cells potentially important contributors to chronic disease[61]. Although metabolically inactive cells arise in response to environmental stress, they are also capable of arising, in a seemingly stochastic fashion, in nutrient-replete environments suggesting their role in the so-called 'bet-hedging strategy' of bacteria to ensure survival upon unanticipated stress[61,68]. The presence of a persistent subpopulation predating exposure to antibiotics raises interesting questions about the underlying molecular mechanisms involved in generation of this phenotype[64].

Mtb belongs to the family of slow-growing mycobacteria, characteristics accompanying this classification make the bacterium very difficult to treat, and long drug treatment regimens serve to increase the likelihood of the emergence of resistance and persistence[69]. As humans are both the host and only known reservoir of *Mtb*, these slow-grower traits are further strengthened by the adaptations that the bacillus has developed over millennia of co-evolution[70]. As a result, the process of TB infection goes against the classical definition of pathogenicity, that the key mechanism underlying a diseased state is the unrestricted growth of a microorganism[70]. Conversely, *Mtb* does not tend to grow in an uncontrolled manner but rather a complex interaction between host and pathogen, involving metabolic interactions that are still poorly understood results in a disease that is incredibly difficult to treat[70]. These factors allow for multiple infection outcomes that vary immensely in severity, making it difficult to develop a set of criteria for predicting disease progression[69]. Beyond the most obvious pathways down which an infection may go – namely, clearance of the pathogen without disease symptoms or onset of active disease – TB can also cause latent infection, by which the *Mtb* bacilli enter a state of so-called dormancy, making the host an asymptomatic carrier with the potential to develop active disease when conditions within the host undergo certain changes[69]. Mycobacteria are capable of entering a state of metabolic inactivity which leads to growth arrest and allows for survival in unfavourable conditions[69,71]. Elucidating the metabolic changes that *Mtb* undergoes when surviving within the various environmental niches of the host is critical to understanding its pathogenicity.

The life cycle of *Mtb* brings the organism into contact with an exceedingly diverse array of environmental niches that put the bacteria under many different stresses to which they have adapted by evolving a unique set of metabolic pathways[70]. The *Mtb* bacillus is capable of infecting several different types of immune and non-immune cells, where it is faced with a milieu of host defenses to which it has developed several protective metabolic responses[45,70]. Co-catabolism of carbon sources has proven a useful adaptation of *Mtb* in the face of nutrient-depleted environments, enabling the bacterium to utilize several carbon substrates simultaneously to facilitate growth[70]. The bacillus is also capable of surviving in extracellular host compartments such as caseous lesions, wherein nutrient uptake is limited and a state of non-growth is favored to survive within these hypoxic niches[72]. The phenotypic heterogeneity exhibited by *Mtb* to accommodate environmental hardship experienced in different host compartments severely impacts antimicrobial susceptibility, contributing an additional barrier to effective treatment[45,72].

One highly effective mechanism by which the bacilli achieve drug tolerance is by undergoing a thickening of the cell wall. Studies have shown increased production of mycolic acids and peptidoglycan in response

to hypoxia, this increased cell wall mass reduces permeability and can significantly decrease the ability of drugs to enter the bacilli and reach their desired targets[71,73–75]. Conversely, certain pathogenic bacteria have exhibited the ability to transiently shed cell wall components to avoid detection and killing by cell wall active (CWA) antibiotics, a mechanism known as spheroplasting[65,76]. Cell wall active (CWA) antibiotics are one of the most clinically relevant groups of antibiotics on the frontline of fighting bacterial infection[65]. As such, understanding the various mechanisms deployed by bacteria to evade these molecules is critical to the advancement of drug discovery. Unlike conventional persisters, which remain in a state of arrested growth until antibiotic pressure has been removed from the environment, cell wall deficient (CWD) bacteria are capable of growth and division, albeit in a more primitive manner and at a much slower rate than their cell wall replete counterparts[76]. Cell wall deficient variants of *Mtb* have been implicated in tolerance to ethambutol and suggested to play a role in disease recurrence[77]. The ability of bacteria to switch to a CWD form to evade treatment with CWA antibiotics is of increasing interest in infectious diseases research, and could pose a previously disregarded threat as it effectively renders cell wall targeting drugs insufficient in the treatment of clinical disease[78,79].

CURRENT STATE OF TB DRUG DISCOVERY

The number of reported TB cases saw a major decline in 2020 and 2021 as a result of the restrictions implemented to combat the COVID-19 pandemic; nevertheless, the World Health Organisation estimates 9.9 million people fell ill with TB in 2020, a minor decrease from previous years[80]. Of greater concern is the predicted rise in TB deaths over the coming years, as mortality rates have been severely impacted by limited access to healthcare during the pandemic[80,81]. The current TB treatment regimen was established over 40 years ago and has undergone little change since that time, with the recent introduction of bedaquiline, delamanid, and pretomanid to tackle drug-resistant TB[54,82,83]. Although several trials are under way to address the lengthy treatment times associated with TB, the paucity of low-toxicity anti-TB drugs to combat both drug-resistant and drug-sensitive TB is evident, emphasizing the necessity for development of rapid and effective drug discovery methods[83,84]. Early drug discovery adopted the drug-to-target approach whereby compound efficacy was tested in whole-cell assays, but this was discarded for a target-to-drug based approach which aimed to exploit perceived “vulnerabilities” in the mycobacterial metabolic repertoire[85]. Despite early promise, this approach has generally yielded poor outcomes owing to the fact that, while a drug may show effective inhibition when exposed to a purified enzyme in a biochemical assay, this is not always the case when presented with a permeability barrier such as the mycobacterial outer membrane[82]. Hence, the drug-to-target approach has been revisited as the initial step to discovering novel compounds with good inhibitory efficacy in whole-cell

assays, incorporating whole-genome sequencing (WGS) and a range of 'omics techniques downstream to elucidate mode-of-action of compounds with demonstrated activity[86]. For medicinal chemists, this approach presents major challenges: attempts to optimize physicochemical and pharmacological properties are confounded by the inability of the collaborating biology teams to provide any actionable reasons for loss of activity in derivative molecules modified at different sites on the core pharmacophore[87].

In vitro compound efficacy in *Mtb* is most commonly determined in a standard minimal inhibitory concentration (MIC) assay. This method provides the drug concentration at which cell growth is inhibited but it is difficult to discern whether poor compound efficacy is a result of low permeability, drug efflux or biotransformation, or weak target binding[88]. A further limitation of MIC assays is their implementation in nutrient-rich media which fails to account for the metabolic state of *Mtb* experienced in the nutrient-depleted environmental niches of the host[89]. Moreover, since permeation can only be inferred from activity in these assays, the number of compounds satisfying the criterion of "permeation" is very limited. For this reason, it is necessary to dissociate the measure of permeation from that of compound activity. A combination of MIC determination with methods that allow monitoring of permeation and efflux, as well as simple, rapid target identification would enhance *in vitro* compound testing, significantly increasing the throughput of validated molecules into *in vivo* models in the later pre-clinical phases of TB drug discovery.

RATIONALE

The application of fluorescent probes and high-resolution imaging has proven a powerful tool in understanding the growth dynamics of bacteria, providing a non-invasive and highly specific means of investigating the mechanisms involved in transcription, translation, and cell division[90,91]. Implementation of bio-orthogonal probes as a means of fluorescent tagging is gaining traction in bacterial research. Bio-orthogonal reactions exploit non-natural functional groups that allow for highly selective coupling of a target molecule to the probe in complex biological systems[92]. Of further benefit is the diminutive size of these functional groups that make them unlikely to present structural perturbations to the target molecule[92]. Such reactions have been utilized to study *in vivo* drug distribution, cellular localization of biomolecules, and translational activity[93–95]. Previous research implementing bio-orthogonal chemistry has informed much of the work presented here and is discussed in detail in Chapter 3.

Fluorescence microscopy can be readily applied to drug discovery, with the most commonly used method being a live/dead indicator such as propidium iodide which is incorporated into dead cells as a result of their compromised membrane structure[96,97]. Another commonly applied technique involves the use of a

constitutively-expressed fluorophore such as GFP to monitor population growth in the presence of environmental stressors such as nutrient starvation or antibiotic exposure[98,99]. More targeted approaches rely on fluorescent protein fusions to track localization of drug targets, or use environmentally dependent probes such as the pH-sensitive fluorescent reporter developed by Darby et al. to screen compounds for disruption of intra-bacterial pH levels[84,100].

There is little literature evaluating the use of fluorescent probes as a proxy for drug permeation. The ability of drugs to permeate the mycobacterial cell envelope is a crucial factor in their efficacy; however, the physico-chemical properties of small molecules that facilitate passage through this barrier are not well documented[101]. Several machine learning approaches have been developed in recent years to allow high-throughput analysis of mycomembrane permeation, with the aim of developing a set of parameters that accurately describe the molecular properties required by a drug-like compound to cross the cell envelope and reach its target[44,101,102]. Although computational drug discovery provides a rapid means of molecular screening, there is a lack of empirical data supporting such findings. We proposed to exploit bio-orthogonal reactions to develop a permeation assay that might provide empirical data to support *in silico* determination of molecular properties that define a good permeator. As mentioned previously, bio-orthogonal probes offer a potentially powerful tool for understanding drug permeation due to their minimal impact on native molecular structure[92]. As such, they are expected to have a minor effect on compound permeation while providing the ability to react with an intracellular target to deliver an end-point readout of cytoplasmic access.

The second part of this research addressed the potential for CWD bacilli as a tool for assessing the impact of the cell wall on compound permeation. Cell wall deficiency has recently re-emerged as an area of interest, with studies in different bacterial species investigating their potential role in pathogenicity and recalcitrance of disease[78,79]. Treatment with cell wall-targeting antibiotics is capable of driving a switch to cell wall deficiency as a means of escaping detection, and these CWD organisms can persist within the host and revert to a walled state upon withdrawal of antibiotics, presenting a previously underappreciated mechanism of evading antibiotic treatment and potentially contributing to recurrence of disease[79]. Beyond their potential role in disease, CWD bacteria provide an excellent tool in biotechnology and research into cell wall synthesis[103,104]. Organisms lacking a cell wall have been utilized as protein expression systems, removing the hindrance presented by the cell wall when extracting heterologous proteins[105]. More recently, CWD *Mycobacterium smegmatis (Msm)* have been exploited to elucidate the mechanisms behind mycobacterial cell wall synthesis[53,104]. These studies, discussed further in Chapter 4, exemplify the capacity to apply cell wall deficiency in understanding the role of the cell wall in compound permeation.

HYPOTHESIS

The hypothesis informing this doctoral research was that the mycobacterial cell wall confers intrinsic resistance to anti-TB drugs, necessitating an enhanced understanding of its role in small molecule permeation, as well as implementable tools to assist efforts towards new TB drug discovery. This further led to exploration of the intriguing possibility that stripping the cell wall under certain environmental conditions may provide an underappreciated form of tolerance to cell wall-targeting drugs.

AIM

This study set out to investigate the parameters by which the mycobacterial cell wall regulates entry of molecules into the cytoplasm; and to elucidate the functioning of the bacillus in the absence of the cell wall components.

OBJECTIVES

The objectives were designed to facilitate a comprehensive analysis of the role of the mycobacterial cell wall in permeation and bacterial survival, and comprised:

1. Determining the utility of BONCAT (Bio-orthogonal Non-canonical Amino Acid Tagging) to empirically determine compound penetration through the mycobacterial cell envelope to evaluate the reliability of *in silico* predictions of permeability.
2. Evaluating the utility of BONCAT to report on metabolic heterogeneity in mycobacteria
3. Developing and characterizing a cell wall-deficient “spheroplast” model of *Msm.*
4. Validating loss of cell wall components in lysozyme-treated *Msm* by means of microscopic exploration and fractional proteomic analysis.

CHAPTER 2: METHODS AND MATERIALS

BACTERIAL STRAINS AND STANDARD CULTURE CONDITIONS

Mycobacterium smegmatis (Msm) strains were grown in Middlebrook 7H9 growth medium supplemented with 0.05% $Tween_{80}$, 2% glycerol and 10% OADC at 37°C in a shaking incubator. Freezer stocks of *Msm* were grown overnight and sub-cultured to reach mid-log phase (OD_{600} 0.5-0.8) the following day. Where necessary, antibiotics were added to mycobacterial cultures at the required concentrations.

Table 2.1. Bacterial Strains used in this study

Msm Strain	Reference
mc^2155 (wild-type)	Snapper et al. [106]
parB::mCherry	Santi & McKinney [107]

PREPARATION OF STOCK SOLUTIONS AND SPECIALIZED MEDIA

TABLE 2.2 Reagents required to perform BONCAT Analyses

BONCAT Reagents			
Reagent	**Constituents**	**Provider**	**Additional Steps**
PBS Buffer	1 PBS tablet 200ml ddH_20	Sigma-Aldrich	Filter sterilized
50mM THPTA	21.7g THPTA 1ml ddH_20	Sigma-Aldrich	
20mM Copper Sulfate	3.19g Copper sulfate 1ml ddH_20	Sigma-Aldrich	
100mM Aminoguanidine Hydrochloride	11mg Aminoguanidine Hydrochloride 1ml PBS Buffer	Sigma-Aldrich	*Made fresh for each experiment
100mM Sodium Ascorbate	19.8mg Sodium Ascorbate 1ml PBS Buffer	Sigma-Aldrich	*Made fresh for each experiment
100mM 2-Chloro-acetamide	93.5g 2-Chloro-acetamide 10ml PBS Buffer	Sigma-Aldrich	
100mM Azido-homoalanine	180mg Azido-homoalanine 10ml ddH_2O	Sigma-Aldrich	Stored at 4°C
1mM TAMRA Alkyne	1mg TAMRA Alkyne 467µl DMSO	DivBio Science	Stored at -20°C
1mM TAMRA DBCO	1mg TAMRA DBCO 936µl DMSO	Sigma-Aldrich	Stored at -20°C
1mM ROX Alkyne	1mg ROX Alkyne 572µl DMSO	DivBio Science	Stored at -20°C
1mM ROX DBCO	1mg ROX DBCO 835µl DMSO	DivBio Science	Stored at -20°C
1mM Cy3 Alkyne	1mg Cy3 Alkyne 530µl DMSO	DivBio Science	Stored at -20°C
1mM Cy3 DBCO	1mg Cy3 DBCO 903µl DMSO	DivBio Science	Stored at -20°C
5mM coumBARAC	1.9mg coumBARAC 1ml DMSO	NIH/NIAID	Stored at -20°C

TABLE 2.3 Spheroplasting media, reagents and buffers

Spheroplast Reagents			
Reagent	**Constituents**	**Provider**	**Additional Steps**
0.2M Maleate Buffer	24.2g Tris 23.2g Maleic Acid 900ml ddH_20	Sigma-Aldrich Sigma-Aldrich	Adjusted to pH6.6 with 10mM NaOH Made up to 1L with ddH_20 Filter sterilized
SMM Buffer	171g Sucrose 1.9g Magnesium Chloride 100ml 0.2M Maleate Buffer	Sigma-Aldrich Sigma-Aldrich	Made up to 1L with ddH_20 Filter sterilized
TSB-SMM	30g TSB Powder 171g Sucrose 1.9g Magnesium Chloride 100ml 0.2M Maleate Buffer	Sigma-Aldrich Sigma-Aldrich Sigma-Aldrich	Made up to 1L with ddH_20 Filter sterilized
20% (w/v) Glycine	20g Glycine 60ml ddH_20	Sigma-Aldrich	Made up to 100ml with ddH_20 Filter sterilized
10mg/ml Lysozyme	10mg Hen Egg White Lysozyme 10ml ddH_20	Sigma-Aldrich	Stored at 4°C *Lysozyme stocks were made once a month to avoid lysozyme degradation

TABLE 2.4 Reconstitution of fluorescent probes

Fluorescent Probes			
Reagent	**Constituents**	**Provider**	**Additional Steps**
10mM NADA	2.67mg NADA 1ml DMSO	H3D	Stored at -20°C
823µM FM™ 4-64	100µg FM™ 4-64 200µl DMSO	ThermoFisher	Stored at -20°C *Stock solutions were unstable and discarded after 2 weeks
5mM BODIPY™ 581/591 C11	1mg BODIPY™ 581/591 C11 400µl DMSO	ThermoFisher	Stored at -20°C

TABLE 2.5 Reagents required for proteomic analysis

Proteomics Reagents			
Reagent	**Constituents**	**Provider**	**Additional Steps**
Lysis Buffer	1 Protease Inhibitor Tablet 10ml PBS Buffer	Roche	Stored at 4°C
Cell Wall Detergent	20µl Triton-X-100 10µl Tween-20 40mg CHAPS 20ml PBS Buffer	Sigma-Aldrich Sigma-Aldrich Sigma-Aldrich	Stored at 4°C
Cell Debris Detergent	315mg Tris 400mg SDS 31mg DTT 20ml PBS Buffer	Sigma-Aldrich Sigma-Aldrich Sigma-Aldrich	Stored at 4°C
Denaturation Buffer	3.6g Urea 1.5g Thiourea 12mg Tris	Sigma-Aldrich Sigma-Aldrich Sigma-Aldrich	Stored at -20°C
Solution A	2% (v/v) Acetonitrile 0.1% (v/v) Formic Acid	Sigma-Aldrich Sigma-Aldrich	

Solution C	60% (v/v) Acetonitrile 0.1% (v/v) Formic Acid	Sigma-Aldrich Sigma-Aldrich	

TABLE 2.6 Reconstitution of antibiotics

Antibiotic Stock Solutions			
Reagent	**Constituents**	**Provider**	**Additional Steps**
10mM Streptomycin	14.6mg Streptomycin Sulfate 1ml ddH_20	Sigma-Aldrich	Stored at 4°C
10mM Rifampicin	8.2mg Rifampicin 1ml DMSO	Sigma-Aldrich	Stored at 4°C
10mM Ethambutol	2mg Ethambutol 1ml ddH_20	Sigma-Aldrich	Stored at 4°C
500µM Linezolid	0.17mg Linezolid 1ml ddH_20	Sigma-Aldrich	Stored at 4°C
500µM Linezolid Azide	0.2mg Linezolid Azide 1ml ddH_20	Institute for Molecular Bioscience, Queensland, Australia	Stored at 4°C
500µM Roxithromycin	0.42mg Roxithromycin 1ml ddH_20	Sigma-Aldrich	Stored at 4°C
500µM Roxithromycin Azide	0.44mg Roxithromycin Azide 1ml ddH_20	Institute for Molecular Bioscience, Queensland, Australia	Stored at 4°C
500µM Vancomycin	0.72mg Vancomycin 1ml ddH_20	Sigma-Aldrich	Stored at 4°C
500µM Vancomycin Azide	0.8mg Vancomycin Azide 1ml ddH_20	Institute for Molecular Bioscience, Queensland, Australia	Stored at 4°C

TABLE 2.7 Standard reagents used for molecular biology

Standard Reagents			
Reagent	**Constituents**	**Provider**	**Additional Steps**
2% (w/v) Alamar Blue	2g Resazurin Sodium Salt 100ml ddH_20	Sigma-Aldrich	Stored at 4°C
1M Hydrogen Peroxide	0.88ml 8.8M Hydrogen Peroxide Solution 9.12ml ddH_20	Sigma-Aldrich	
50X TAE Buffer	242g Tris 100ml 0.5M EDTA Solution 57.1ml Glacial Acetic Acid	Sigma-Aldrich Sigma-Aldrich Sigma-Aldrich	Adjust volume to 1L with ddH_2O Dilute to 1x working stock for gel electrophoresis
1X TE Buffer	121mg Tris 2.9mg EDTA 100ml ddH_20	Sigma-Aldrich Sigma-Aldrich	Adjusted to pH8.0 with 10mM HCl
Loading Dye	40mg Bromophenol Blue 4.5ml Glycerol 10.5ml ddH_20	Sigma-Aldrich Sigma-Aldrich	Filter sterilized Pipetted into 1ml aliquots Stored at -20°C

IN SILICO PERMEABILITY PREDICTION

The formula established by Lee et al. to calculate predicted permeability of drug-like compounds in *Mycobacterium tuberculosis* (*Mtb*) was adapted for the specific purposes of this work[108]. Available molecular structures of click chemistry fluorophores were collected from several commercial websites (see Supplementary Table 1) and imported into Marvin Sketch to calculate lipophilicity (logD), polar surface area (PSA) and fraction of rotatable bonds (f_{rb}). The following formula was applied to all fluorophores to calculate predicted permeability values:

$$P_{(calc)} = (0.2*logD) + (-0.004*PSA) + (0.36*f_{rb}) - 4.313$$

BIO-ORTHOGONAL NON-CANONICAL AMINO ACID TAGGING (BONCAT)

The BONCAT labelling method was adapted from Hydrocarbon and Lipid Microbiology Protocols[109]. Briefly, 10ml cultures of *Msm* were grown to an OD_{600} of ~0.3-0.4 before incubation with 1mM AHA for 3h at 37°C. For protein synthesis inhibition, pre-treatment with ¼× MIC (0.67µM) streptomycin at was carried out for 3h at 37°C before AHA labelling. Cultures were centrifuged at 4000rcf for 10min and resuspended in 1ml of PBS to concentrate cells, before being passed through a 5µm filter to remove clumps. Cells were either used immediately or frozen at -20°C for future use. 50µl of cells was added to a poly-L-lysine coated coverslip and incubated at room temperature for 15min. The coverslips were washed once with PBS and incubated at room temperature with 80% ethanol or PBS for 30min for permeabilized and non-permeabilized cells, respectively. The CuAAC reaction cocktail was prepared in two separate microtubes; 220µl PBS, 12.5µl of 100mM aminoguanidine hydrochloride and 12.5µl of 100mM sodium ascorbate were added to Tube 1 and 2.5µl of 20mM copper (II) sulphate, 5µl of 50mM THPTA and 2.5µl of 500µM alkyne dye were added to Tube 2. The tubes were incubated for 3min, 5µl was added from Tube 2 to Tube 1 and mixed by inversion. 20µl of the reaction cocktail was added to the coverslip and incubated at room temperature for 30mins. The coverslip was then washed 3 times with PBS before placing on a microscope slide for analysis. For SPAAC, cells were incubated with 50µl of 100mM 2-chloroacetamide after ethanol permeabilization for 1h in the dark. The cells were then incubated with 1µM dibenzocyclooctyne (DBCO) dye for 30min in the dark. The coverslip was then washed 3 times with PBS before placing on a microscope slide for analysis.

TREATMENT WITH AZIDE-FUNCTIONALIZED DRUGS

Treatment with azide-functionalized drugs was performed in a similar manner as with the BONCAT assays. 10ml cultures of *Msm* were grown to an OD_{600} of ~0.3-0.4 before incubation with azide-functionalized drugs at 1× MIC for 3h at 37°C, following this the fluorogenic coumBARAC probe was employed for SPAAC labelling, performed as before, of internalized azide-tagged drugs.

GENERATION OF SPHEROPLASTS

Wild-type *Msm* was grown in TSB growth medium to an OD_{600} of 0.8-1.0 before addition of 1.2% (w/v) glycine for 16-20h at 37°C. The cells were then centrifuged at 4000rcf for 10min, washed once with SMM buffer and centrifuged as before. The cell pellet was then resuspended in TSB-SMM media containing 1.2% glycine and 100µg.ml^{-1} lysozyme for overnight incubation at 37°C.

DNA EXTRACTION

1ml of culture was centrifuged at 13000rcf for 5min and the pellet was resuspended in 50µl TE Buffer before incubating at 80°C for 5min to rupture cells. 100µl chloroform-isoamyl alcohol (1:1) was added to the solution and mixed by inverting then the sample was centrifuged at 13000rcf for 5min. The supernatant (containing the DNA) was carefully removed for subsequent gel electrophoresis and PCR analyses.

GEL ELECTROPHORESIS

1% (w/v) agarose gels were prepared by adding 0.3g agarose powder to 30ml Tris-acetate-EDTA (TAE) buffer and dissolving by heating in a microwave. The agarose was allowed to cool slightly before addition of 0.5µl ethidium bromide and setting of the gel in a casting tray. Set gels were placed in a gel electrophoresis tank containing 1× TAE buffer and 5µl DNA and 2µl loading dye were added to appropriate wells. Molecular Weight Marker III (Roche Applied Science) was used to determine band sizes. The tank was then attached to a power bank (Bio-Rad) and gels were run at 80V for 30min.

PCR

PCR reactions were performed using Q5® High-Fidelity DNA polymerase (NEB) and set up in a reaction tube containing 5µl 5× Q5 Reaction Buffer (NEB), 0.5µl 10mM dNTPs, 1.25µl of both forward and reverse

primers achieving a final concentration of 0.5µM, 0.25µl Q5® High-Fidelity DNA polymerase, 5µl 5× Q5 High GC Enhancer, 50ng template DNA (DNA concentration determined using NanoDrop) and nuclease-free water up to 25µl. Cycling conditions to amplify the *metH* fragment (2382bp) were as follows: initial denaturation at 98°C for 2min, 35 cycles of 98°C for 10s, 68°C for 25s and 72°C for 2min and final extension at 72°C for 4min. Primers used were:

metH Forward Primer: CAACATGGACGAGGGCATGA
metH Reverse Primer: GACTGCGGGTGCGAGAAATA

CELL ENVELOPE STAINING

All staining was carried out in wild-type and spheroplast *Msm*. 10ml cultures were centrifuged at 4000rpm and pellets were resuspended in 1ml 7H9 (for wild-type) or TSB-SMM (for spheroplasts) to concentrate the bacteria. 100µl aliquots were taken for each sample and cells were then stained with either 100µM DMN-trehalose or 100µM NADA for 20min at 37°C, washed two times in PBS (for wild-type) or SMM buffer (for spheroplasts) and imaged immediately to track changes in cell envelope composition. FM™ 4-64 Dye (ThermoFisher Scientific) was added to 100µl of each sample on ice to a final concentration of 5µg/ml for 1min and bacteria were imaged immediately without washing.

NUCLEIC ACID STAINING

Cells were prepared as described previously and 2µl Syto™ 9 was added to 1ml concentrated culture to reach a final concentration of 10µM. Cells were incubated at room temperature for 10min and imaging was conducted immediately without washing.

LIPID PEROXIDATION ASSAY

Cultures of wild-type *Msm* were grown to an OD_{600} of 0.6-0.8 and spheroplasts were prepared as previously indicated. For hydrogen peroxide (H_2O_2) treatment, wild-type cultures were incubated with 1mM H_2O_2 for 1.5h at 37°C before washing twice with PBS. All 10ml cultures were centrifuged at 4000rpm and pellets were resuspended in 1ml 7H9 (for wild-type) or TSB-SMM (for spheroplasts) to concentrate the bacteria. 500µl aliquots of each culture were stained with BODIPY™ 581/591 C11 (ThermoFisher Scientific) at 5µM for 1h at 37°C. Cells were washed twice in the relevant buffers and imaged immediately.

MICROPLATE ALAMAR BLUE ASSAY (MABA)

50µl of 7H9 was added to all wells of a 96-well plate, before addition of tested drugs at the relevant concentrations to the top row of all wells. A 2-fold serial dilution of drug was performed down the columns of the plate. Wild-type *Msm* was grown to OD_{600} ~0.5 before 1:1000 dilution with 7H9 media and addition of 50µl to rows B-D of the plate. As spheroplasts showed little ability to replicate, cultures were filtered to remove clumps and 50µl of culture was added directly to the plate in rows E-G. Rows A & H served as the "growth" and "no growth" controls, respectively (**Figure 2.1**). Plates were incubated for 48h at 37°C before addition of 10µl Alamar Blue to all wells. Plates were incubated with Alamar Blue for 4h during which respiring cells reduced the die from a blue to pink colour. Absorbance was read using the FLUOstar OPTIMA (BMG LABTECH) microplate reader and calculations were performed to determine MIC_{90} of tested drugs.

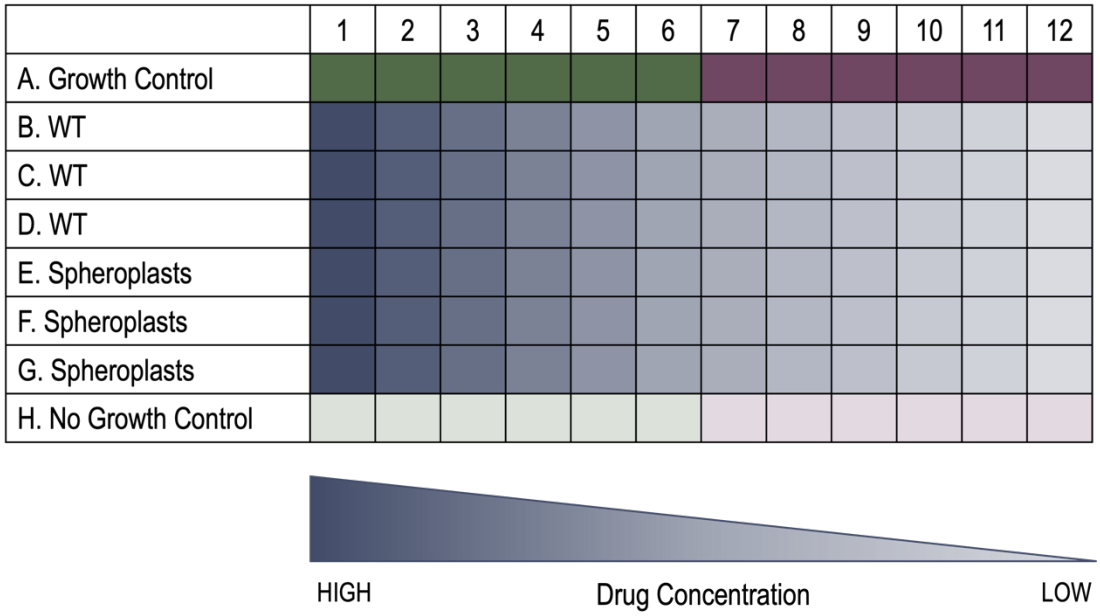

Figure 2.1. MABA plate setup. Standard microplate Alamar Blue assays were performed in clear, U-bottom, 96-well plates with 2-fold drug dilutions from rows 1-12. Growth control wells contained no antibiotic, and no growth controls were not inoculated with bacteria. Green wells indicate wild-type (WT) controls and purple wells indicate spheroplast controls.

END-POINT MICROSCOPY

All end-point imaging was carried out using a Zeiss Axio Observer with 100× oil immersion phase contrast lens. For BONCAT analyses, coverslips that were pre-incubated with bacteria and stained were added to microscope slides using 5µl PBS. For cell envelope staining and lipid peroxidation assays, 5µl of culture was placed directly onto a microscope slide and sealed with a coverslip for imaging.

TIME-LAPSE MICROSCOPY

Gene Frame® Preparation

Before preparation of time-lapse samples, the microscope was switched on to allow the incubation chamber and heating ring on the 100× objective lens to reach 37°C. Mid-log phase cultures were passed through a 5µm filter using a syringe to remove any clumps. 1.5% (w/v) low-melting point agarose was dissolved in 10ml deionized water and allowed to cool slightly before addition of 10ml pre-warmed 2× concentrated 7H9 or TSB-SMM media to obtain a 1× concentration of media containing 0.75% agarose. A Gene Frame® was adhered to a glass microscope slide before addition of 50µl agarose-containing media. Another glass slide was placed over the agarose and the two slides were tightly sandwiched together using tape. The agarose was allowed to set for 15min before carefully removal of the top slide. The top layer of the Gene Frame® was removed to expose the adhesive edge before addition of 2µl filtered culture to the agarose pad. The culture was gently distributed across the pad by tilting the slide and allowed to dry out for 5min before sealing with a coverslip. Prepared slides were inserted into the incubating chamber of the Zeiss Axio Observer and left for 30min to allow stabilization of the sample at 37°C. Immersion oil was placed on the 100× objective lens before inserting the incubating chamber into the stage piece.

CellASIC® ONIX2 Preparation

Mid-log phase cultures were passed through a 5µm filter using a syringe to remove any clumps. 200µl of media was pipetted into the first row of solution inlet wells of a CellASIC® ONIX2 bacterial plate and where necessary, media or buffer containing relevant antibiotics or lysozyme was dispensed into subsequent wells (row 2-5). A 50µl aliquot of culture was pipetted into the cell inlet wells (row 8) of the plate and 200µl PBS or SMM buffer was added to the outlet wells (row 7). Immersion oil was placed on the 100× objective lens, the plate was sealed with the manifold and placed on the microscope stage. Using the CellASIC® ONIX2 software, the bacteria in row 8 were perfused into the viewing chamber and this step was repeated until an adequate number of cells were visible. Next, the experimental settings were defined in the software, determining the length of time each row of media or reagents was perfused across the viewing chamber of the plate.

For both agarose pad and CellASIC® ONIX2 experiments, time-lapse parameters were set using the ZEN software, using the Time Series and Tile Setup settings. The necessary imaging channels were selected and fluorescence settings were applied where necessary. Software autofocus was set to scan 20µm above and below the designated z-plane to ensure images remained in focus throughout the

experiment. Regions of interest were selected, and parameters were set to automatically image regions of interest at 30min intervals with experiments taking place over a 16-24h period.

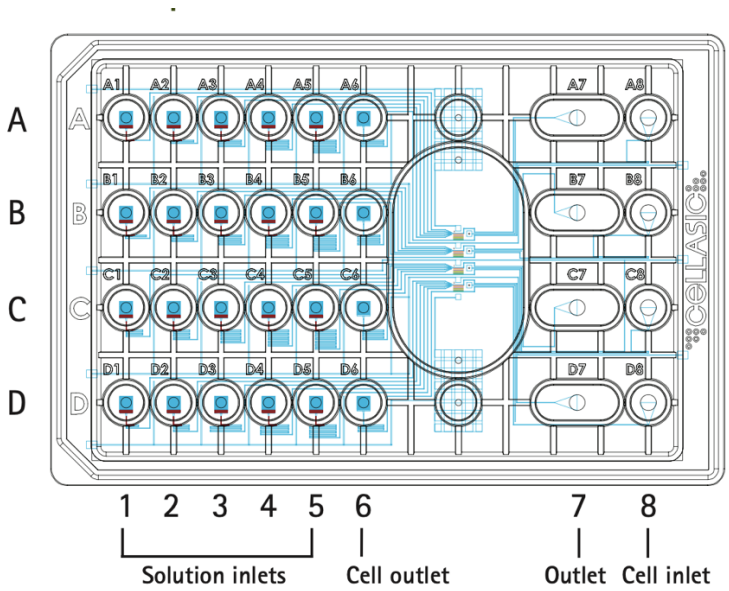

Figure 2.2. Diagram of a CellASIC® ONIX2 bacterial plate[110].

IMAGE ANALYSIS

All image analysis was carried out using Fiji 2.1.0. Fluorescence image brightness settings were kept constant across all samples being compared. Fluorescence quantification was achieved by thresholding brightfield images to obtain a binary output displaying the bacteria. Measurements were set to capture information pertaining to area, standard deviation, mean grey value and integrated density and binary images were redirected to fluorescent images to obtain the above data for individual bacteria. Integrated density values were employed in determining single cell fluorescence. Number of foci in *Msm parB*::mCherry and Syto™ 9 samples were determined using the Total Maxima function for foci displaying prominence >200. Medial axis profiling was performed using the MicrobeJ plugin and the Profile descriptor following detection of bacteria.

PREPARATION OF PROTEIN FRACTIONS FOR MASS SPECTROMETRY

50ml cultures of wild-type and spheroplast *Msm* were centrifuged at 4000rpm for 10min and washed twice in PBS (wild-type) and SMM buffer (spheroplasts) twice before another centrifugation step followed by snap-freezing of pellets in liquid nitrogen. Samples were thawed at room temperature, pellets were resuspended in 1ml lysis buffer and transferred to a sterile 2ml microtube. Microtubes were placed in a

beaker containing an ice slurry for sonication using a probe sonicator (United Scientific) with pulse settings of 15s on and 15s off for a period of 5min at an amplitude of 30V for each sample. The probe was wiped with 70% ethanol and pulsed for 1min in ddH_2O between samples. Lysates were then centrifuged at 8000rcf for 10min at 8°C and the supernatant was carefully removed and passed through a 0.22µm filter into a fresh microtube using a 1ml syringe. The remaining pellet contained the cell debris which was washed twice with PBS and centrifuged at 8000rcf for 10min at 8°C. The PBS was removed from the samples, the debris pellet was resuspended in cell debris detergent and boiled at 95°C for 30min. Debris samples were allowed to cool on ice before a final centrifugation step at 8000rcf for 10min at 8°C, after which the supernatant was transferred to a fresh microtube and stored at -20°C for downstream analysis.

The supernatants collected after sonication were subjected to centrifugation at 22 000rcf for 30min at 4°C to separate the cell envelope fraction from the cytoplasmic fraction. The supernatant formed here contained cytosolic proteins, these were carefully removed and placed in a fresh microtube for storage at -20°C until downstream analysis took place. The cell pellet, containing cell envelope proteins, was washed twice with PBS and centrifuged as before. After removal of PBS, the cell pellet was resuspended in 1ml cell wall detergent and stored at -20°C.

MASS SPECTROMETRY

Fractions isolated for each cell type were allowed to thaw at room temperature before transfer to a Falcon tube containing acetone and methanol to obtain a sample:acetone:methanol ratio of 1:8:1. Samples were stored overnight at -20°C for protein precipitation. Following this, samples were centrifuged at 4000rcf for 10min before washing with ice-cold 80% acetone and repeating centrifugation. The protein pellet was allowed to briefly air-dry before resuspension in 1ml denaturation buffer and transfer to a fresh microtube for storage at -20°C until further use.

A Bradford assay was performed to quantify protein present in each fraction, whereby 5µl of each sample and 10µl of each standard (BSA ranging from 25-200ng/µl) were aliquoted into a 96-well plate in duplicate before addition of 250µl Bradford reagent to all wells. Absorbance at a wavelength of 595nm was read using a microplate reader and protein concentrations in each sample were determined based on the standards. A volume of each sample containing 20µg protein was aliquoted into a fresh microtube, to which DTT was added to a final concentration of 3mM for incubation at room temperature for 20min. Next, iodoacetamide was added to a final concentration of 15mM and samples were incubated in the

dark at room temperature for a further 20min. A 40µg/ml solution of LysC was added to samples at a ratio of 1:100 and incubated at 30°C for 3h. Samples were then diluted 5× with 5mM ammonium bicarbonate and pH was confirmed to be 8.0. Lastly, trypsin was added to each sample at a ratio of 1:100, incubated overnight at 30°C and the tryptic digested halted by addition of 0.5% formic acid.

The final step in protein preparation required desalting of tryptic digests using C18 resin for mass spectrometry. The stage tips were prepared for desalting by creating a hole in the centre of each sterile 2ml microtube into which a 200µl pipette tip was placed. Discs of C18 resin were cut using the base of a sterile pipette tip and gently down into the stage tip to ensure it was firmly wedged in place. The C18 resin within the stage tips was activated by adding 100µl of 100% methanol and the microtubes were centrifuged at 50g for 1min to allow the liquid to pass through the resin. Following this, 200µl of Solution A was added to the stage tip to equilibrate the C18 resin and microtubes were centrifuged as before. Flow-through was discarded from the microtube as was necessary. A volume of each sample containing 10µg of tryptic peptides was pipetted into each stage tip and centrifuged at 50g for 5min to allow for protein binding to the resin. The bound peptides were then washed with 200µl of Solution A, centrifuged at 200rcf for 1 min and the flow-through was removed. A glass vial was inserted into the microtube beneath the stage tip and peptides were eluted with addition of 100µl of Solution C and centrifugation at 20rcf until the C18 resin appeared dry. Finally, eluted peptides were dried using a SpeedyVac concentrator and resuspended in Solution A to a final concentration of 1µg/µl before carrying out tandem mass spectrometry.

BIOINFORMATIC ANALYSIS

Initial steps of proteomic analysis were carried out by Tariq Ganief (Blackburn Lab, IIDMM, University of Cape Town) using the MaxQuant software to obtain label free quantification (LFQ) values for all identified peptides. Protein lists for each fraction were obtained after protein identification using the Uniprot proteome for *Msm* (Proteome ID: UP000000757, 6601 proteins, 14/05/2016) and removal of reverse hits and common contaminants. Only proteins with a q-value <0.01 and number of unique peptides exceeding 2 were used from downstream analysis. Further analysis was performed using Perseus V1.52.6 to identify proteins unique to each fraction and significance analysis to determine changes in relative abundance between spheroplast and wild-type fractions. All protein lists were exported to Excel for downstream analysis. To infer functional annotation, Cytoscape V3.9.1 was utilized, and the ClueGO V2.5.8 application allowed for download of the *Mycobacterium smegmatis* str. mc^2155 annotation list. ClueGO functional annotation was performed using UniProt protein IDs and annotation from Gene Ontology and

KEGG databases. Figures were generated by selecting for display of pathways with $p>0.05$ and the Significance visual style, all other parameters were set to default. Functional association networks were saved as images and ClueGO results tables were exported to Excel for further analysis. Volcano plots were generated in R Studio to demonstrate alterations in protein abundance between samples.

CHAPTER 3: INVESTIGATING CELL WALL PERMEATION

Background

BIO-ORTHOGONAL CHEMISTRY

Bio-orthogonal reactions present a powerful tool in biology, providing a means of labelling molecules of interest in a way that allows for reliable reaction with the target without interfering with its biological system[111,112]. The wide variety of conditions present across biological systems present challenging environments in which these reagents must remain inert to their surroundings but exhibit robust reactivity with one another to generate stable linkages between target and probe[111]. In spite of these demands, chemical biologists have developed an impressive collection of bio-orthogonal functional groups that show remarkable selectivity owing to their non-natural properties while causing only minor perturbations to the functionality of their targets due to their diminutive size[112,113]. This method of biomolecule tagging accommodates linkage of reactive moieties to fluorescent probes, allowing for thorough investigation into biological processes, from *in vivo* evaluation of drug activity in mouse models to peptidoglycan labelling for live imaging of bacteria[93,114].

Bio-orthogonal reactions are largely composed of cycloaddition reactions which fall under the umbrella of click chemistry, a powerful set of reactions that is reliable, distinctly selective, and capable of generating high yields of product[115,116]. Evidence of such reactions occurring in nature was observed by Sharpless et al. who noted the significance of primary metabolites in providing the building blocks of life that can undergo reversible condensation to form polymers[115]. The simple and highly versatile nature of such reactions provides a promising basis for rapid compound synthesis with the added benefits of proceeding with high yields at each step in the synthetic process and generating low-level, inoffensive by-products that are easily removed from the system[115,117]. The crux of such reactions is the coupling of small molecules using heteroatom links (C-X-C), to provide a robust tool for molecular synthesis that utilizes readily available reagents in a near-complete reaction that generates a single product[115].

Huisgen's 1,3-dipolar cycloaddition of azides and alkynes to yield a triazole product (**FIGURE 3.1**) rapidly emerged as a frontrunner in the click chemistry field owing to the easy installation of azide and alkyne moieties in compounds of interest and their tolerance to a range of functional groups and reaction conditions[116–118]. Furthermore, the low reactivity of azides and alkynes towards biological molecules and absence of azide in naturally occurring molecules suggested applicability in biological systems[113,117,118]. However, this inertness is reflected in the kinetic properties of the reaction, making Huisgen's 1,3-dipolar

cycloaddition an incredibly slow process. In the development of click chemistry, this was rapidly circumvented by the addition of a copper(I) catalyst that resulted in significant rate enhancement, thus propelling copper(I)-catalyzed azide-alkyne cycloaddition (CuAAC) to the forefront of synthetic chemistry[112,117,119]. Although a versatile tool for medicinal chemists, the copper(I) catalyst required for this process to occur timeously is not ideal in biological systems due to its cytotoxic effects[112].

To circumvent the problem of metal toxicity caused by the copper(I) catalyst, ligands can be added to stabilize the oxidation state of copper(I) and prevent generation of reactive oxygen and nitrogen species[116,120]. Although this method has shown efficacy in live cells, an alternative approach to eliminate the need for a copper catalyst altogether was introduced by Bertozzi et al. who exploited the unstable nature of cyclic alkynes to drive the reaction[94,112]. The strain experienced by an alkyne in its cyclic conformation (**FIGURE 3.1**) is able to drive triazole formation in the absence of a catalyst, allowing for non-toxic labelling of live cells[94,121]. Hence, strain-promoted azide-alkyne cycloaddition (SPAAC) has become an attractive method for molecular labelling in live organisms and much work has been invested in optimizing cyclooctynes for bio-orthogonal applications[112,113].

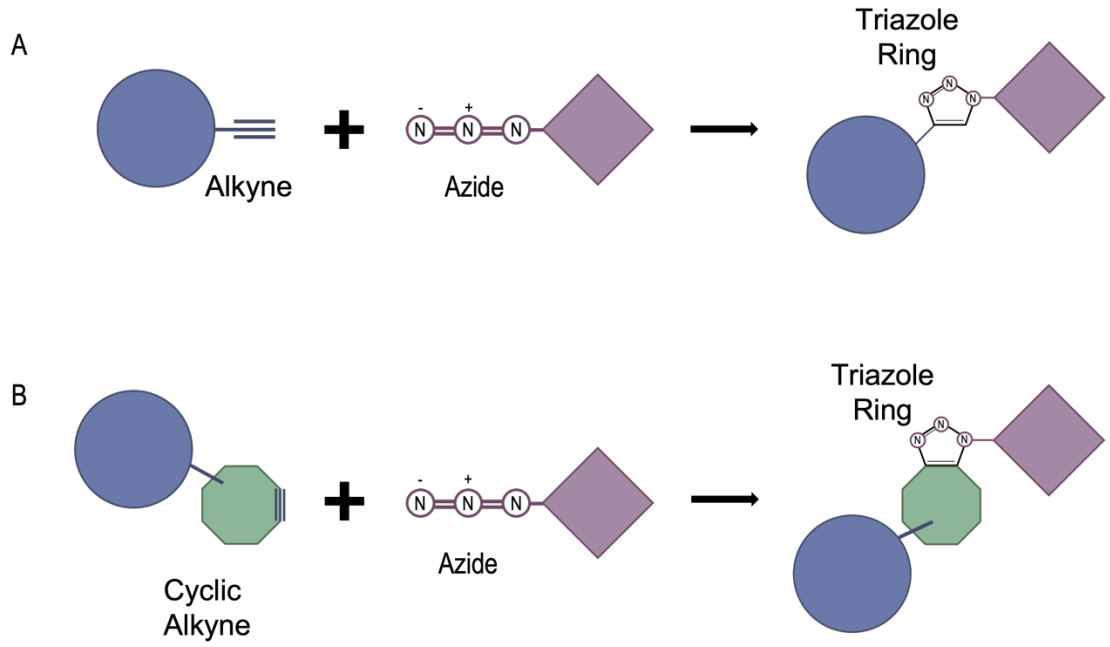

FIGURE 3.1. Huisgen's 1,3-dipolar cycloaddition. (A) Cycloaddition reaction occurring between alkyne and azide moieties to form a triazole functional group between target and probe, a slow reaction that can be catalysed by the addition of a copper(I) catalyst. (B) Cycloaddition reaction between azide and cyclo-alkyne moieties forming a triazole functional group between target and probe, driven by the strained ring conformation of the cyclo-alkyne. Probes and targets are represented by blue circles and purple diamonds, target and probe can be linked to either moiety to achieve bio-orthogonal tagging.

FLUOROGENIC PROBES

A challenge in fluorescent bio-orthogonal reactions is the issue of background fluorescence arising from unreacted probe in the sample, which necessitates several wash steps and consequently poses a problem for *in vivo* studies[113].The use of fluorogenic probes, labelling molecules that only become fluorescent upon reaction, alleviates the need for wash steps[122,123]. Although a number of these probes exist for copper(I)-catalysed bio-orthogonal reactions, their application in live-cell imaging again drove the development of fluorogenic molecules that could be incorporated into the SPAAC system[124]. Owing to the bulky nature of cyclic alkynes, it is preferable to attach the azide moiety to the target molecule to prevent any steric hindrance, in turn requiring the fluorogenic probe to be linked to the cyclo-alkyne[122]. Again, the Bertozzi group pioneered this research, utilizing the photophysical properties of coumarin-based fluorophores which lend themselves to easy modifications that enhance brightness, to develop coumBARAC[123,125]. This fluorogenic compound, which exhibits 10-fold fluorescent enhancement upon triazole formation, has shown efficacy in live imaging of mammalian cells[123,126]. Since then, several other fluorogenic probes have been developed and implemented in both mammalian and bacterial systems[114,124,127].

BONCAT (BIO-ORTHOGONAL NON-CANONICAL AMINO ACID TAGGING)

Bio-orthogonal non-canonical amino acid tagging - or 'BONCAT' - involves fluorescent labelling of newly synthesized proteins to detect metabolically active cells within a population[128]. This technique was initially developed for the study of mammalian cells but has been rapidly adapted for application in prokaryotes[129,130]. Two methionine analogues, L-azidohomoalanine (AHA) and homopropargylglycine (HPG), are currently utilised in BONCAT[131]. These non-canonical amino acids carry small functional groups (azide in AHA, alkyne in HPG) that can be applied in bio-orthogonal reactions[131,132]. BONCAT relies on the metabolic incorporation of these non-canonical amino acids into proteins followed by covalent coupling of the resultant proteins with a biotin- or fluorophore-linked tag[130]. Although the cell wall of mycobacteria provides a potential obstacle to entry of these synthetic amino acids, their similarity to methionine suggests they can gain entry into the cell via the same pathway as the native amino acid. Indeed, it has previously been found that a D-alanine analogue is capable of entering *Mtb* cells to allow BONCAT labelling[133], suggesting that methionine analogues will be capable of the same. Moreover, previous work in my host laboratory (Moosa, Mashabela, unpublished) and in other groups[134] has established the ability of *Mtb* to assimilate exogenous L-methionine.

Upon successful incorporation of the methionine analogue into proteins, the azide/alkyne group undergoes click cycloaddition with the click-modified probe to form a triazole conjugate which links the non-canonical amino acid to the relevant tag[95,130]. Biotinylated peptides from active cells can then be captured and purified using avidin beads and analysed using mass spectrometry[132]. Alternatively, newly synthesized proteins are bio-orthogonally labelled with fluorescent probes for visualization under the microscope (**FIGURE 3.2**)[95,128,132].

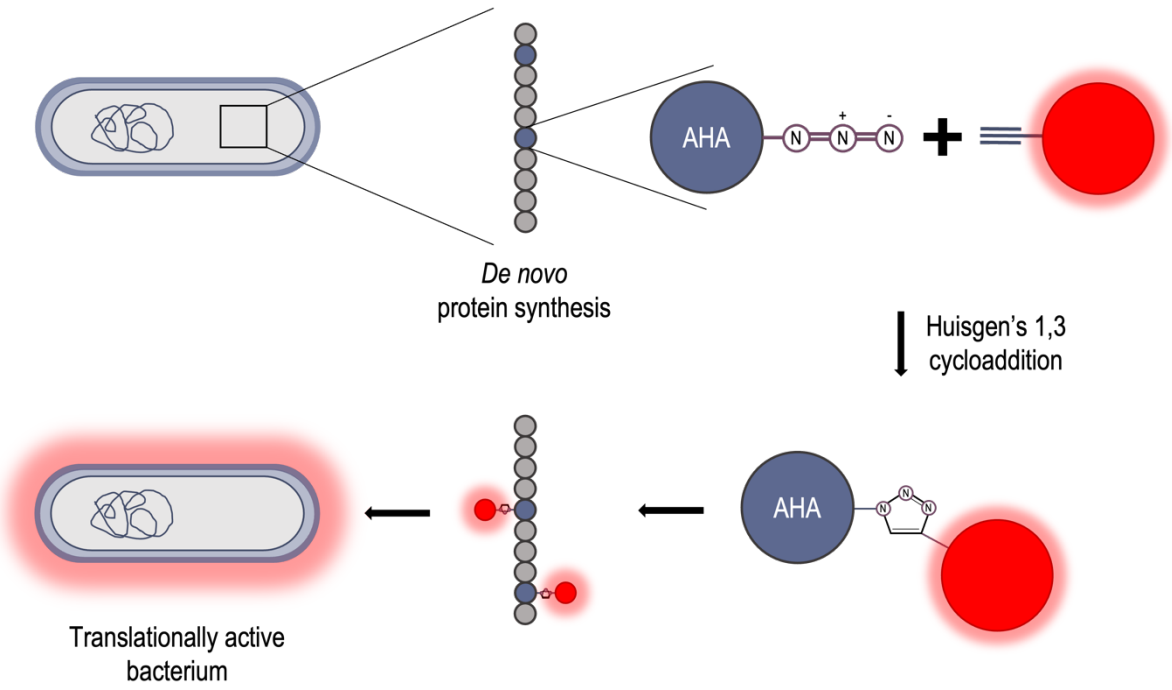

FIGURE 3.2. BONCAT in bacteria. Newly synthesized proteins incorporate the methionine analogue (AHA) containing an azide moiety that reacts with an alkyne-linked fluorophore (red), forming a triazole link between probe and target to allow for visualization of active translation in bacterial cells using fluorescence microscopy. AHA residues are represented by blue circles in the newly synthesized protein, red circles represent the alkyne-linked fluorophore.

Protein labelling offers a much more reliable approach to understanding cellular metabolism in comparison to studying RNA levels which often vary and can show poorly correlation to expression levels of their encoded proteins[135]. BONCAT allows unbiased study of whole-cell translational activity in response to external stimuli. Although currently limited to labelling proteins containing methionine, this approach allows for tagging of the majority of cellular proteins as most species, across eukaryotes and prokaryotes, harbour a very high percentage of methionine-containing proteins[130]. Furthermore, BONCAT provides an intriguing solution to the problem of unculturable bacteria as the synthetic amino acid can be added to bacterial populations *in situ* to allow study of protein synthesis in a native environment[128]. This technique also offers a much more affordable and higher throughput method to

study *in situ* activity of individual cells in comparison to other currently available technologies which involve stable isotopes or radioactive molecules and invariably require the use of specialized facilities and expensive equipment[95]. Other means of protein labelling are also biased in that they involve probes that are designed to target specific proteins, hindering the ability to grasp the inner workings of the proteome as a whole[136]. Therefore, BONCAT offers a promising approach to understand whole-cell protein activity and cellular metabolism.

Results

IN SILICO PERMEABILITY PREDICTION

Based on previous work in *Mycobacterium tuberculosis (Mtb)*, we selected a set of parameters to calculate hypothetical permeability values (P_{calc}) to inform mycomembrane permeation[108]. The descriptors selected to generate our formula were the distribution coefficient of hydrophobicity (LogD), polar surface area (PSA) of the molecule, and fraction of rotatable bonds (f_{rb}). Although lipophilicity is commonly measured using logP, the logarithmic value arising from the partitioning of a neutral molecule between *n*-octanol and water, it does not take into consideration the potential ionisation of a molecule at different pH values; therefore logD, a distribution coefficient of hydrophobicity, may be a more apt descriptor[137,138]. LogD not only accounts for the lipophilicity of a molecule, but also considers the extent of ionisation experienced by the molecule at different pH levels; this is important when considering the pH of the body compartment for which a drug-like molecule is destined[108,137]. Polar surface area, along with logP/logD are often considered the most important factors in describing the properties of a drug[43]. PSA refers to the area of a molecule associated with oxygen and nitrogen atoms and their accompanying hydrogen atoms and is considered a good parameter for determining drug-likeness as it provides information about molecular polarity and solubility[43,139,140]. Lastly, we determined the fraction of rotatable bonds compared to the total number of bonds in a molecule. Rotatable bonds can be used as a 2D descriptor of molecular flexibility, they tend to increase with increasing molecular weight and are an important factor when considering the oral bioavailability of a drug compound[141–143]. Current literature suggests that a lower number of rotatable bonds makes for a good candidate drug molecule as this provides structural rigidity, which increases the likelihood of a compound binding to its prospective target ligand[141]. As a high molecular weight can result in an increased number of rotatable bonds, skewing prospective calculations, we opted to implement the fraction of rotatable bonds (f_{rb}) in our equation to normalise predicted permeation values for molecular size. We derived a formula from previous published data using these parameters to determine their role in mycobacterial cell wall permeation and calculated the predicted permeability values (P_{calc}) for a set of commercially available click chemistry fluorophores[108] (**Table 3.1**).

Table 3.1. Calculated molecular properties of commercially available click-adapted fluorophores

Compound	MW (g.mol^{-1})	log D (pH7.4)	PSA	f_{rb}	$P_{(calc)}$
Cyanine5.5 DBCO	1029.14	9.91	55.7	0.106	-2.515
Cyanine7 DBCO	885.62	8.92	55.7	0.107	-2.713
6-FAM-DBCO	676.71	8.65	84.9	0.074	-2.896
Sulfo-Cyanine3.5 Alkyne	1028.32	7.60	35.4	0.085	-2.904
Cyanine5 DBCO	929.03	7.93	55.7	0.117	-2.907
Cyanine7.5 Alkyne	722.4	7.07	35.4	0.091	-3.007
Cyanine3 DBCO	902.99	7.40	55.7	0.113	-3.015
Sulfo-Cyanine5 Alkyne	717.94	6.59	23.3	0.121	-3.045
Sulfo-Cyanine5.5 DBCO	1317.69	10.20	243.0	0.144	-3.193
Cyanine5.5 Alkyne	656.3	6.07	35.4	0.102	-3.203
AF568 Alkyne	807.97	6.49	64.3	0.057	-3.252
Sulfo-Cyanine3 DBCO	955.23	8.04	156.2	0.134	-3.281
6-R6G-Alkyne	495.57	5.73	38.3	0.086	-3.289
5-ROX-DBCO	835	5.80	64.9	0.065	-3.389
Cyanine7 Alkyne	622.28	5.09	35.4	0.104	-3.399
AF430 Alkyne	578.64	4.90	58.6	0.138	-3.517
Cyanine5 Alkyne	556.18	4.09	35.4	0.119	-3.593
Sulfo-Cyanine7 Alkyne	784.04	5.79	135.9	0.126	-3.653
Sulfo-Cyanine7.5 Alkyne	1120.46	7.41	222.7	0.136	-3.672
Cyanine3 Alkyne	530.14	3.57	35.4	0.113	-3.700
Sulfo-Cyanine5 DBCO	981.27	5.94	170.1	0.131	-3.758
Sulfo-Cyanine5.5 Alkyne	1054.36	6.68	222.7	0.150	-3.813
5-ROX-Alkyne	571.66	3.00	32.6	0.047	-3.826
BDP-581/591-DBCO	692.6	3.20	57.9	0.125	-3.859
Sulfo-Cyanine3 Alkyne	691.9	4.52	135.9	0.138	-3.903
5-FAM-Alkyne	413.38	3.16	105.1	0.040	-4.087
6-FAM-Alkyne	413.38	3.16	105.1	0.040	-4.087
AZDye 430 DBCO	761.81	3.16	133.32	0.124	-4.169
5/6-Texas Red-PEG4-Alkyne	819.98	3.45	155.77	0.142	-4.195
BDP-R6G_DBCO	640.53	1.25	57.4	0.112	-4.252
TAMRA PEG4 DBCO	936.06	3.24	171.04	0.159	-4.292
5-TAMRA-Alkyne	**467.51**	**1.63**	**84.7**	**0.063**	**-4.303**
6-TAMRA-Alkyne	**467.51**	**1.63**	**84.7**	**0.063**	**-4.303**
TAMRA Alkyne	**467.52**	**1.63**	**84.71**	**0.063**	**-4.303**
AFDye 405 Alkyne	**619.47**	**2.74**	**168.44**	**0.185**	**-4.372**
BDP-FL DBCO	**592.49**	**0.43**	**57.4**	**0.107**	**-4.418**
BDP 581/591 Alkyne	**429.27**	**-0.09**	**37.0**	**0.123**	**-4.435**
BDP 630/650 Alkyne	**487.33**	**-0.17**	**46.3**	**0.119**	**-4.489**
BDP 650/665 Alkyne	**470.28**	**-0.11**	**62.6**	**0.119**	**-4.543**
AZDye 430 Alkyne	**540.55**	**0.5**	**113.01**	**0.152**	**-4.610**
Sulfo-Cy5.5-Alkyne	**954.14**	**1.76**	**198.46**	**0.116**	**-4.713**

TAMRA PEG4 Alkyne	**643.73**	**0.03**	**121.63**	**0.176**	**-4.730**
BDP TR Alkyne	**461.29**	**-1.36**	**46.3**	**0.109**	**-4.731**
BDP TMR Alkyne	**435.28**	**-1.66**	**46.3**	**0.102**	**-4.793**
Carboxyrhodamine 110 DBCO	879.97	1.36	216.4	0.167	-4.846
Sulfo Cy5 DBCO	1009.22	1.47	221.6	0.136	-4.856
BDP R6G Alkyne	377.2	-2.27	37.0	0.102	-4.878
BDP 558/568 Alkyne	383.22	-2.45	37.0	0.109	-4.912
Sulfo Cy3 DBCO	983.18	0.94	221.6	0.133	-4.963
Carboxyrhodamine 110 Alkyne	587.63	-0.43	166.99	0.190	-4.998
BDP FL Alkyne	329.15	-3.09	37.0	0.091	-5.046
Cy7 DBCO	1259.53	1.24	275.97	0.133	-5.121
Cy5.5 DBCO	1175.37	1.18	275.97	0.116	-5.139
5/6-FAM-PEG4-DBCO	881.94	-0.46	199.26	0.169	-5.141
AF546 DBCO	1104.15	-0.41	231.9	0.079	-5.294
Sulfo Cy5 Alkyne	787.96	-1.19	201.29	0.158	-5.299
AZDye 594 DBCO	980.1	-0.87	216.59	0.080	-5.324
AFDye 546 Alkyne	855.34	-1.19	213.2	0.082	-5.374
AZDye 350 Alkyne	350.34	-2.78	135.79	0.103	-5.375
Sulfo Cy3 Alkyne	761.93	-1.72	201.29	0.155	-5.406
AF647 DBCO	1131.36	-0.83	275.97	0.159	-5.525
AZDye 680 DBCO	1086.73	-1.84	234.83	0.157	-5.563
AZDye 555 DBCO	1105.32	-1.35	275.97	0.156	-5.630
AF594 DBCO	980.28	-2.47	213.76	0.079	-5.633
MB660R DBCO	1003.19	-2.01	240.36	0.114	-5.635
AZDye 568 DBCO	953.04	-2.14	233.51	0.083	-5.645
AZDye 405 DBCO	774.79	-2.92	212.52	0.103	-5.710
AF546 Alkyne	885.25	-3.06	211.59	0.083	-5.741
AZDye 594 Alkyne	758.18	-3.52	196.28	0.085	-5.771
AF647 Alkyne	910.1	-3.48	255.66	0.184	-5.965
AZDye 680 Alkyne	865.47	-4.5	214.52	0.183	-6.005
AZDye 350 DBCO	722.14	-4.06	239.57	0.119	-6.040
AZDye 555 Alkyne	883.06	-4.01	255.66	0.182	-6.072
MB660R Alkyne	781.93	-4.67	220.05	0.129	-6.081
AF594 Alkyne	759.19	-5.13	193.45	0.084	-6.082
AZDye 568 Alkyne	731.39	-4.8	213.2	0.090	-6.093
AZDye 488 DBCO	792.79	-3.95	257.38	0.079	-6.104
AF488 DBCO	792.12	-5.19	257.38	0.079	-6.352
AZDye 488 Alkyne	571.53	-6.61	238.81	0.085	-6.560

*MW (molecular weight), PSA (polar surface area), frp (fraction of rotatable bonds), $P_{(calc)}$ (calculated permeation value), DBCO (dibenzocyclooctyne).

** Compounds displaying the best qualities of a good permeator are highlighted in blue.

It is assumed that a low polar surface area, small fraction of rotatable bonds and high lipophilicity (high logD) impart good cell wall penetration ability. However, an intermediate set of values stands to be more beneficial as a compound that is too lipophilic may easily enter the cell wall itself but not be able to pass into the cytosol to reach its target. Similarly, if a compound is too hydrophilic, it may be readily soluble but will have difficulty entering the lipid-rich mycomembrane. Therefore, a small range of intermediate $P_{(calc)}$ values was determined to predict good cell wall permeation based on previous work; here, we define molecules with a $P_{(calc)}$ between -4.30 and -4.70 to be good permeators of the mycomembrane[108]. Compounds displaying the best qualities of a good permeator are highlighted in **Table 3.1** and mean values of each molecular property that contributes to this range of values can be seen in **Table 3.2**.

Table 3.2. Mean values of calculated molecular properties

$P_{(calc)}$	log D(pH7.4)	PSA	f_{rb}	MW ($g.mol^{-1}$)
-4.3 to -4.7	0.535	88.577	0.115	541.259
< -4.7	-1.943	213.493	0.124	848.535
> -4.3	5.407	90.683	0.110	768.195

*PSA (polar surface area), f_{rp} (fraction of rotatable bonds), MW (molecular weight).

From **Tables 3.1** and **3.2**, it was evident that the logD values resulting in a desirable $P_{(calc)}$ were much lower than anticipated, in turn suggesting that a high degree of lipophilicity was not a desirable factor in predicting permeation. This was somewhat surprising as the mycomembrane is lipid-rich and we would expect to see a logD value higher than 1. Yet, as previously mentioned, this may be beneficial to mycobacterial permeation as, once a compound passes through the cell wall, it must enter the more hydrophilic cytoplasm to reach its molecular target. Furthermore, even though the mean logD value for predicted effective permeation was low (**Table 3.2**), it was still a positive integer, indicating that the set of compounds were more lipophilic than hydrophilic (negative logD values). This observation bolstered the notion that intermediate values might be optimal for permeation – ideal compounds are marginally lipophilic, allowing entry into the mycobacterial cell but not too lipophilic to prevent entry into the cytosol. The PSA and MW values of desirable compounds were both low, indicating a small, low polarity molecule is a suitable candidate for permeation. The fraction of rotatable bonds in compounds with good predicted permeability were close to the lower end of the range, indicating that molecular rigidity was likely beneficial when entering a mycobacterial cell. Therefore, all findings from the applied equation fit the previously described criteria for predicting a good cell wall permeator.

To investigate the *in vitro* applicability of predicted permeability, a subset of fluorophores with P_{calc} values predicting "good" or "bad" permeation was selected for microscopic analysis. Our objectives were twofold: firstly, to analyse the effects of the alkyne and dibenzocyclooctyne (DBCO) moieties on permeation and, secondly, to determine whether uptake of the selected fluorophores mirrored the predicted permeation qualities defined *in silico*. Therefore, we selected three fluorophore backbones with different predicted permeation qualities to ascertain the impact of each moiety in addition to verification of the P_{calc} (**Table 3.3**). Upon analysis of **Table 3.3**, it was apparent that addition of the DBCO moiety increased MW, logD (suggesting increased lipophilicity), and PSA of the fluorescent backbone. The increased MW most likely explained the rise in PSA values and was considered of little significance as logD is the major contributing factor when determining P_{calc}. These observations suggested that molecules carrying the DBCO moiety might be capable of entering the cell wall but, owing to their lipophilic qualities, would struggle to reach the cytoplasm. When comparing the fluorescent backbones of these molecules, we saw that a low logD value, indicating reduced lipophilicity, gave a more favourable P_{calc}, reinforcing the notion that logD is a critical factor in determining permeation into the cell cytoplasm.

Table 3.3. Selected click-adapted fluorophores for *in vitro* evaluation of predicted permeability

Compound	$P_{(calc)}$	logD (pH7.4)	PSA	f_{rb}	MW ($g.mol^{-1}$)
Cy3 Alkyne	-3.70	3.57	35.40	0.11	530.14
Cy3 DBCO	-3.28	8.04	156.2	0.13	955.23
ROX Alkyne	-3.83	3.00	32.6	0.05	571.66
ROX DBCO	-3.39	5.80	64.90	0.07	835.00
TAMRA Alkyne	-4.30	1.63	84.70	0.06	467.51
TAMRA DBCO	-4.29	3.24	171.04	0.16	936.06

*Suppliers listed in Materials and Methods.
**Molecular structures in Supplementary Table 1.

COMPARISON OF ALKYNES AND DIBENZOCYCLOOCTYNES (DBCOS)

Initial experiments set out to determine whether the addition of the bulky DBCO moiety negatively impacted the ability of the fluorophore backbone to enter *Msm* bacilli, as was predicted *in silico*. Cultures were incubated in triplicate with AHA for 3 hours before staining with selected fluorophores. For the Cy3 and TAMRA backbones, there was a significant decrease in fluorescence for the DBCOs when compared to the alkynes (**FIGURE 3.3 A & B**). This suggested that the bulky DBCO moiety significantly impacted the ability of the molecules to reach the cytoplasm, an observation in agreement with the prediction of increased molecular weight inhibiting passage through the cell wall. The high logD value of 8.04 calculated for Cy3 DBCO suggested that the DBCO side chain considerably increased lipophilicity, as

compared to the logD of 3.57 calculated for Cy3 alkyne, likely further contributing to the reduced ability of the molecule to enter the cytoplasm. Furthermore, both TAMRA and Cy3 DBCOs exhibited high PSA values of 171.04Å and 156.2Å, respectively, further diminishing their permeation capabilities due to raised polarity. Conversely, the greater fluorescence observed for the Cy3 and TAMRA alkynes might be attributable to their relatively small size, decreased lipophilicity and comparatively low PSA values.

The ROX DBCO fluorophore displayed significantly higher fluorescence than its alkyne counterpart (**FIGURE 3.3C**). Although this was not predicted given the permeation parameters of this molecule, we observed that it possessed logD and MW characteristics similar to those of the other DBCOs but its PSA value of 64.9Å was significantly lower. It was possible this reduction in surface polarity proved beneficial in gaining access to the cell wall. Notably, while ROX DBCO exhibited greater fluorescence than its alkyne counterpart, we observed a unique pattern of fluorescence localization to the cell envelope, suggesting the inability of the molecule to enter the cytoplasm (**FIGURE 3.3C**). This might be ascribed to its high logD value of 5.8, resulting in a level of lipophilicity that promoted association with the lipid-rich cell wall.

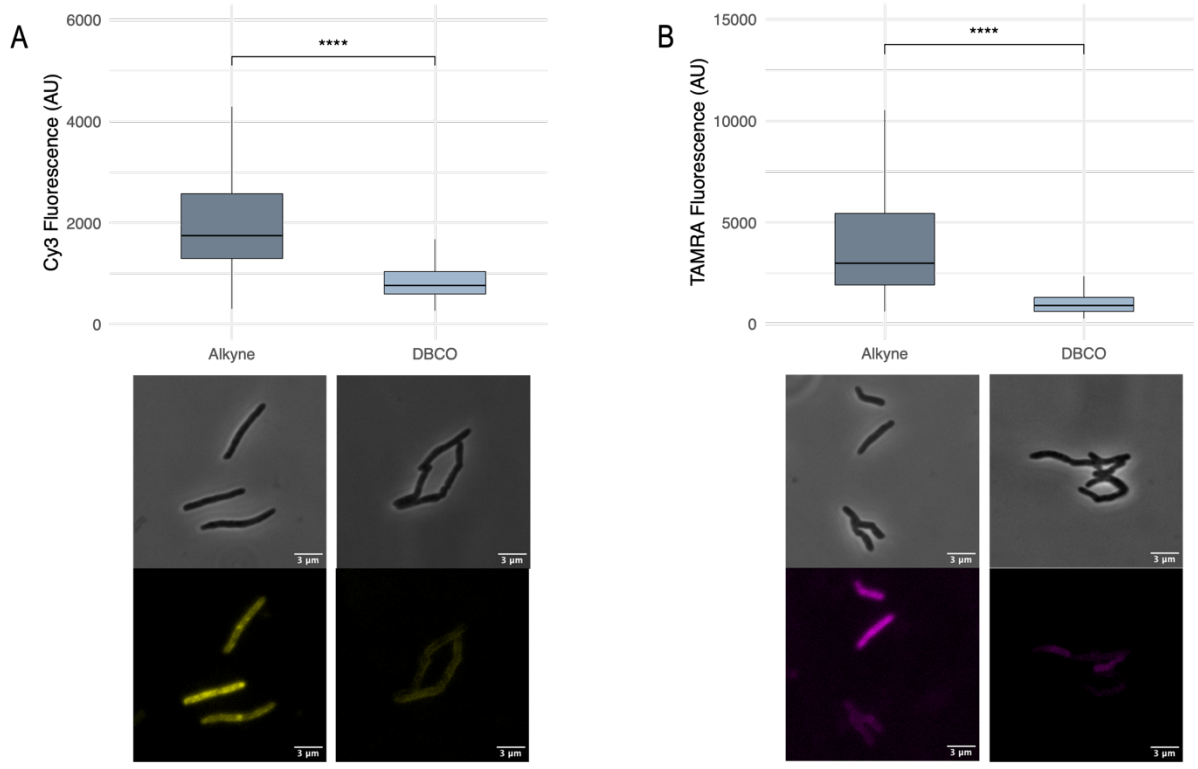

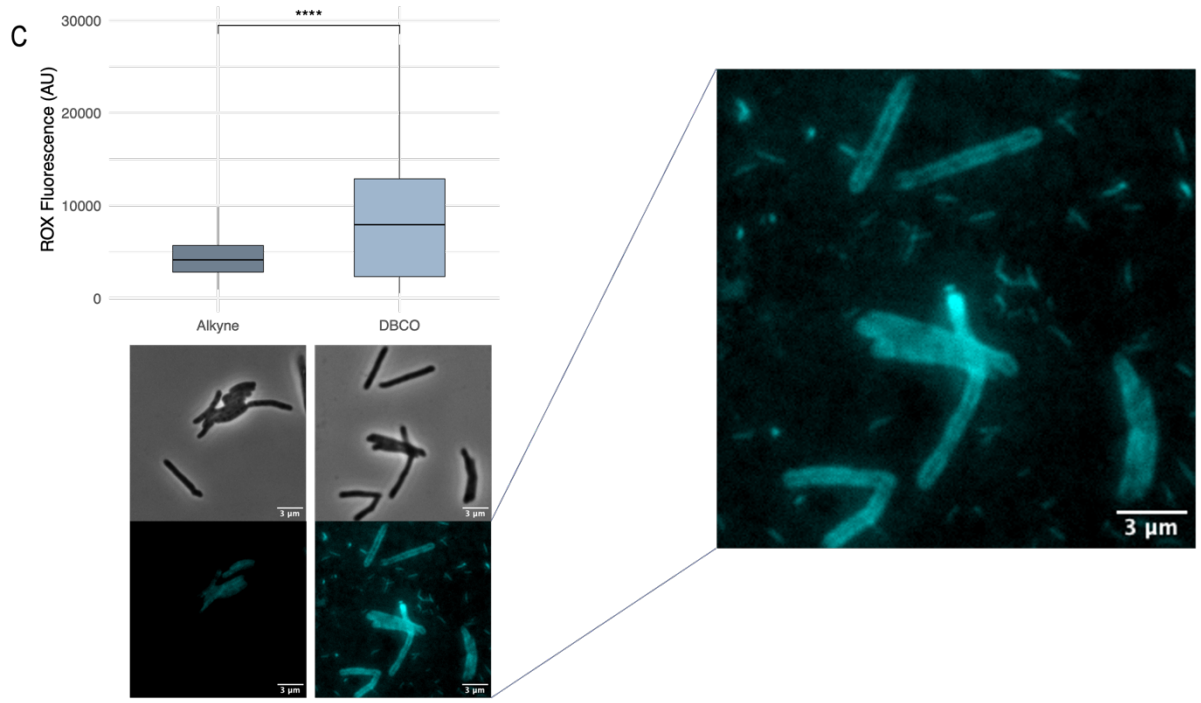

FIGURE 3.3. Alkyne and DBCO functional groups affect total fluorescence. Whole-cell fluorescence was compared between alkyne- and DBCO-linked Cy3 (A), ROX (B) and TAMRA (C). Top panels of each figure show fluorescence across each population and bottom panels display representative images of *Msm* stained with the corresponding fluorophore. The ROX DBCO fluorescent image has been enlarged for the purpose of highlighting fluorescence localization in the sample. Fluorescence was visualized using a Zeiss Axio Observer inverted fluorescence microscope and quantified using ImageJ software. For each condition, 100 cells were measured in triplicate. An Independent t-test was used to determine significance, p=0.005).

ENHANCING THE UPTAKE OF FLUORESCENT PROBES

Next, we set out to determine the effect of cell wall permeabilization on fluorophore uptake. The comparatively poor permeation characteristics of the Cy3 alkyne relative to the other two alkynes in both *in silico* predictions and the initial staining experiments made it a good candidate for an experiment aimed at determining the best method of increasing fluorophore uptake by *Msm*. Based on commonly applied fixation and permeabilization protocols, we assessed the efficacy of paraformaldehyde (PFA), a cross-linking agent, and ethanol, a denaturing agent, in enhancing fluorescent signal of Cy3 alkyne[144,145]. Bacteria were treated with 4% PFA or 80% ethanol before staining and compared to untreated organisms. Ethanol treatment showed a significant increase in fluorescence when compared to 4% PFA and untreated cells, suggesting its efficacy in increasing cell envelope permeability and enhancing uptake of Cy3 alkyne (**FIGURE 3.4**). This observation led us to proceed with 80% ethanol treatment as a means of permeabilization of samples before carrying out further BONCAT analyses.

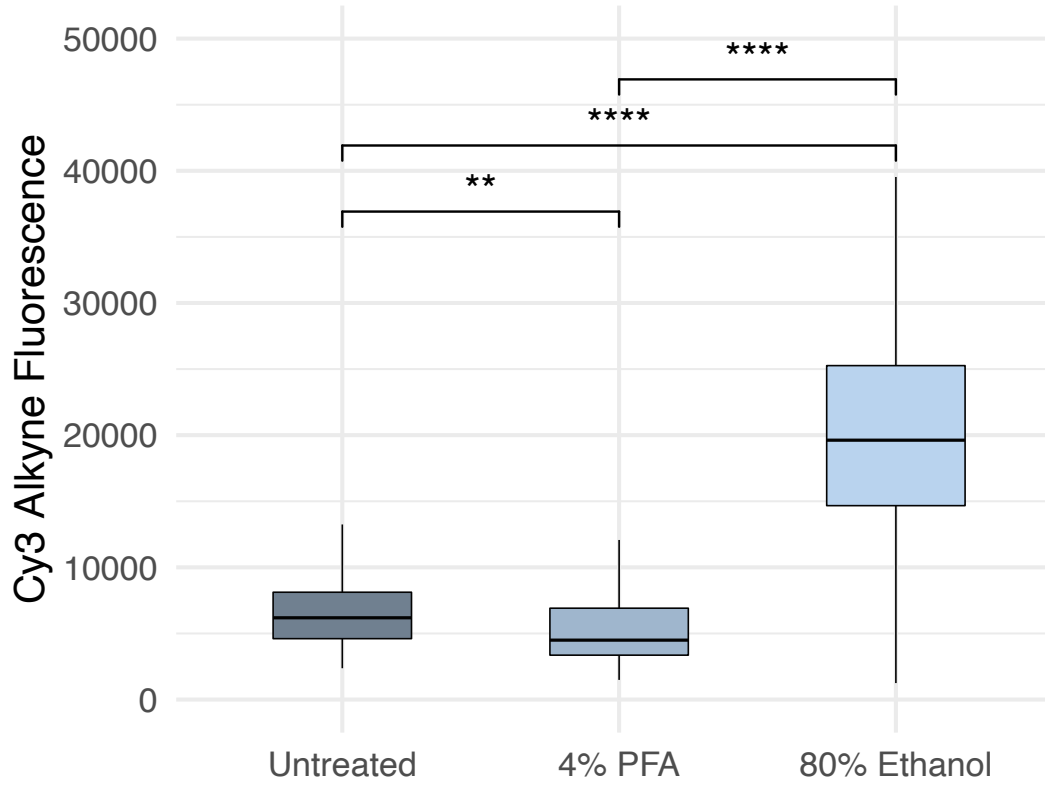

FIGURE 3.4. 80% ethanol increases fluorophore uptake. Whole-cell Cy3 alkyne fluorescence was compared between non-permeabilized, 4% PFA- and 80% ethanol-permeabilized samples. Fluorescence was visualized using a Zeiss Axio Observer inverted fluorescence microscope and quantified using ImageJ software. For each condition, 50 cells were measured, and Student's t-test was used to determine significance between samples, p=0.005.

Cultures were grown as before, and an 80% ethanol permeabilization step was incorporated into the protocol before proceeding with cell staining. The purpose of this experiment was to investigate whether heterogeneity in fluorophore uptake was due to the varying abilities of individual cells to allow entry into the cytoplasm or, alternatively, a true representation of metabolic heterogeneity as a function of differences in protein synthesis (and thus uptake of AHA) between individual bacilli. Across all 6 fluorophores, there was a significant increase in whole-cell fluorescence upon permeabilization, indicating that 80% ethanol treatment enhanced the ability of the fluorophores to gain entry to the cytoplasm of *Msm* (**FIGURE 3.5**). For Cy3 and TAMRA (**FIGURE 3.5 A, B, E & F**), it was noticeable that DBCO-containing fluorophores exhibited lower fluorescence than their alkyne counterparts following permeabilization of the cell envelope, confirming our initial observations that DBCOs were poor permeators of the mycobacterial cell envelope. As noted in the previous experiment, this was not the case for ROX, with the DBCO variant exhibiting a higher level of fluorescence than the alkyne. However, it was interesting to note that, even with 80% ethanol permeabilization, ROX DBCO still exhibited fluorescent localization to the exterior of the cell (**FIGURE 3.5D**). This suggested that, although the cell

wall had become more permissive to the entry of molecules, this lipophilic probe preferred the lipid-rich environment of the cell wall. In contrast, all other fluorophores used in this experiment exhibited a diffuse fluorescence signal throughout the cell, indicative of uptake into the cytoplasmic region.

When addressing the dilemma of permeability *versus* metabolic heterogeneity, this experiment allowed for visualisation of the variation in single-cell fluorescence under permeabilized and non-permeabilized staining conditions. We postulated that permeabilization of the several layers encapsulating the bacilli would, to some extent, eliminate the concern that single-cell heterogeneity was linked to the inability of some cells to take up a fluorophore. Consequently, we noticed an increase in the spread of data in all fluorescent probes when subjected to 80% ethanol permeabilization (**FIGURE 3.5**). Our tentative conclusion was that the variability in these cells could be ascribed to heterogeneous protein synthesis, given that the confounder of cell-cell heterogeneity in permeability was reduced through ethanol treatment.

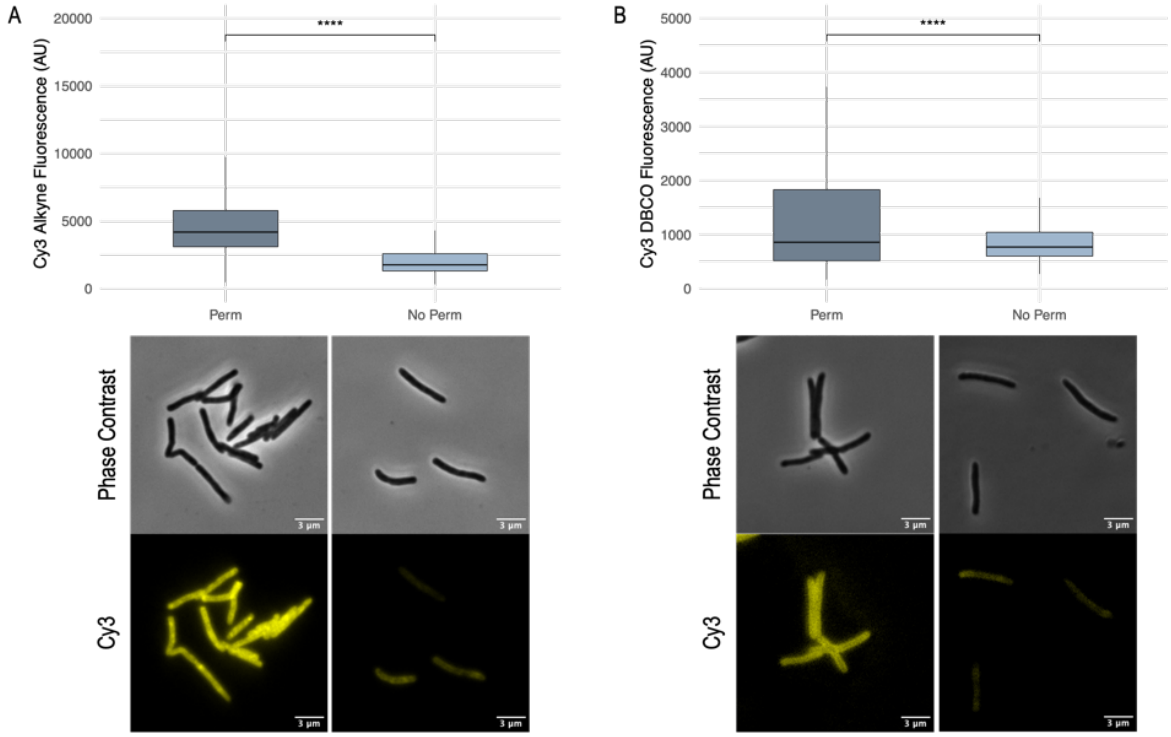

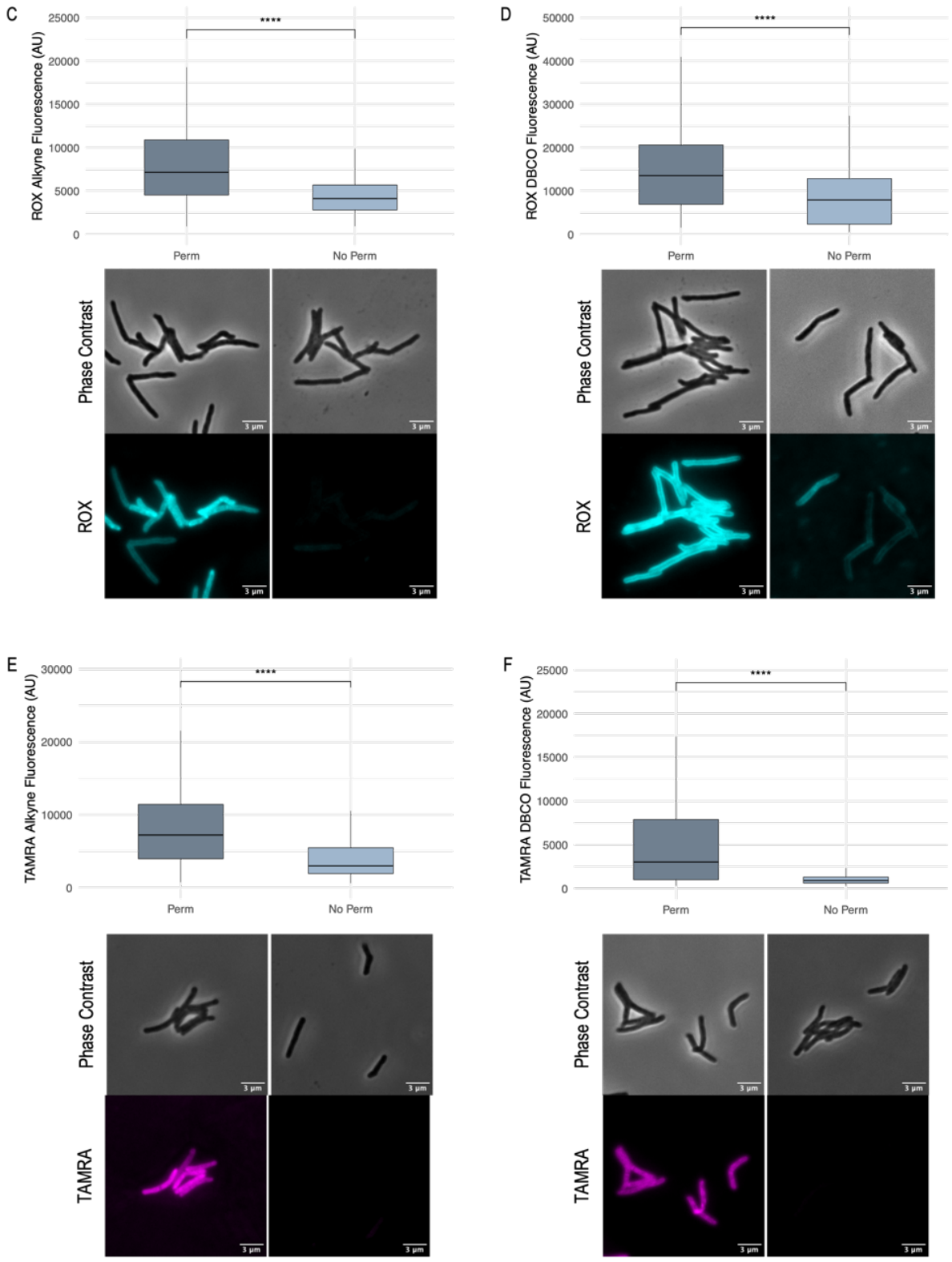

FIGURE 3.5. Permeabilized cells show elevated fluorescence for all fluorophores. Whole-cell fluorescence was compared between non-permeabilized (No Perm) and 80% ethanol-permeabilized (Perm) samples . The three fluorophore backbones used were Cy3, ROX and TAMRA; the alkyne-linked probes are visualized in A,C and E and the DBCO-linked probes are visualized in B, D and F. Top panels of each figure show fluorescence across each population and bottom panels display representative images of *Msm* stained with the corresponding fluorophore under the different conditions. Fluorescence was visualized using a Zeiss Axio Observer inverted fluorescence microscope and quantified using ImageJ software. For each condition, 100 cells were measured in triplicate and Student's t-test was used to determine significance between samples, p=0.005.

INVESTIGATING MYCOBACTERIAL METABOLIC ACTIVITY USING BONCAT

After verifying that 80% ethanol permeabilization increased uptake of fluorescent probes, in turn providing a more authentic representation of metabolic heterogeneity within a cell population, we proceeded to investigate the effect of protein synthesis inhibition on BONCAT fluorescence in permeabilized samples. Cultures were pre-exposed to streptomycin, an aminoglycoside that binds irreversibly to the mycobacterial 30S ribosomal subunit, interfering with protein synthesis[54]. Cells were treated at ¼× MIC (0.67µM) for 3h before 3h labelling with AHA and subsequent staining. Across all fluorophores, a significant decrease in fluorescence was observed following streptomycin treatment (**FIGURE 3.6**). These results indicated that pre-incubation of cultures with a protein synthesis inhibitor reduced the level of newly synthesized proteins that incorporated AHA, decreasing availability of the azide tag to which the click fluorophores could bind. Furthermore, we observed reduced variance among bacterial populations treated with streptomycin, potentially indicative of greater homogeneity in protein expression. This result was consistent with our previous findings suggesting that observed fluorescence was not solely dependent on permeation of molecules but was also a function of changes in protein synthesis levels, thus providing an indication of altered metabolic activity in single cells.

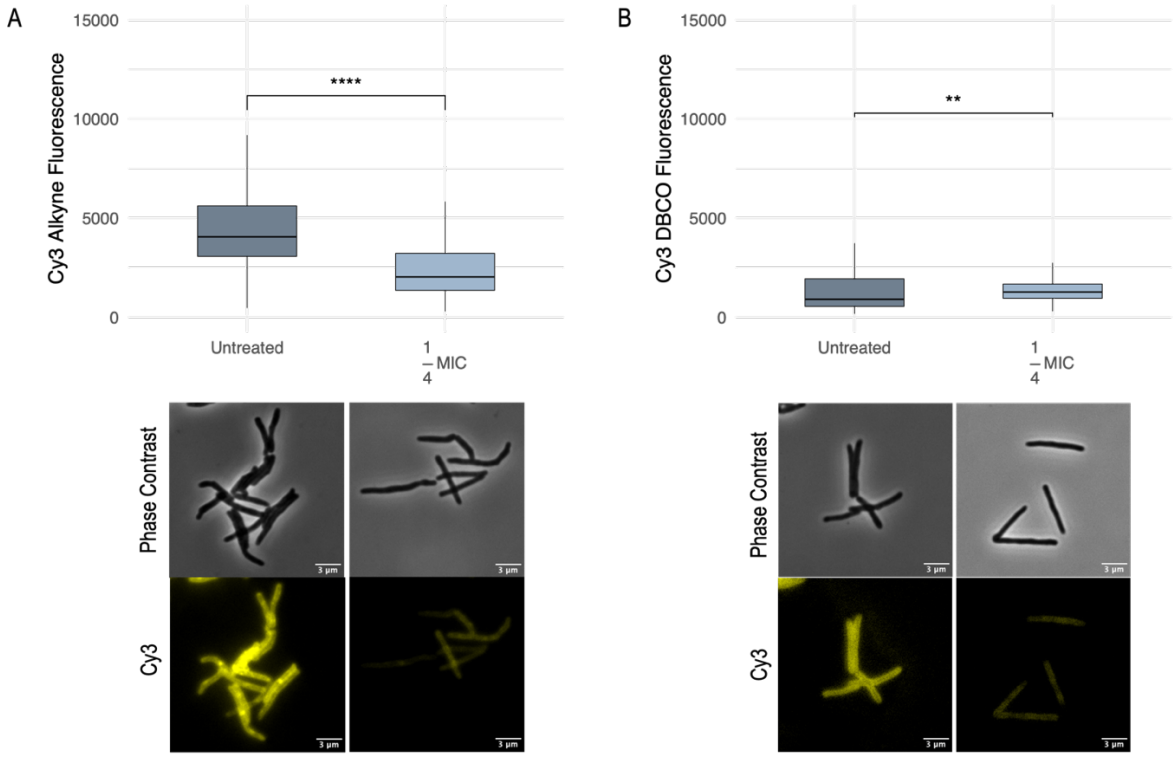

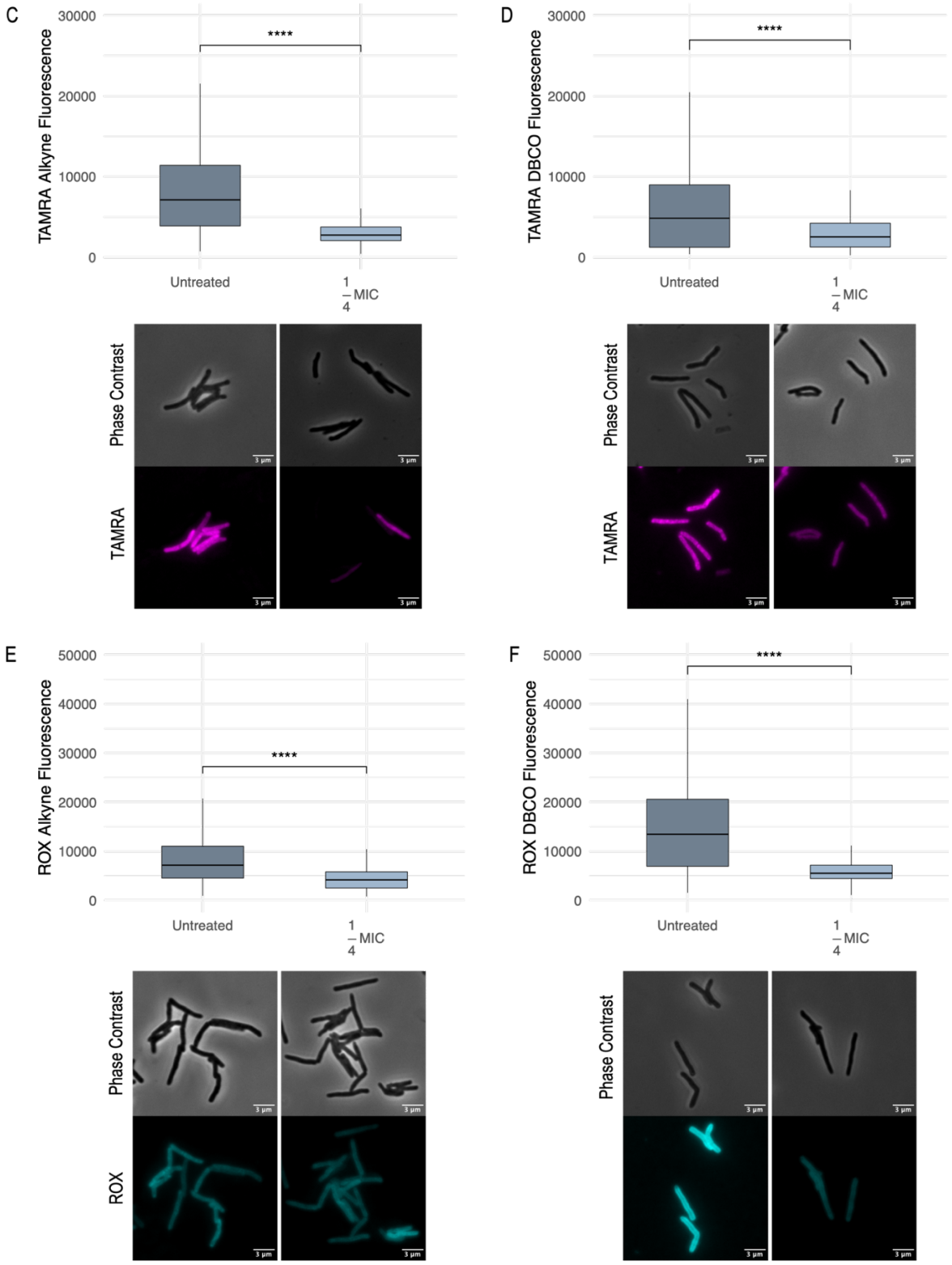

FIGURE 3.6. Streptomycin treatment decreases total fluorescence. Whole-cell fluorescence was compared between untreated samples and samples exposed to streptomycin at ¼ MIC. The three fluorophore backbones used were Cy3, ROX and TAMRA; the alkyne-linked probes are shown in A,C and E and the DBCO-linked probes are shown in B, D and F. Top panels of each figure show fluorescence across each population and bottom panels display representative images of *Msm* stained with the corresponding fluorophore under the different conditions. Fluorescence was visualized using a Zeiss Axio Observer inverted fluorescence microscope and quantified using ImageJ software. For each condition, 100 cells were measured in triplicate and Student's t-test was used to determine significance between samples, p=0.005.

APPLICATION OF AZIDE-FUNCTIONALIZED DRUGS

BONCAT proved useful in characterizing the molecular properties required by a compound to allow effective penetration of the mycobacterial cell envelope. However, as we set out to develop this as a tool to inform drug discovery, we wanted to see if this technique could be applied to drugs known to be active against *Mtb*. A small panel of azide-functionalized antibiotics was obtained through collaboration with Prof. Mark Blaskovich (Institute for Molecular Bioscience, University of Queensland, Australia). Initial assessments of minimum inhibitory concentration (MIC_{90}) were conducted to ensure addition of the azide group did not alter the antibiotic efficacy against *Msm*. For all azide-functionalized drugs, we found no reduction in efficacy compared to the native molecules (**Table 3.4, Supplementary Information 1**). This was an important result as it implied the addition of the azide moiety had no impact on the mechanism of action of the respective compounds. Based on the innate inactivity of trimethoprim and polymyxin against mycobacteria, these drugs were excluded from further analyses.

The assumption was made that the azide-functionalized drugs would accumulate within cells at a much lower concentration than that of the previously investigated methionine analogue (AHA). Therefore, we opted to utilize a fluorogenic probe to eliminate any potential background fluorescence caused by unreacted probe. Based on methods reported by the Bertozzi lab, our collaborators in the Barry laboratory (NIH/NIAID) completed synthesis of coumBARAC, a DBCO derivative reported to undergo a 10-fold increase in fluorescence following triazole formation[123].

Table 3.4. MIC_{90} values (µm) for azide-functionalized drugs and native compounds

	Roxithromycin	Trimethoprim	Polymyxin	Vancomycin	Linezolid
Native Compound	1.25	25	No action	1.25	3.125
Azide-functionalized Compound	1.25	50	No action	0.3125	6.25

Fluorescence microscopy was performed utilizing azide-functionalized roxithromycin, vancomycin and linezolid, all anti-mycobacterial compounds involved in impeding protein synthesis. *Msm* cultures were incubated with azide-functionalized drugs at 1× and 2× MIC_{90} for 3h before carrying out click chemistry with coumBARAC to allow for observation of drug uptake. Unfortunately, we observed fluorescence in our treated samples that was only marginally higher than that of the untreated controls. Linezolid-azide showed the most promising indication of successful labelling, giving a strong fluorescent readout at 2× MIC_{90} (**FIGURE 3.7, top panel**). Both roxithromycin-azide and vancomycin-azide were unable to generate fluorescence higher than that seen in the controls (**FIGURE 3.7, middle and bottom panels**). Owing to these initial findings and limited amounts of both azide-functionalized drugs and coumBARAC, we were

not able to pursue this investigation further, including performing quantitative analyses on fluorescence readouts.

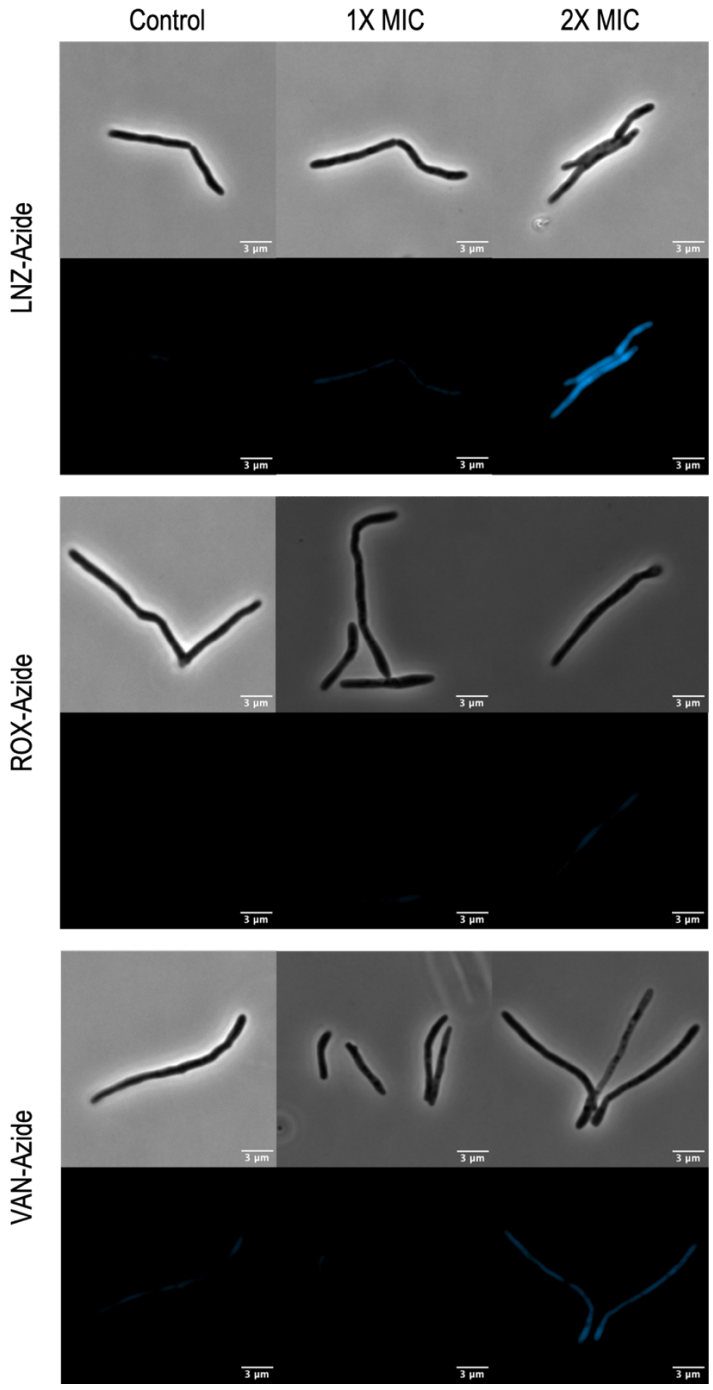

FIGURE 3.7. Azide-functionalized drugs show weak fluorescent signal. Representative images of fluorescence in *Msm* following click chemistry tagging with a fluorogenic probe (coumBARAC) of linezolid-azide (top panel), roxithromycin-azide (middle panel) and vancomycin-azide (bottom panel) at 1× and 2× MIC_{90}. Untreated cells were used as a control for autofluorescence. Fluorescence was visualized using a Zeiss Axio Observer inverted fluorescence microscope and processed using ImageJ software.

Discussion

MOLECULAR PROPERTIES THAT IMPACT PERMEATION

The ability to cross the cell membrane and enter the cytoplasm to reach its desired target is a crucial factor in determining the success of candidate drug compounds, and is complicated by the presence of a cell wall in bacteria[138,146]. The peptidoglycan layer in the majority of bacteria presents an array of difficulties in the penetration of molecules, and is compounded in mycobacteria by the presence of the lipid-rich mycolic acid and arabinogalactan layers[146]. The inability to predict in advance – or even determine rapidly downstream – whether a compound possesses the capacity to penetrate the mycobacterial cell wall presents a serious obstacle to rational medicinal chemistry efforts. In addition to penetrating the mycobacterial cell wall, anti-TB drugs need to first gain access the various host environments in which the bacillus resides[45]. These barriers to drug discovery emphasize the critical need for developing a set of permeation parameters that effectively inform rational drug design[102]. Important molecular descriptors of permeation include polar surface area (PSA) and hydrophilicity (logP/logD)[138,139]. PSA is defined by the presence of oxygen and nitrogen atoms on the surface of a molecule and high PSA values are commonly associated with poor permeation of molecules[139,140]. The lipophilicity of compound can be ascertained using logD, a pH-dependent descriptor that indicates the ability of a molecule to pass through a hydrophobic barrier such as the lipid-rich mycomembrane[138,146]. Finding a molecule with qualities that accommodate both entry into infected tissues and immune cells and through the lipophilic mycobacterial cell envelope presents a significant challenge to medicinal chemists[45,102]. As a result, there is a general lack of permeation data, meaning that structure-activity relationship (SAR) analyses are incapable of determining whether loss of activity in a close analogue of an “active” molecule results from differential permeation, bacillary-mediated biotransformation, efflux, or disruption of target engagement. Although click chemistry is widely used in the process of lead optimization as it provides a rapid and reliable means of molecular modification, this study set out to evaluate the applicability of click chemistry as a tool for enhancing our understanding of permeation in rational drug design, and to aid in differentiating true inactivity from lack of permeation[147].

When analysing the molecular structure of commercially available click chemistry fluorophores in relation to permeability of the mycobacterial cell wall, several distinguishing features arose. First, the majority of good permeators were alkynes, indicating that the dibenzocyclooctyne (DBCO) moiety is a hindrance when passing through the cell wall. This is unsurprising when considering the molecular weight of each component, with alkynes having a mass of just 15g.mol^{-1} in contrast to the 206g.mol^{-1} of DBCOs.

Furthermore, the addition of a DBCO moiety often resulted in an increased logD value, indicating its role in elevating hydrophobicity. These observations suggest that, although the strained-ring conformation of DBCOs provides the benefit of cycloaddition in the absence of the potentially toxic levels of copper required to promote the conventional click chemistry reaction, the unfavourable qualities associated with their bulky configuration may outweigh their utility in this context[112]. We also noted that many of the compounds predicted to have desirable permeation qualities were derivatives of the BODIPY and TAMRA skeletons (**FIGURE 3.8**). The logD values showed the closest association with generating a good P_{calc} value, supporting the notion that this pH-dependent descriptor of lipophilicity is key in determining effective compound permeation[137,148]. Both BODIPY and TAMRA derivatives displayed intermediate logD values ranging from -1.66 to 1.63, suggesting the necessity for a degree of lipophilicity that allows penetration of the lipid-rich cell envelope but does not exceed levels that become detrimental to cytoplasmic entry. Polar surface area also proved an important factor in determining permeation, with most good permeators exhibiting low PSA values ranging from 37Å to 85Å; this is in agreement with research that indicates a high level of surface polarity negatively impacts permeation[108]. Lastly, the size and compact nature of TAMRA and BODIPY backbones (192g.mol^{-1} and 430g.mol^{-1}, respectively) are likely an important contributing factor in penetration of the mycomembrane. Compounds that showed poor permeability tended to be bulky, with molecular weights exceeding 650g.mol^{-1} and a PSA greater than 200Å, conferring poor penetrating capabilities. These characteristics were accompanied by either a highly negative logD value (< -1.7), suggesting a very hydrophilic molecule that would not be able to pass through the lipid-rich mycomembrane, or a highly positive logD value (> 2.8), indicating a molecule that is too lipophilic and runs the risk of getting trapped in the mycomembrane. Collectively, these *in silico* observations may provide insight into future drug discovery: current research tends to focus strongly on drug-like factors required for efficient host absorption and more emphasis should potentially be placed on the ability of the drug to enter the infecting organism[45]. This calls for an intermediate range of desired values that take into consideration both host and pathogen permeation.

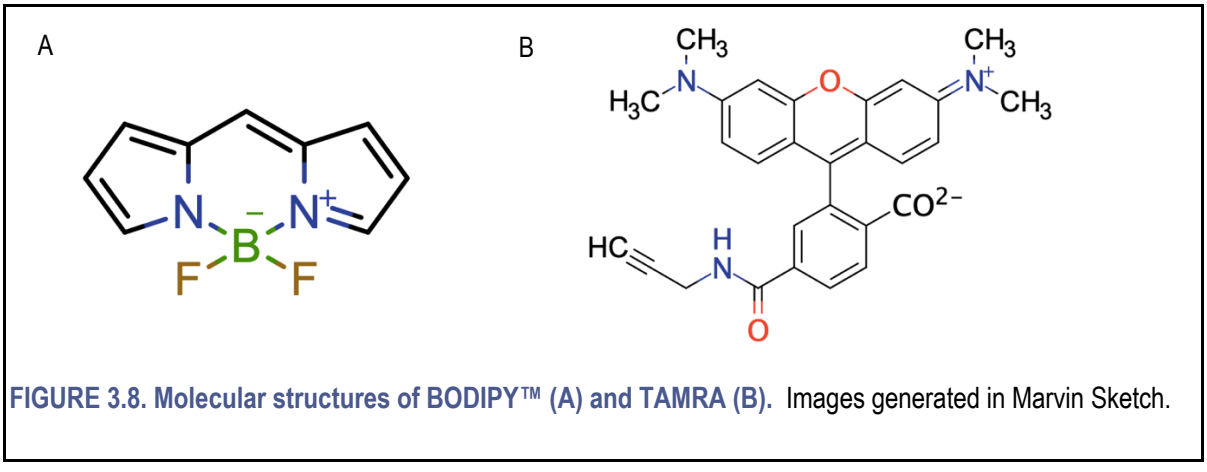

FIGURE 3.8. Molecular structures of BODIPY™ (A) and TAMRA (B). Images generated in Marvin Sketch.

BONCAT FOR THE EVALUATION OF PERMEABILITY

Determining the parameters that define a good permeator is essential in the rational design of drugs to ensure that a compound is capable of reaching its intended target. This is especially true in the development of anti-TB drugs as the thick, lipid-rich mycobacterial cell envelope presents a robust barrier to the entry of many molecules[102]. Extensive research has been directed towards defining permeation parameters for the mycobacterial cell wall as it presents an intrinsic mechanism of drug resistance that can prevent even the most potent drugs from reaching their targets[44,102]. *In silico* drug design allows for rapid evaluation of large compound libraries to assess permeability of the *Mtb* cell wall by applying various models based on molecular descriptors of structures predicted to exhibit effective penetration[101]. Although these bioinformatic approaches are powerful in their high throughput capabilities, there is a need for empirical validation of these permeability predictions. This is further confounded by the inefficiency of current approaches utilized to inform lead compound potency to provide an accurate representation of *Mtb* infection, where enzyme inhibition assays fail to account for permeation and minimum inhibitory concentration assays in standard laboratory media do not take the metabolic state of *Mtb* in the harsh environmental niches of the host into consideration[89,101].

This set of experiments intended to discern the potential application of BONCAT as a means of ascertaining molecular permeation of the mycobacterial cell wall through fluorescent readouts. The methionine analogue, AHA, can be readily incorporated into newly synthesized proteins due to the promiscuity of tRNAs and promises good coverage due to the high prevalence of methionine residues across bacterial proteins[130]. We expected to observe fluorescence only when the click-adapted fluorophores gained entry into the cytoplasm and underwent cycloaddition with AHA; these assays, in conjunction with *in silico* permeability prediction, provided a platform to establish molecular attributes of compound penetration.

When determining the impact of click chemistry moieties on fluorophore permeation, experimental findings showed close association with *in silico* predictions. The impact of molecular weight was made apparent in the decreased fluorescence of the Cy3 an TAMRA DBCOs in comparison to their alkyne counterparts, a finding in agreement with the permeation parameters set out by Christopher Lipinski in defining a molecule with MW > 500g.mol^{-1} as being a poor permeator[41,42]. The DBCO moiety also severely impacted logD, increasing its value to result in a highly lipophilic compound that cannot gain access to the cell at all (as seen for Cy3 and TAMRA DBCOs) or inhibiting its ability to pass beyond the lipid-rich cell envelope and enter the cytoplasm (as seen for ROX DBCO). PSA exhibited a similar

elevation in DBCOs, contributing a further adverse effect on permeation, as has been observed in previous studies in mammalian cells[149]. The known difference in reaction kinetics of alkyne and DBCOs was addressed during method development, ensuring extended incubation times for DBCOs which exhibit a slower reaction rate than their alkyne counterparts; however, this component of the study may warrant future investigation to fully distinguish the effects of molecular structure on observed fluorescence from those resulting from variations in reaction kinetics. The comparison of alkynes and cyclic alkynes performed here provides a basis for applying click chemistry to the understanding of mycomembrane permeation and the availability of several structurally distinct bio-orthogonal probes could be readily applied to augment this strategy in developing a set of permeation parameters that accurately inform rational drug design[113].

PERMEABILIZING THE MYCOBACTERIAL CELL ENVELOPE

The mycobacterial cell envelope constitutes a robust barrier to the entry of antibiotics, posing a critical impediment to drug discovery[150]. As such, a thorough understanding of the composition of the mycomembrane and the mechanisms by which it regulates entry of molecules is paramount in informing rational drug design[33]. The cell envelope of *Mtb* is a highly lipophilic environment that is capable of undergoing remodelling under different environmental stresses in order to survive in the various conditions presented by different sites of infection[151]. This makes the cell wall a desirable drug target, both via direct killing through inhibition of essential cell wall biosynthetic enzymes and indirectly by weakening structural integrity to allow easier access of compounds with intracellular targets[33,54].

The impenetrability of the mycobacterial cell envelope often requires harsh chemical treatment to allow for uptake of probes, commonly implementing degrading enzymes such as lysozyme to grant access to intracellular components of the bacillus[152]. However, lysozyme causes severe degradation of the peptidoglycan layer and can result in lysis, making this method unsuitable for our purposes[153]. Furthermore, lysozyme treatment is known to result in morphological changes and at elevated concentrations can almost completely degrade the cell wall; these observations form the basis of the second component of this work and are discussed in further detail in the subsequent chapter[154,155]. We opted to utilize treatment 80% ethanol to permeabilize the *Msm* cell envelope which resulted in a significant increase in total BONCAT fluorescence that effectively displayed the efficacy of this agent to destabilize the cell wall and allow for easier access of fluorophores to their intracellular target. These experiments exhibited not only the impenetrability of the mycomembrane but the inherent heterogeneity in permeability within a population that determines compound uptake on a single cell level.

METABOLIC HETEROGENEITY IN MYCOBACTERIA

Phenotypic heterogeneity is a well-documented phenomenon that occurs during *Mtb* infection as the bacteria adapt to the various environmental niches within the host and is now recognized as playing an essential role in the emergence of persisters[62,72,156]. This heterogeneity not only contributes towards effective in-host survival through changes in metabolic and physiological states, but also gives rise to variations in drug susceptibility experienced by a bacterial population[72]. The ability of a single bacillus within a population to enter a different metabolic state poses a major challenge for drug discovery as many antibiotics prove ineffective in the face of such heterogeneity[59]. As such, it is essential to invest ample research into understanding the level of heterogeneity present in mycobacterial populations and the mechanisms underlying this phenomenon to inform ration drug design. Here, we sought to apply BONCAT as a means of evaluating heterogeneity in protein expression on a single cell basis. The variance observed when analysing single cell BONCAT fluorescence demonstrated the extent to which a population of *Msm* growing under the same environmental conditions can exhibit cell-cell heterogeneity in protein synthesis. Treatment with streptomycin to inhibit protein expression revealed a decrease in population variance, suggestive of a more homogenous level of translational activity in response to antibiotic treatment. These findings emphasized the capacity for BONCAT, an inexpensive and easily applicable assay allowing for single cell analysis, as a proxy for enhancing our knowledge of phenotypic heterogeneity.

FLUORESCENT ANTIBIOTICS IN DRUG DISOVERY

The application of fluorescent antibiotics in evaluating drug-target interactions provides an intriguing strategy in advancing our ability to understand the mechanistic effects of antibiotic challenge on bacterial growth dynamics and metabolic activity[157]. Such techniques also provide scope for *in vivo* studies that give insight into bioavailability of drugs during host-pathogen interactions[157]. Taking advantage of the small molecular weight of fluorescein and the reactivity of an amine residue located on the vancomycin molecule, researchers were able to develop a fluorescent derivative of vancomycin to investigate peptidoglycan biosynthesis in *B. subtilis*[158,159]. Fluorophores such as fluorescein and BODIPY™ are preferable in development of fluorescent antibiotics due to their low molecular weight, limiting the effects of fluorescent tagging on target binding; however, the beneficial properties of click chemistry as a means of probing biological systems makes it attractive for visualizing antibiotic localization in live cells[157,160,161].

As previously mentioned, the small, unreactive moieties involved in the click chemical linking of probe and target presents a highly effective means of investigating biological interactions[111].

Recent work by Phetsang et al. utilized azide-functionalized drugs as a means of fluorescently tracking antibiotic localization in several species of bacteria[160,161]. Importantly, the authors reported that addition of the azide moiety did not impact antibiotic efficacy, for both a linezolid analogue targeting Gram-positive bacteria and a trimethoprim analogue for Gram-negative studies, emphasizing the potential of azide-functionalized drugs as a powerful tool in elucidating mechanism of action[160,161]. In collaboration with this group, we were able to gain access to a set of azide-functionalized drugs for application in *Msm*. We isolated three of these compounds that showed killing efficacy comparable to that of the native drugs and went on to investigate their applicability in fluorescent labelling. Azide-functionalized vancomycin (1× MIC) and roxithromycin (1× and 2× MIC) were unable to generate a signal exceeding background fluorescence; as they showed effective killing in the growth inhibition assay confirming their ability to penetrate the cell envelope to reach their targets, this result suggested that the intracellular concentration of azide able to bind the fluorophore was insufficient in producing a detectable fluorescent signal. This was highlighted by the lack of fluorescent localization seen for the vancomycin analogue at 2× MIC which, owing to its activity being dependent on binding to peptidoglycan residues, is expected to localize to the cell wall[159]. However, the azide-functionalized linezolid analogue showed some promise, displaying a reasonable amount of fluorescence at 2× MIC. These experiments represent a proof of concept that, with future development of more powerful fluorescent probes, click chemistry might be readily applied as a quick and inexpensive means of conferring drug permeation and localization in mycobacteria.

Conclusion

Mycobacteria are notorious for their uniquely impermeable cell wall that poses innumerable obstacles to effective drug administration[38]. The majority of ongoing research into novel drugs selects a lead compound, usually from a biological source, and uses mathematical and bioinformatic calculations to develop a panel of derived potential drug compounds[162]. We hypothesized that adaptation of the BONCAT protocol as a proxy for drug permeation, in combination with *in silico* permeability prediction, could provide beneficial insight into desirability of candidate molecules. Use of fluorescent dyes with modified side chains and ring structure could prospectively present a quick, inexpensive and simple assay to biochemically elucidate the desirable properties of a candidate molecule. Coupling of calculated molecular properties to predict mycobacterial cell envelope permeation with BONCAT provided a platform

for elucidating how well these predictors represent permeation in empirical investigations. The small set of click-functionalized fluorophores tested allowed us to demonstrate the impact of different moieties on mycobacterial permeation and, combined with the substantial collection of commercially available click chemistries utilizing different reactive groups and coupling mechanisms, provided a basis for future work in applying these side chains to better understand the properties contributing to molecular permeability[113].

The second component of this study aimed to apply BONCAT in mycobacteria to profile the variability of protein activity within apparently homogenous bacillary populations. The population variance observed for single cell BONCAT fluorescence revealed heterogeneity in protein expression that was reduced upon treatment with a protein synthesis inhibitor. These findings provide a foundation for further investigation into how different antibiotics affect heterogeneity in translational activity. Furthermore, elucidating the mechanisms behind this heterogeneity could further clarify the parameters defining persistent and tolerant bacilli. Moreover, it could prove very useful in delineating translational inhibition as part of mechanism of action studies for novel TB drug discovery.

CHAPTER 4: CELL WALL DEFICIENCY IN *MYCOBACTERIUM SMEGMATIS*

Background

L-FORM BACTERIA: A BRIEF HISTORY

Morphologically atypical bacteria were most notably recorded in the 1880s, especially by Ernst B. Almquist working with *Vibrio cholerae*[27]. Similar work was performed in *Mycobacterium tuberculosis* (*Mtb*) by Elie Metchnikoff in 1888 and parallels can be drawn across studies conducted during this period, involving several bacterial species and reflecting strong interest in plotting the so-called life cycle of a bacterium[27,163]. Although cell wall deficient (CWD) forms of bacteria have been noted as far back as 1852, they entered the spotlight when observed and cultured in 1935 by Emmy Klieneberger at the Lister Institute in London. Klieneberger designated these bacteria L1 and L2 (named for the Lister Institute), noting their similarity to the causative agent of pleuropneumonia and identifying them as members of this group of organisms which were later classified as Mycoplasma[26,27,164]. In 1937, Louis Dienes advanced this work by exhibiting a pathogenic capacity of the so called "L-organisms" and their apparent evolution from canonical bacterial parent cells[165]. Although noting their distinct fragility and pleomorphic properties, Dienes was able to culture the L-organisms indefinitely, providing evidence for their independence from the parental bacillus[165]. Soon after, the reversion of L-forms to the parental phenotype was observed, incontrovertibly distinguishing L-forms from Mycoplasma[164]. From that point forward, there was an abundance of literature concerning L-form bacteria, elucidating their chemical composition and understanding their role in disease pathogenesis[29,166–169]. However, research diminished due to the challenges accompanying this avenue of interest, specifically the complexities inherent in L-form isolation and cultivation in conjunction with their obscure and unquantifiable role in pathogenicity. Intriguingly, over the past few years, there has been a resurgence in research into CWD bacteria[170,171]. Revival of the field compels further research in applying past knowledge to modern technology.

CLASSIFICATION OF CELL WALL DEFICIENT FORMS

Scattered throughout the literature are the terms "L-form", "L-phase", "L-variant", "protoplast", "spheroplast" and "cell wall-deficient", presenting much ambiguity in the details that separate one definition from another. L-form bacteria were first noted to be similar to protoplasts in 1957 but deemed distinct in their ability to reproduce[172]. Following this, the initial designation of "L-form" was given to stable variants of bacteria that lacked a cell wall and exhibited Mycoplasma-like colony growth[27]. However,

certain studies still used the word “spheroplast” in defining these cell wall deficient bacteria[173,174]. This abstruse nomenclature can be simplified into four broad categories of cell wall deficiency - namely, stable and unstable forms of both protoplasts and spheroplasts that arise from a parental walled organism (**FIGURE 4.1**). Protoplasts are defined by electron microscopy as devoid of any cell wall structure, whereas spheroplasts retain residual cell wall components; however, both can be considered L-forms if they are capable of replication[175]. Further subdivision into stable and unstable L-forms is determined by their ability to revert to parental cell wall status (unstable) or to replicate indefinitely as L-forms (stable) in the absence of cell wall synthesis inhibitors[175].

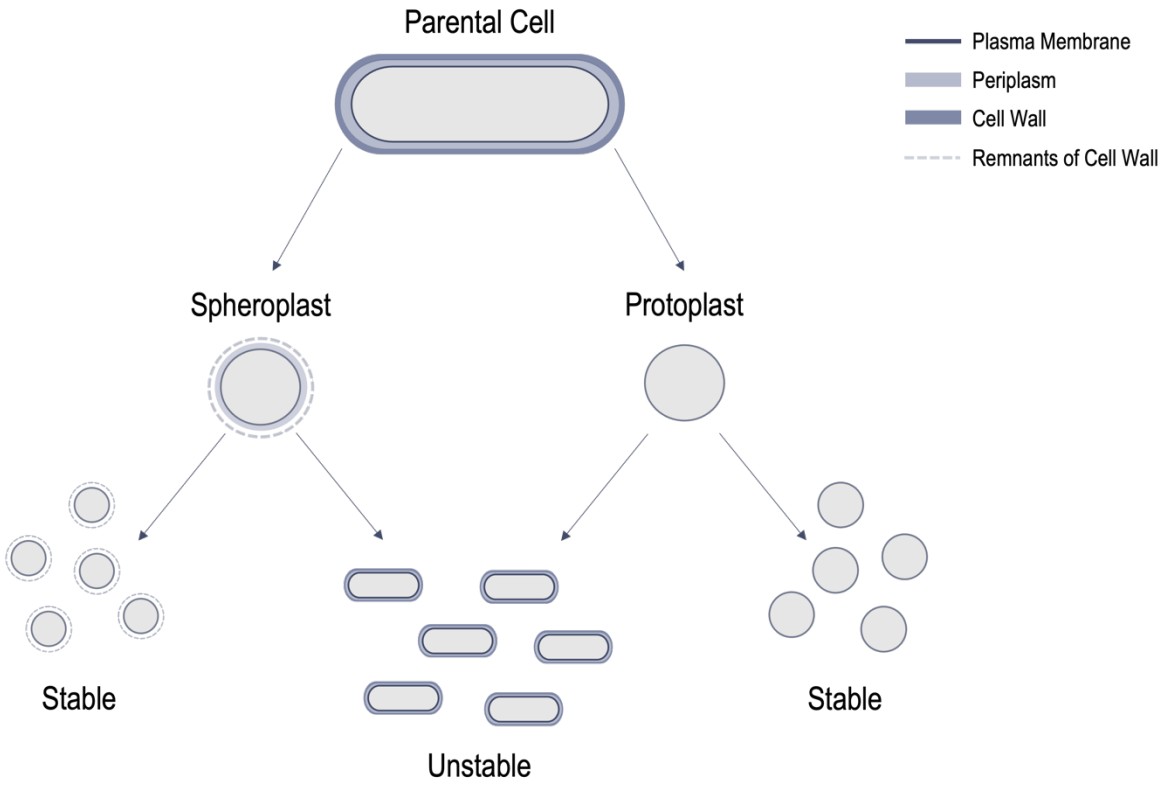

FIGURE 4.1: Categorizing cell wall deficiency. Spheroplasts and protoplasts are considered stable when capable of producing cell wall-deficient progeny and unstable when reverting to wild-type, cell wall replete state.

INDUCTION AND MAINTENANCE OF CELL WALL DEFICIENCY

Initially, L-forms were isolated solely from clinical samples and subjected to penicillin as a means of isolation from cell wall replete organisms[176]. Upon removal of penicillin, reversion to walled bacilli could be observed in broth culture, suggesting these organisms to be unstable L-forms[176,177]. In 1958, Claes Weibull implemented lysozyme treatment in sucrose solution as a means of generating L-forms; this

method was refined over the next decade and is still the most commonly applied protocol today[53,178–180]. The development and survival of L-forms rely on two key criteria; firstly, peptidoglycan synthesis must be inhibited and, secondly, an osmotic stabilizer must be present in the growth medium to prevent lysis. Inhibition of cell wall synthesis can be achieved in various ways: external factors such as lytic enzymes and cell wall inhibiting antibiotics can be utilized; alternatively, genetic manipulation can give rise to mutants that have lost the ability to synthesize cell wall components[155,181]. Maintaining an osmotically stable environment is critical to unstable L-form survival, and this is most commonly achieved by use of a sucrose buffer but can also utilize various salt solutions to the same end[105]. It is possible for stable L-forms to arise through passage in various media or by treatment with mutagenic agents, but this can be a challenging and time-consuming process[175]. Interestingly, successful induction seems more likely to occur under anaerobic as opposed to aerobic conditions[182]. This hypothesis was recently confirmed in *Bacillus subtilis*, in which absence of a cell wall was found to result in increased flux through the glycolytic pathway, increasing the risk of generating reactive oxygen species[183]. L-form functionality and growth could be restored when glycolysis was bypassed, either by depleting oxygen or utilizing the gluconeogenesis pathway[183]. Furthermore, whilst many Gram positive and Gram negative bacteria have been successfully converted into a CWD state, tailored media and methods can be required for certain species whereas others are seemingly impossible to transform[105]. When considering observation of these CWD variants naturally arising in bacterial populations, the aforementioned treatments are not so much 'inducers' of cell wall deficiency but rather selective agents[27].

L-FORMS IN PATHOGENICITY

The clinical relevance of CWD bacteria and their role in disease outcome remains controversial despite being studied for an extensive period. The very first L-forms isolated were from *Streptobacillus monoliformis*, found in the naso-pharynx of rats and now known to cause Rat Bite Fever[26,28]. Following this discovery, L-forms were isolated from a wide range of pathogenic bacteria including *Streptococcus spp*., *Nocardia spp*. and *Mycobacterium spp*[29,166,184,185]. Although it is generally accepted that L-forms can arise within a host as a result of antibiotic treatment or via host immune interactions, it is less clear whether the bacteria have any role in actively causing disease when present in this state[185]. One intriguing avenue of investigation postulates that CWD bacteria are involved in persistence of certain diseases: the lack of a cell wall allows evasion of cell wall targeting antibiotics so that, upon completion of treatment, the bacteria revert back to their native, walled state and are able to cause disease again[78,79,105,185].

Several poorly characterized chronic conditions may be explained by the presence of CWD bacteria, an example being their association with relapse in urinary tract infections (UTI)[79]. In certain cases of chronic renal disease, where no expected species of bacteria can be cultured, the search has been redirected to CWD forms and microscopy has successfully revealed their presence in both urine samples and renal epithelial sections[186,187]. The chronicity of such ailments appears consistent with hypotheses that CWD bacteria can act as persisters, causing relapse of active disease after an indeterminate period of time. L-forms implicated in urinary and renal infections have been found to revert to *Streptococci*, which has also been shown to be the case in rheumatic fever and aphthous stomatitis[188]. It has been suggested that these variants are induced by cell wall targeting antibiotics administered during UTI treatment and can remain viable in the kidneys to later cause recalcitrance of disease[79,189]. The kidneys provide a potentially supportive environment for the survival of CWD organisms given their hypertonicity might promote conversion of wild-type bacteria to a CWD state[190]. Furthermore, it has been shown that altering kidney osmolarity by ingestion of glucose water can result in lysis of CWD forms, clearing infection[191]. The hypertonic nature of the urinary tract and normal acidity of urine are factors that further promote conversion to a CWD state and allow maintenance of bacteria in this form, making it likely that there is constant flux within the system between traditional and aberrant variants of its bacterial inhabitants[27,192,193]. A recent study supporting these hypotheses found L-form *Escherichia coli* present in the urinary tracts of patients suffering from recurrent UTI[79]. Walled bacteria from urine samples were capable of transitioning to an L-form state in the presence of cell wall-targeting antibiotics, and these L-forms retained the ability to revert to wild-type organisms[79]. These findings show the potential implications of L-form switching as a physiologically relevant event in certain disease states[79].

A major confounder to fully understanding CWD pathogenicity lies in the difficulty to culture and identify these atypical organisms, with most clinical culture methods resulting in loss of L-forms owing to their osmotic instability, their low proportion within a bacterial population, and their significantly slower rate of replication[194]. Another complication lies in the lack of modern evidence utilizing advanced methods; the majority of research in this area was carried out before the advent of molecular techniques and comprises primarily of small case studies utilizing variable methods of detection and culture, undermining reproducibility and credibility[185,195]. Notwithstanding these concerns, the weight of historical and – increasingly – modern reports suggests that CWD bacteria should not be disregarded owing to their potential role in persistence. Also, the potential for decreased but not completely absent immunomodulatory properties suggests they might prove useful in eradicating chronic disease, and in aiding vaccine development[195].

MYCOBACTERIAL L-FORMS

Cell wall deficient mycobacteria have been associated with Crohn's disease and sarcoidosis; for example, CWD *Mycobacterium avium subsp. paratuberculosis* (MAP) is a bacterium responsible for Johne's disease in livestock[185,196,197]. Sarcoidosis is a disease with unknown aetiology, resulting in the development of granulomas most commonly in the lungs, lymph nodes, or skin[198]. Several studies have isolated CWD forms of both MAP and *Mtb* from sarcoidosis patients but no direct role of mycobacteria has been demonstrated in the pathogenesis of the disease[194,199–201]. Similarly, while CWD MAP has been found in patients across several studies of Crohn's disease, a disorder characterized by inflammation of the bowel, it is yet to be proven that CWD mycobacteria are the causative agent. Notably, there is no clinical evidence of antimycobacterial treatment having a positive effect on disease outcome[196,202]. Crohn's disease has more recently been attributed to dysbiosis of the gut microbiome caused chiefly by alterations in diet, being labelled as a polymicrobial infection[203]. However, with both sarcoidosis and Crohn's, there is an immune-reactive component that appears to enhance disease symptoms, bearing a striking resemblance to several other chronic infections in which a role for CWD bacteria has been proposed[198,203].

Mtb L-forms were most notably isolated from pulmonary TB patients in 1960 by Lida H. Mattman, a pioneer in the field of mycobacterial L-form research[27,204]. *Mtb* L-forms have subsequently been isolated from TB cases by several groups, hinting at their importance in disease status[194,201]. Artificially generated CWD *Mtb* has been shown to persist within the lungs of guinea pigs for an extensive period of time without causing disease and only exhibiting pathogenic properties upon reversion to the bacillary state[29]. Studies carried out in Russia have found CWD *Mtb* to be the cause of relapse and destructive cavities in patients showing a false negative result for bacillary growth in conventional culture[27,194]. More recent studies have noted the unique properties of CWD *Mtb* formed *in vitro* from clinical strains, including their potential to confer phenotypic resistance to cell wall synthesis inhibitors[77,155,205]. That work highlights the potential importance of L-forms in persistence and recurrence of TB, but also emphasizes the need for more reliable and universally implemented methods of detecting CWD bacteria, including trials with large enough participant cohorts to provide statistical support for the significance of these findings[185].

CELL WALL DEFICIENCY AS A TOOL IN MICROBIOLOGY

The utilization of CWD bacteria to study the enzymes involved in cell wall synthesis is increasingly popular owing to the importance of understanding cell wall biosynthetic pathways in developing effective cell wall targeting antimicrobials. The role of the flippase enzyme, MmpL3, in transporting trehalose

monomycolates to the mycobacterial cell wall was recently elucidated in *Msm* by utilizing CWD bacteria in combination with metabolic labeling techniques[53]. Similarly, Melzer et al. applied CWD *Msm* in conjunction with fusion proteins and metabolic labelling to demonstrate the role of the protein DivIVA in polar envelope assembly[104]. *Vibrio cholerae* spheroplasts have been used to study the Type VI secretion system which plays an important role in the virulence of this organism, again in combination with modern techniques such as fusion proteins and fluorescent time-lapse imaging[206]. These examples highlight the potential for CWD bacteria as important research tool.

Several studies have utilized β-lactams to demonstrate the capacity for cell wall deficiency as a bacterial survival strategy. The long-standing method of confirming L-form morphology was via electron microscopy (EM), which defined protoplasts as possessing a cell membrane only and spheroplasts as retaining some cell wall remnants[175]. More recently, with the use of molecular techniques and advances in widefield microscopy, limited peptidoglycan synthesis has been confirmed as essential for survival and propagation of Gram negative L-forms[207]. However, this almost negligible peptidoglycan biosynthetic activity seems to be unaffected by cell wall-targeting enzymes. For example, *Bacillus subtilis* is capable of generating and propagating L-forms under lytic conditions such as those experienced in the host macrophage to avoid cell death[155]. Similarly, L-forms have been shown to play an important role in phenotypic resistance of *Mtb* to the frontline drug, ethambutol[77]. The target of ethambutol is an enzyme responsible for the polymerization of arabinose monomers which make up a portion of the mycomembrane; by sloughing its cell wall, the mycobacterial L-form renders the drug ineffective[77]. Other work has shown that heat stress in *E. coli* and nutrient starvation in *Mtb* can lead to the formation of CWD bacteria as a mechanism of survival[205,208]. Combined, these studies strongly suggest that cell wall deficiency may play a central role in bacterial persistence under stress conditions.

A major driver behind the use of CWD bacteria in biotechnology is their increased permeability in comparison to their walled counterparts. They were initially used as expression systems because transformation of plasmid DNA proved easier without the obstacle of a fully intact cell wall and protein yields were found to be comparable to those of conventional expression systems[105,209]. The absence of a cell wall proved beneficial in a multifactorial manner; amongst others, the protein product of the plasmid no longer became trapped within the periplasm and was not exposed to extracellular proteases[210]. A more recent paper proposed the utilization of L-forms with the intent of creating a simple system for the synthetic design of therapeutic phages[103]. In their study, Kilcher et al. subjected Listeria L-forms to both native and synthetic phage genomes in an attempt to develop a robust system for the rebooting of phage

DNA for propagation of viable phages[103]. This study provides an excellent example of the potential applications of CWD bacteria in the fields of synthetic biology.

Results

GENERATION OF CELL WALL DEFICIENT *MYCOBACTERIUM SMEGMATIS*

Previous investigations into the development of CWD bacteria have implemented various strategies to chemically strip the cell wall. In this study, we adopted a protocol in which *Msm* was grown in medium containing 1.2% glycine to initiate the process of spheroplasting, with addition of lysozyme in an osmotically stable medium causing further degradation of cell wall components. Successful generation of CWD *Msm* organisms was determined using phase contrast and fluorescence microscopy (**FIGURE 4.2A**). An *Msm parB*::mCherry bioreporter mutant[107] was used as the experimental strain to ensure the maintenance of the same species throughout the spheroplasting process based on the expression (and detection) of the endogenous fluorophore. This was validated using fluorescence microscopy and PCR amplification of the mCherry gene (**FIGURE 4.2A&B**).

The essentiality of an osmoprotective environment was investigated by placing CWD organisms in standard 7H9 medium. This resulted in both cell lysis, expected due to the fragility of CWD bacteria, and apparent reversion to a walled state (**FIGURE 4.2C**). In the presence of only a semi-permeable cytoplasmic membrane, bacteria become extremely sensitive to changes on osmolarity, whereas cell wall replete organisms can withstand such environmental changes and maintain osmotic pressure. Therefore, the results indicated that some *Msm* spheroplasts were unable to cope with the changes in osmotic pressure and underwent lysis, whereas others appeared to regenerate cell wall components in response to the environmental changes experienced.

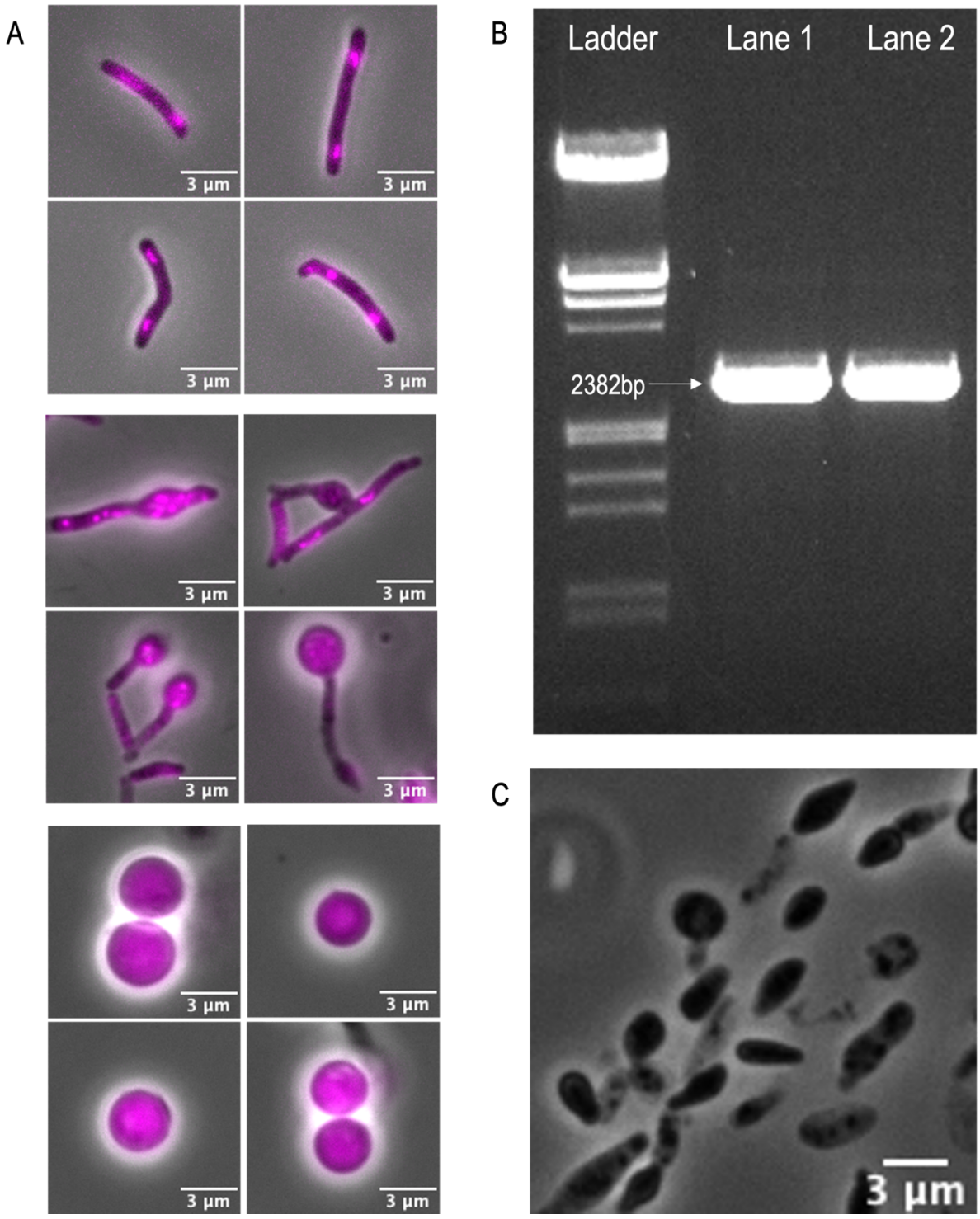

FIGURE 4.2: Lysozyme treatment degrades cell wall components. (A) Microscopic validation of *Msm parB*::mCherry when cell wall replete (top), during initial stages of spheroplasting in the presence of 1.2% glycine (middle), and following complete loss of cell wall components after lysozyme treatment (bottom). (B) PCR validation of species maintenance throughout the treatment by continued presence of the *Msm metH* gene (Lane 1, cell wall replete; Lane 2, lysozyme treated). Molecular Weight Marker III (Roche Diagnostics) was used to estimate PCR product size (2382bp). (C) Morphological changes observed in spheroplasts following transfer to standard Middlebrook 7H9 medium. All image analysis was carried out in ImageJ.

TIME-LAPSE MICROSCOPY OF SPHEROPLAST FORMATION

To fully understand the steps involved in spheroplast formation, time-lapse microscopy was used to monitor cell wall degradation over time (**FIGURE 4.3)**. Treatment was initiated in culture with the addition of 1.2% glycine for 16h before loading the bacteria in a CellASIC® ONIX2 bacterial plate and perfusing 1.2% glycine and lysozyme into the viewing chamber for time-lapse microscopy. Within 3h of exposure to lysozyme, the cells began to undergo minor morphological changes; by 7h, fully formed spheroplasts were observed. The intensity of the phase contrast decreased as the cells underwent morphological changes, implying the loss of cell wall components. Furthermore, once spheroplast formation had taken place, a 'shell' was often visible which suggested the spheroplasting process separated the surviving structure from the cell wall (**FIGURE 4.3, bottom panel**).

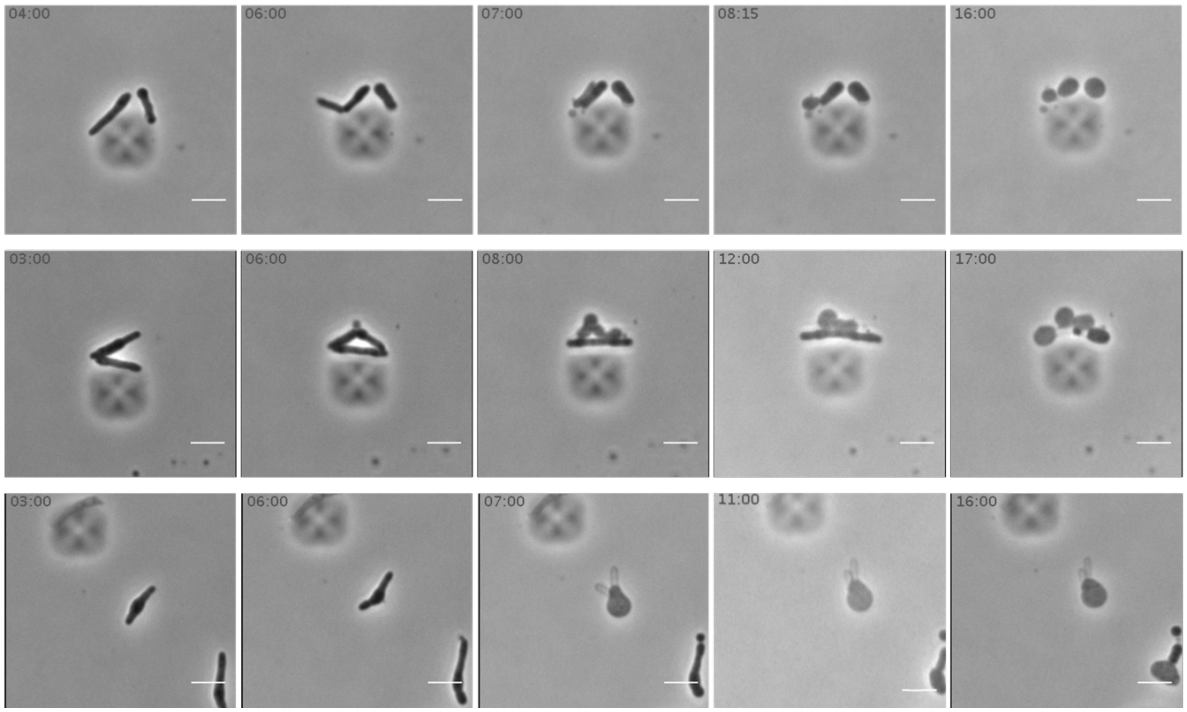

FIGURE 4.3: Time-lapse microscopy reveals formation of cell wall deficient *Msm*. An osmoprotective medium containing 1.2% glycine and lysozyme was perfused across wild-type *Msm* for 18h to visualize morphological changes experienced by bacteria in response to chemical treatment to degrade cell wall components. Time-lapse microscopy was carried out using a CellASIC® ONIX2 microfluidic device and Zeiss Axio Observer inverted microscope. Image analysis was done in ImageJ. Scale bars represent 3μm.

INVESTIGATING LOSS OF CELL WALL COMPONENTS

Staining the Mycolic Acid Layer

To investigate the changes in cell wall structure resulting from lysozyme treatment of *Msm*, we began by analyzing mycomembrane composition utilizing DMN-trehalose. This fluorescent trehalose analogue is incorporated into trehalose monomycolates, the building blocks of the mycomembrane, where it experiences a substantial increase in fluorescence in the hydrophobic environment of the cell wall, allowing for visualization under the microscope[211].

Both wild-type *Msm* and derivative spheroplasts were exposed to DMN-tre for 20min at 37°C before fluorescence quantification. When comparing the distribution of fluorescent signal across the medial axis of individual cells, we quickly noted that cell wall replete bacilli exhibited stronger fluorescence than spheroplasts (**FIGURE 4.4A&B**). There was a distinct localization pattern in wild-type organisms in which fluorescence was concentrated at the poles, an effect readily discernible in the representative images (**FIGURE 4.4D**) and in agreement with previous research into the polar growth dynamics of mycobacteria[58]. It was also clear that, with increasing cell length, we more frequently saw a fluorescent focus appearing towards the centre of individual rods, representing the accumulation of cell wall material at the site of septum formation for division[58]. In stark contrast, spheroplasts exhibited very low levels of fluorescence with no apparent localization, strongly suggesting that mycolic acid biosynthesis had not taken place. We observed low-level, mid-cell fluorescence in spheroplasts that increased with cell length, perhaps implying a slow accumulation of cell wall constituents required to reconstruct the mycolic acid layer. Comparison of whole-cell fluorescence between samples showed a significant decrease in spheroplasts, reiterating our interpretation that these organisms were not actively synthesizing mycomembrane components (**FIGURE 4.4C**).

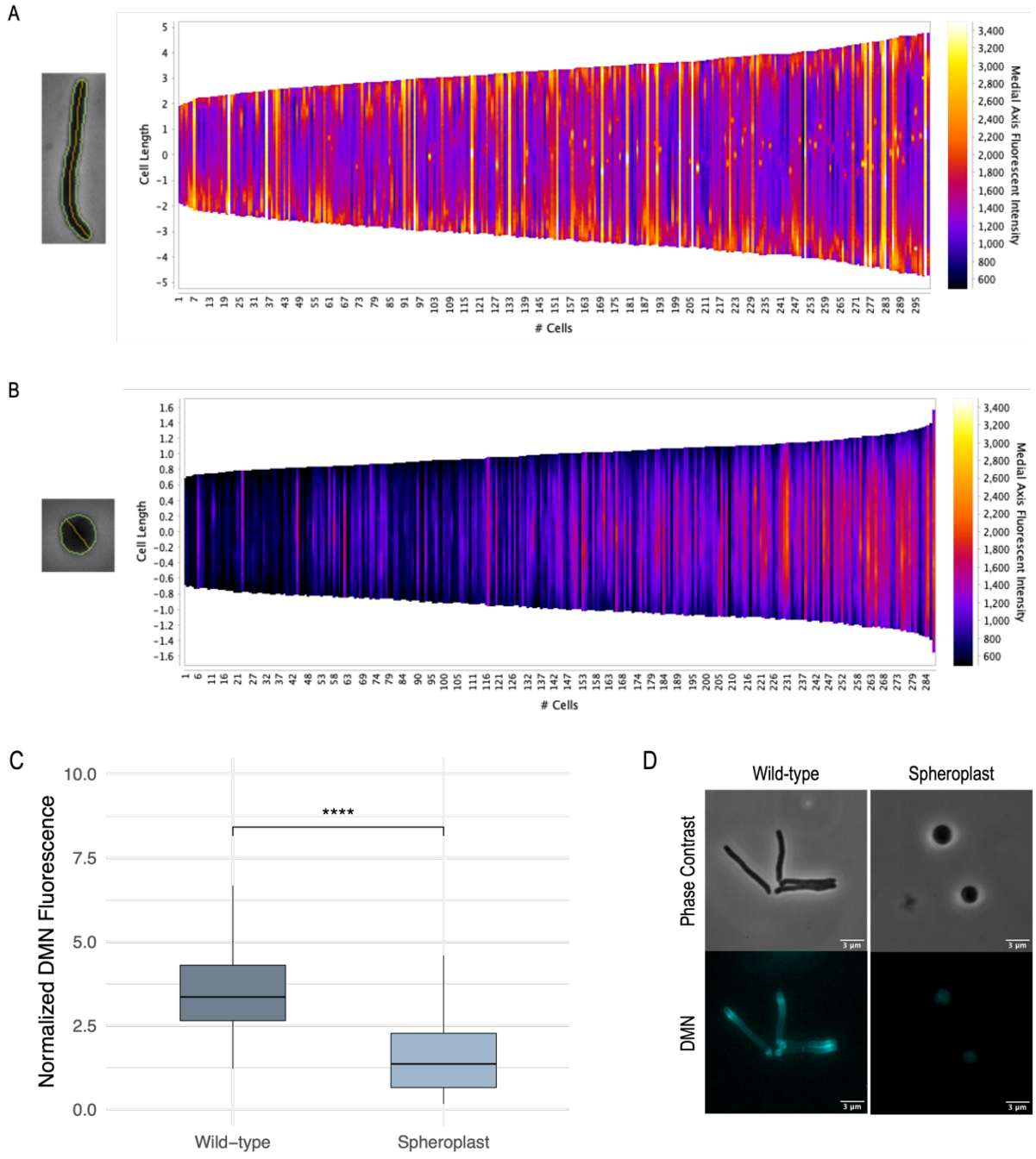

FIGURE 4.4: Decreased incorporation of mycomembrane stain in spheroplasts. Demographs displaying single-cell medial axis profiling of DMN-tre fluorescence in wild-type (A) and spheroplast (B) *Msm*. Whole-cell fluorescence was quantified for each cell type (C) and representative fluorescent images of each sample were generated (D). Fluorescence was visualized using a Zeiss Axio Observer and quantified in ImageJ. For each condition, 100 cells were measured in triplicate and Student's t-test was performed to determine significance, p=0.005.

Peptidoglycan Staining

The peptidoglycan layer is considered essential for bacterial survival in almost all environments[212]; it was important, therefore, for us to investigate the potential (and extent of) loss of this structure in spheroplasts. To this end, we utilized the metabolic probe, N-acetyl-D-alanine (NADA), a fluorescent D-alanine analogue that is metabolically incorporated into the peptidoglycan layer during active synthesis[213]. As before, both *Msm* morphotypes – wildtype and spheroplasts – were incubated with NADA for 20min at 37°C before visualization. Medial axis profiling revealed a strong fluorescent signal in cell wall replete bacilli that exhibited similar polar localization patterns to those seen with DMN-tre (**FIGURE 4.5A&D**). However, fluorescence was also observed across the midsection of wild-type cells, agreeing with other findings that peptidoglycan synthesis occurs not only at the poles but also along the sidewalls of mycobacterial species[214]. NADA staining of spheroplasts differed markedly from that seen in wild-type (**FIGURE 4.5B**), exhibiting near-complete absence of fluorescence and no localization patterns; this suggested little to no peptidoglycan synthesis. Analysis of whole-cell fluorescence revealed significantly decreased probe incorporation in the cell wall deficient variant, in concordance with medial axis profiling and mycomembrane staining data. These results further supported the hypothesis that, given an osmoprotective environment, these variants are capable of surviving in the absence of cell envelope components that are conventionally considered essential to most bacteria.

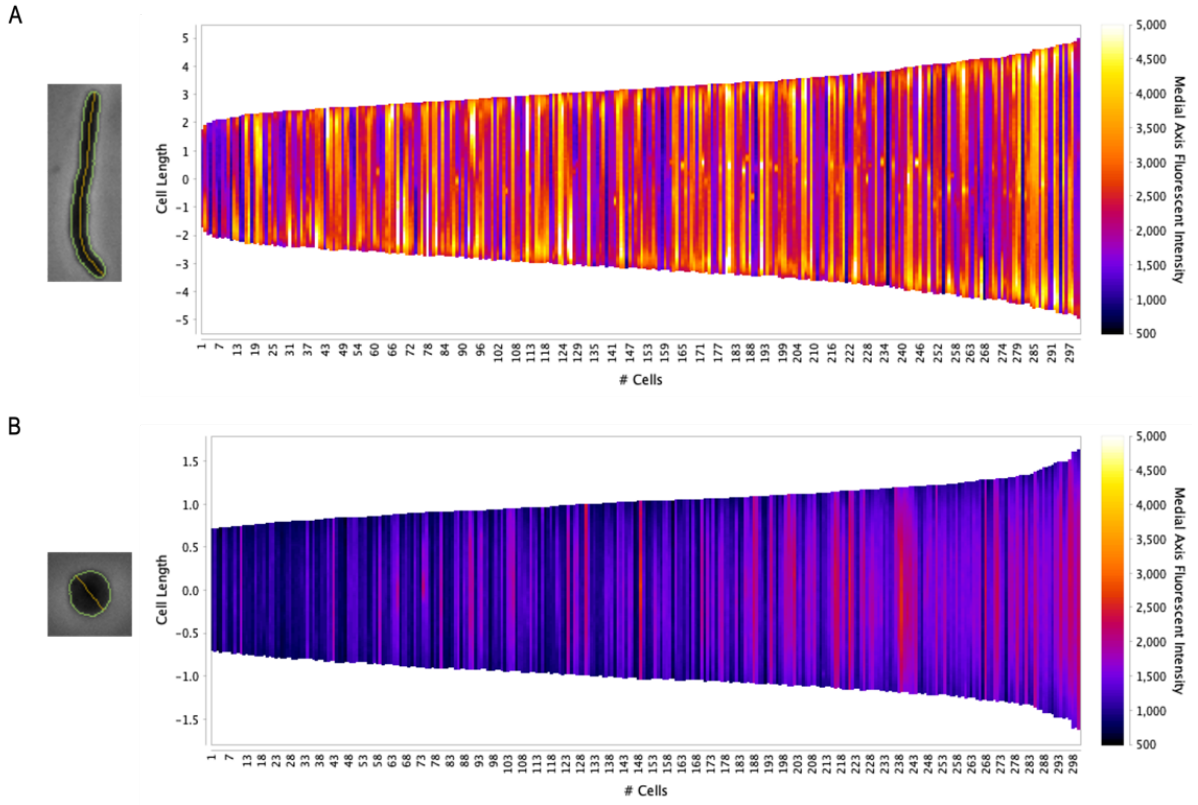

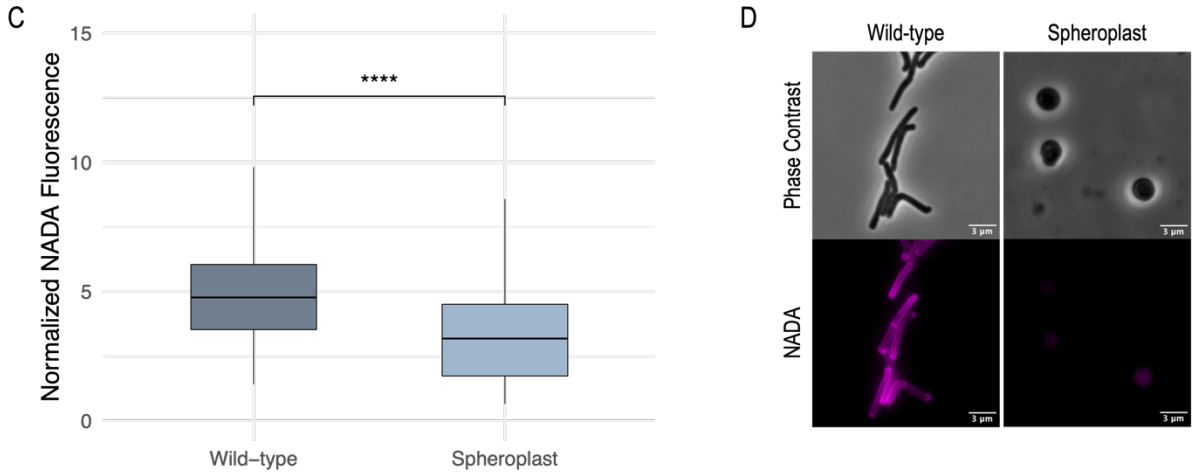

FIGURE 4.5: Peptidoglycan staining is reduced in spheroplasts. Demographs displaying single-cell medial axis profiling of NADA fluorescence in wild-type (A) and spheroplast (B) *Msm*. Whole-cell fluorescence was quantified for each cell type (C) and representative fluorescent images of each sample were generated (D). Fluorescence was visualized using a Zeiss Axio Observer and quantified in ImageJ. For each condition, 100 cells were measured in triplicate and Student's t-test was performed to determine significance, p=0.005.

Plasma Membrane Staining

The lipophilic styryl dye, FM™4-64, was used to investigate the changes in plasma membrane composition between wild-type cells and derivative spheroplasts. FM™4-64 is highly lipophilic, requiring very short incubation times in mammalian cells to prevent endocytosis and ensure labelling of only the plasma membrane. As this dye has very broad specificity, it was predicted that lipid-based components of the mycomembrane such as the free lipids and various mycolates found in this layer of the cell wall would incorporate the stain along with the lipid components of the plasma membrane. As a result, the cell wall replete wild-type bacteria were expected to incorporate higher levels of FM™4-64 than their cell wall deficient counterparts.

Wild-type and spheroplast *Msm* were stained with FM™4-64 and fluorescence was quantified to inspect variations in labelling efficiency. Interestingly, the CWD bacteria showed significantly lower staining capacity when compared to wild-type (**FIGURE 4.6A**). This finding substantiated our hypothesis that lysozyme treatment removes most cell wall components, leaving behind the plasma membrane as the only layer encasing the organisms.

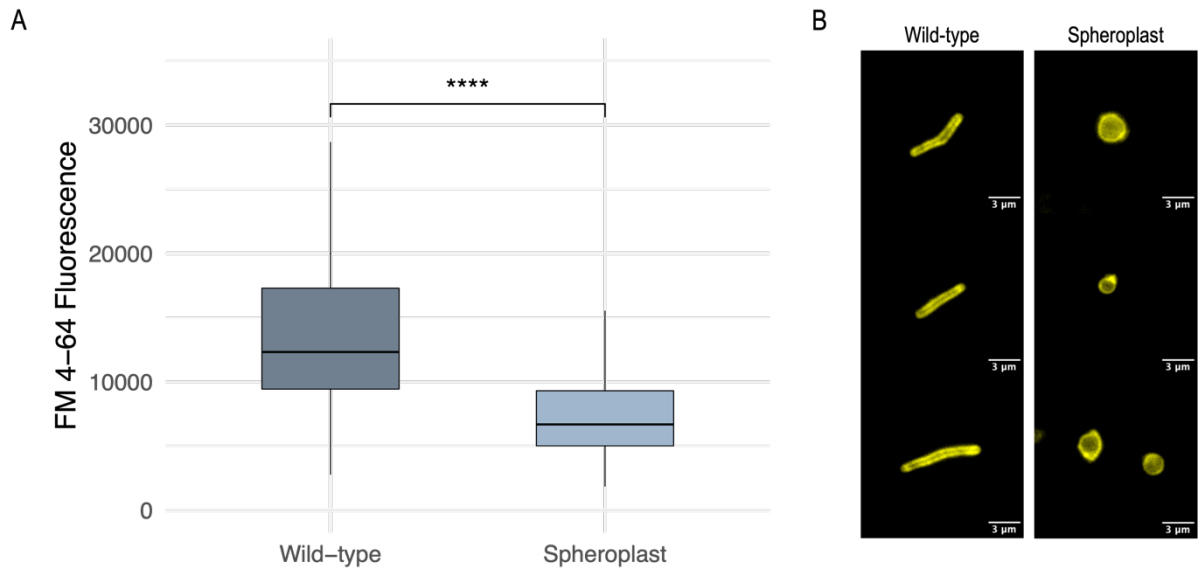

FIGURE 4.6. Spheroplasts exhibit plasma membrane staining. (A) Whole-cell fluorescence of wild-type and spheroplast *Msm*. (B) Representative images of wild-type and spheroplast bacteria stained with FM™4-64. Fluorescence was visualized using a Zeiss Axio Observer and quantified in ImageJ. For each condition, 100 cells were measured in triplicate and Student's t- test was used to determine significance, p=0.005.

ARE CWD BACTERIA CAPABLE OF PROLIFERATING?

Studies in *Bacillus subtilis* have tracked the potential for CWD bacteria to undergo replication, revealing a primitive mechanism by which excess membrane synthesis drives fission[215]. The potential that mycobacteria might be capable of replication in the absence of a cell wall was intriguing, and suitable for investigation in *Msm* using time-lapse microscopy (**FIGURE 4.7**). Image analysis revealed patterns similar to those seen in studies conducted in *B. subtilis*, with cells displaying a blebbing mechanism consistent with an attempt to generate an excess of membrane components. This is thought to cause a shift in the surface area to volume (A/V) ratio of the organism that drives fission into daughter cells in order to restore the ratio to within normal limits. The top two panels display instances of cellular expansion that alter the A/V ratio and the bottom two panels show tubulation and blebbing processes that allow for the budding of daughter cells (**FIGURE 4.7**). These finding suggested that, once bacteria had been stripped of their cell wall, they did not simply persist in an inactive state but were potentially capable of replicating.

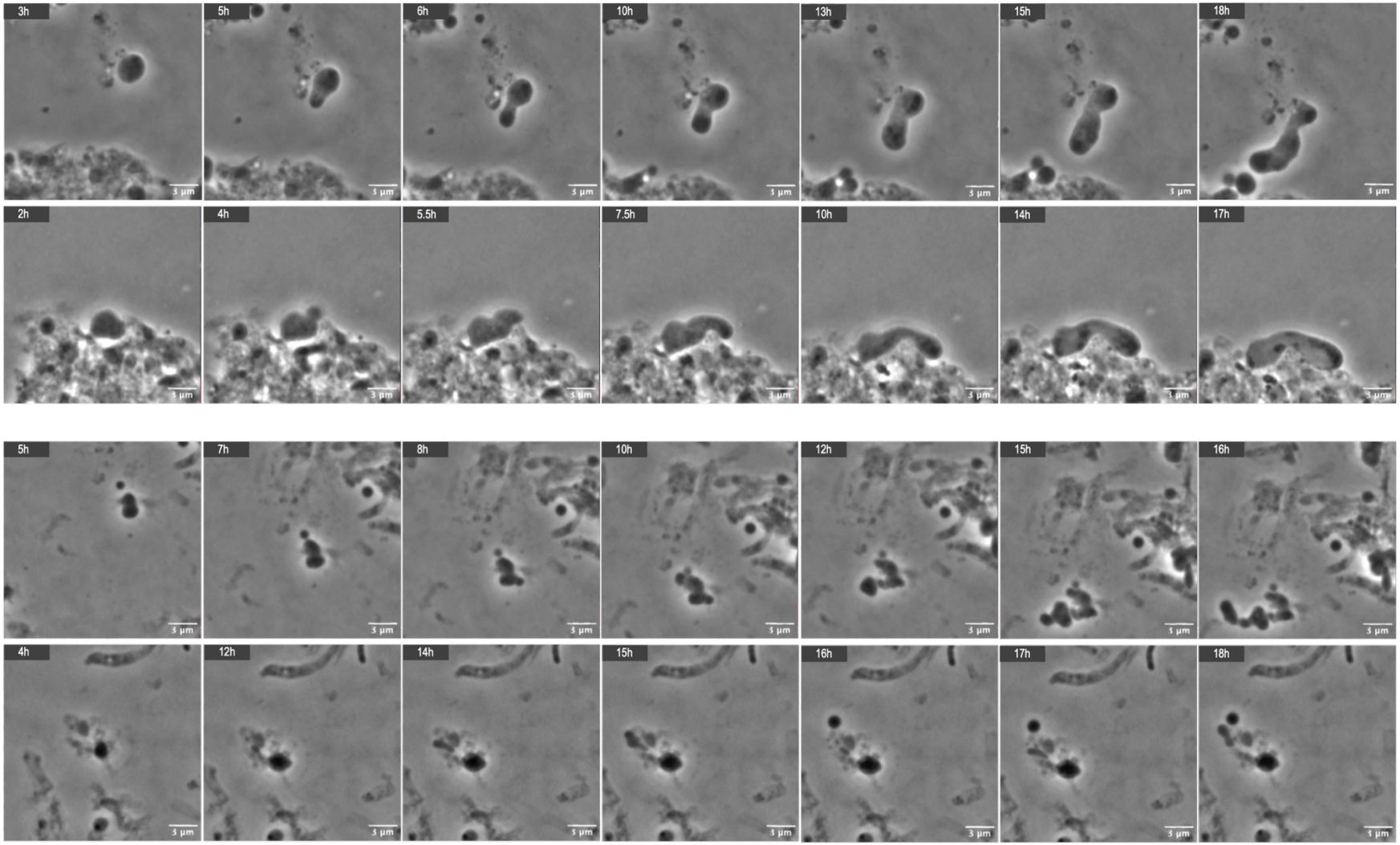

FIGURE 4.7. Excess membrane synthesis in spheroplasts. Excess membrane synthesis in spheroplasts can be seen in the top two panels. The bottom two panels show blebbing and tubulation to produce progeny. Time-lapse microscopy was carried out using a GeneFrame® placed on the incubated stage of a Zeiss Axio Observer inverted microscope. Image analysis was done in ImageJ. Scale bars represent 3μm.

The ParB protein is involved in chromosome partitioning during cell division. Following DNA replication, ParB binds near the origin of replication (*oriM*) and pulls chromosomes towards the poles in preparation for cell division[107]. We sought to utilize this protein to investigate alterations in nucleic acid localization in spheroplasts using a chromosomal *parB*::*mCherry* translational fusion[107]. Fluorescence microscopy was used to visualize localization of the ParB protein and fluorescent maxima were counted.

Spheroplasts displayed a decrease in number of ParB::mCherry foci when compared to wild-type, cell wall-replete *Msm* (**FIGURE 4.8A&B**). Wild-type cells exhibited between 1 and 5 foci, with ~50% of the cells analyzed (149/300 cells) containing 2 foci. This observation was in accordance with the role of the ParB protein in partitioning newly replicated chromosomes in preparation for cell division[107]. In contrast, the majority of spheroplasts displayed only a single focus (237/300 cells) suggesting diffusion of the ParB protein throughout the cytoplasm. It is tempting to suggest these findings are consistent with previous reports of a FtsZ-independent mode of proliferation in CWD organisms[215]. Nearly all bacteria require FtsZ to develop a Z-ring at the site of cell division; in rod-shaped bacteria, this process is closely coupled with polar signals that allow for the correct partitioning of chromosomes and cytoplasmic components in preparation for division[215]. The structural and morphological changes required to generate spheroplasts may have resulted in loss of polar signaling as cells transitioned from a rod to sphere shape. ParB therefore appears to have lost its role in chromosome partitioning in spheroplasts due to the absence of polar signaling, resulting in the diffuse signal seen in **FIGURE 4.8B**.

These findings were validated using Syto™9. This cell membrane permeating nucleic acid stain displays enhanced fluorescence when bound to DNA or RNA. Although this fluorophore is capable of staining RNA as well as DNA, it can be used as an indicator of chromosome number within a cell due to the fluorescent foci that develop when a chromosome is in its condensed state. As such, this assay aimed to confirm the internal fluorescence properties exhibited by ParB::mCherry in wild-type and spheroplast *Msm*. Fluorescence microscopy was utilized to visualize and quantify the staining intensities and localizations of Syto™9 in both wild-type and spheroplast bacteria.

Evaluation of Syto™9 fluorescent maxima showed concordance with *parB*::mCherry data: whereas wild-type cells showed a wide distribution of maxima (between 0-8 per cell), spheroplasts largely contained a single maximum (209/300 cells) (**FIGURE 4.8C**). Again, the single focus detected in spheroplasts appeared to be due to the presence of diffuse signal throughout the cell, whereas cell wall replete bacilli showed distinct fluorescent foci (**FIGURE 4.8D**). These findings indicated that wild-type cells were actively undergoing DNA condensation in preparation for cell division, whereby spheroplasts were likely unable to carry out this process. This could be due to reduced metabolic rate and/or, as previously observed in

our time-lapse experiments, possible unconventional methods of replication in CWD bacteria that do not conform to the typical route of chromosomal condensation and segregation generally observed in bacteria preparing for cell division[216].

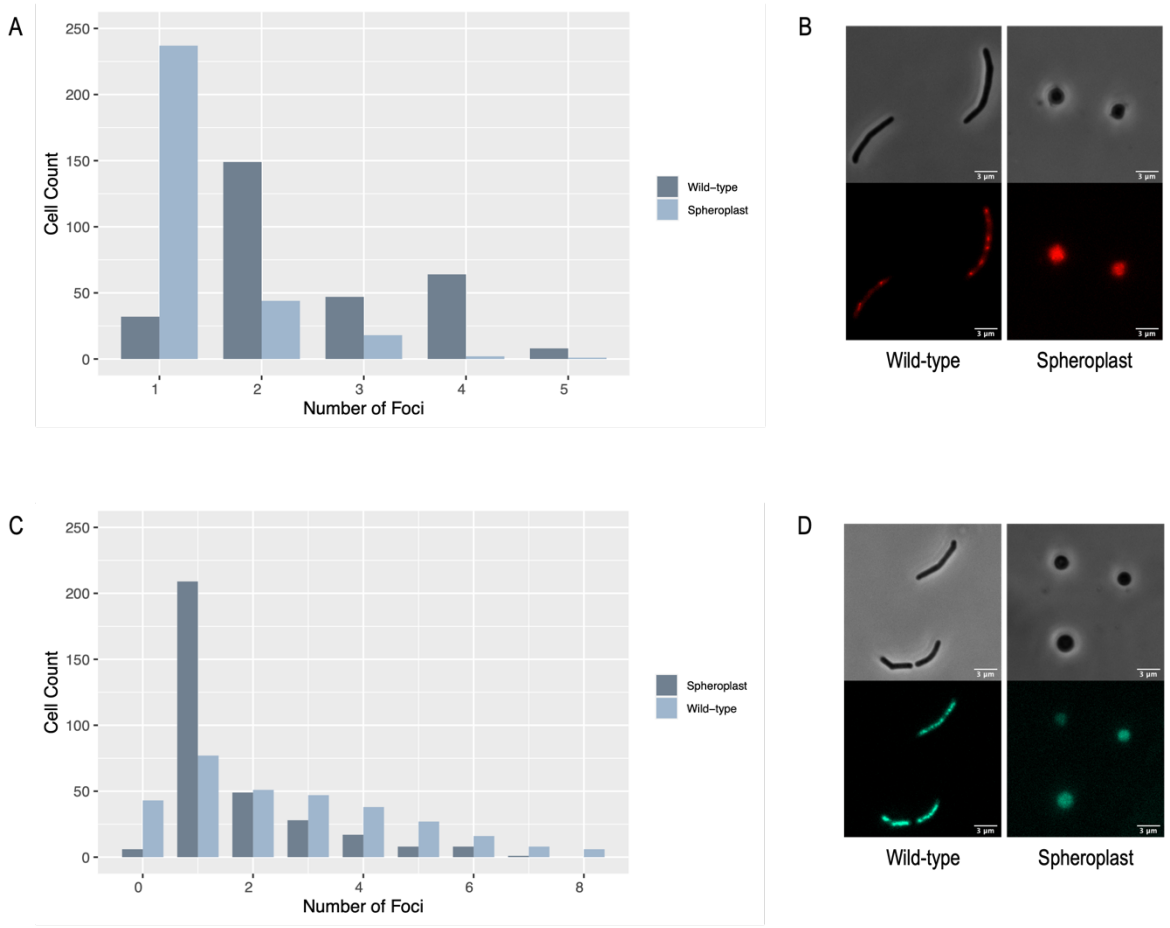

FIGURE 4.8: Spheroplasts show loss of chromosome localization. The number of fluorescent maxima were counted for wild-type and spheroplast *Msm* for the endogenous *parB*::*mCherry* tag and the exogenous Syto™9 nucleic acid stain (C) and representative images of ParB::mCherry fluorescence (B) and Syto™9 fluorescence (D) can be seen for each variant. Fluorescence was visualized using a Zeiss Axio Observer and quantified in ImageJ. For each condition, 100 cells were measured in triplicate.

OXIDATIVE STRESS IN SPHEROPLASTS

Oxygen is the terminal electron acceptor of energy production in all aerobic organisms[170]. However, reactive oxygen species (ROS) can be produced as byproducts of this pathway, causing damage to essential metabolites within the cell and resulting in oxidative stress[170,217]. It has previously been shown in *B. subtilis* that oxidative stress is a major factor affecting the viability of CWD bacteria[170]. To investigate whether this holds true in mycobacteria, the fatty acid analogue, BODIPY™ 581/591 C11, a probe of lipid peroxidation, was used to assess the level of oxidative stress experienced by spheroplast *Msm*. BODIPY™ 581/591 C11 is incorporated into all lipids, fluorescing red under normal conditions but

undergoing a shift to green fluorescence upon oxidation by free radicals[170]. Fluorescence microscopy was utilized to visualize BODIPY™ 581/591 C11 fluorescence and quantify the level of lipid peroxidation experienced by wild-type and spheroplast *Msm*. This was achieved by normalizing the fluorescence resulting from lipid peroxidation (green) to that of total lipid content (red).

As a proxy for oxidative stress, wild-type *Msm* was treated with H_2O_2 which reacts with Fe^{2+} ions to produce •OH radicals[218]. Wild-type bacteria treated with H_2O_2 showed significantly higher levels of oxidative stress compared to untreated cells, providing a positive control for the efficacy of the probe in detecting increased levels of free radicals. The lipid peroxidation of H_2O_2-treated wild-type bacteria resembled that experienced by spheroplasts but was significantly lower. This large increase in oxidative stress experienced by spheroplasts was suggestive of a metabolic imbalance elicited by the removal of the cell wall (**FIGURE 4.9A**). Representative images clearly show the elevated levels of peroxidation-associated fluorescence for H_2O_2-treated and untreated spheroplast variants (**FIGURE 4.9B**). These results correspond with those reported in previous *B. subtilis* studies, suggesting that elevated oxidative stress is experienced when *Msm* is stripped of its cell wall components[170].

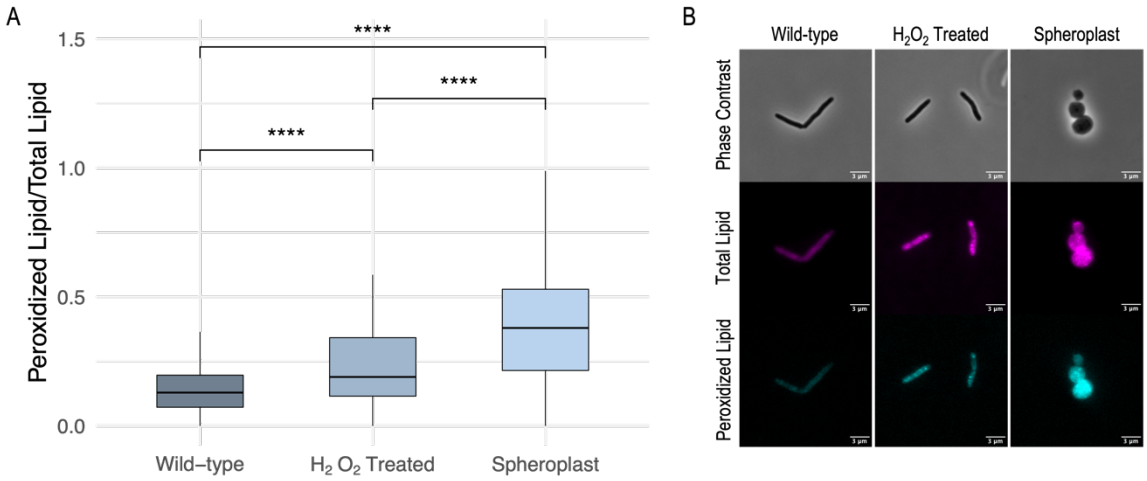

FIGURE 4.9. Cell wall deficiency results in increased lipid peroxidation. BODIPY™ 581/591 C11 fluorescence was used as a proxy for oxidative stress, with peroxidized lipid normalized against total lipid content. (A) Normalized fluorescence in spheroplasts compared to wild-type and H_2O_2-treated *Msm.* (B) Representative images of C_{11}-BODIPY$^{581/591}$ staining (magenta indicates total lipid content, cyan indicates peroxidized lipid). Cyan fluorescence was normalized against unstained cells before fluorescence analysis to account for autofluorescence in this channel. Fluorescence was visualized using a Zeiss Axio Observer and quantified in ImageJ. For each condition, 100 cells were measured in triplicate and a pairwise comparison was used to determine significance, p=0.005.

PROTEOMIC PROFILING OF THE CELL ENVELOPE

We next set out to validate our microscopic findings by implementing a fractional proteomic analysis adapted from Hermann et al[219]. Their protocol is based on centrifugation of protein digests at varying speeds to allow for the separation of cytoplasmic from cell envelope and cell debris fractions. Applying this method, in which each fraction was subjected to label-free LC-MS/MS, yielded a total of ~2800 proteins across all samples. After filtering for common contaminants and reverse hits, proteins with q-value < 0.01 and two or more unique peptides were used for downstream analysis. Only proteins present in all three replicates for each fraction were included (**TABLE 4.1**). Owing to the lipid rich nature of the cell envelope, these fractions yielded the lowest amount of protein, whereas the debris fractions contained the most proteins given that it comprised all insoluble molecules.

TABLE 4.1. Proteins present in all three biological replicates of wild-type and spheroplast samples for each fraction and those that were significantly associated with a functional category from either the Gene Ontology or KEGG databases

	Cell Envelope Proteins	Cytoplasmic Proteins	Cell Debris Proteins
	Present in All 3 Replicates		
Wild-type	325	657	844
Spheroplast	244	557	811
	Functionally Annotated		
Wild-type	167	407	507
Spheroplast	132	344	451

Functional annotation of proteins present in each fraction was carried out using the ClueGO application within Cytoscape[220,221]. Ontologies and pathways recognized in *Mycobacterium smegmatis* str. mc²155 were assembled from GO Molecular Function, GO Biological Process, GO Cellular Component and KEGG to assign function to the identified proteins in each fraction. Only proteins that showed significant association with each pathway were included in the analysis; this allowed us to generate functional networks representing the number of identified proteins associated to a particular pathway (represented by node size) and the level of significance with which these proteins were linked to each category (represented by node colour).

We initially looked at functional annotation for all proteins present in all three replicates for each fraction for both wild-type and spheroplasts (**FIGURE 4.10**). Analysis of the cytoplasmic fractions revealed little difference between each condition (**FIGURE 4.10 E & F**). The cell envelope fractions showed a high level of contamination with known and predicted cytoplasmic proteins; however, the wild-type samples

included 33 proteins associated with ABC transporter activity and 10 proteins associated with protein export (FIGURE 4.10A) – functional categories that were absent in the spheroplast cell envelope fraction (FIGURE 4.10B). Similarly, the wild-type debris fraction contained proteins linked to ABC transporter activity, protein export, and membrane components (FIGURE 4.10C). Interestingly, the spheroplast cell debris samples also showed association with membrane components and protein export (FIGURE 4.10D) which suggested these proteins may be closely linked to the plasma membrane and not the cell wall, resulting in their ability to remain intact during the spheroplasting process. Only 77 proteins in the spheroplast samples were found to be integral to the membrane, whereas the cell wall replete fraction showed 179 protein associations (Supplementary Information 2), strongly suggesting loss of a large proportion of components associated with the membrane. Together, these results implied an extensive decrease in cell envelope-associated proteins in spheroplasts, supporting previous experimental findings that lysozyme treatment causes degradation of the outer layers of the mycobacterial envelope.

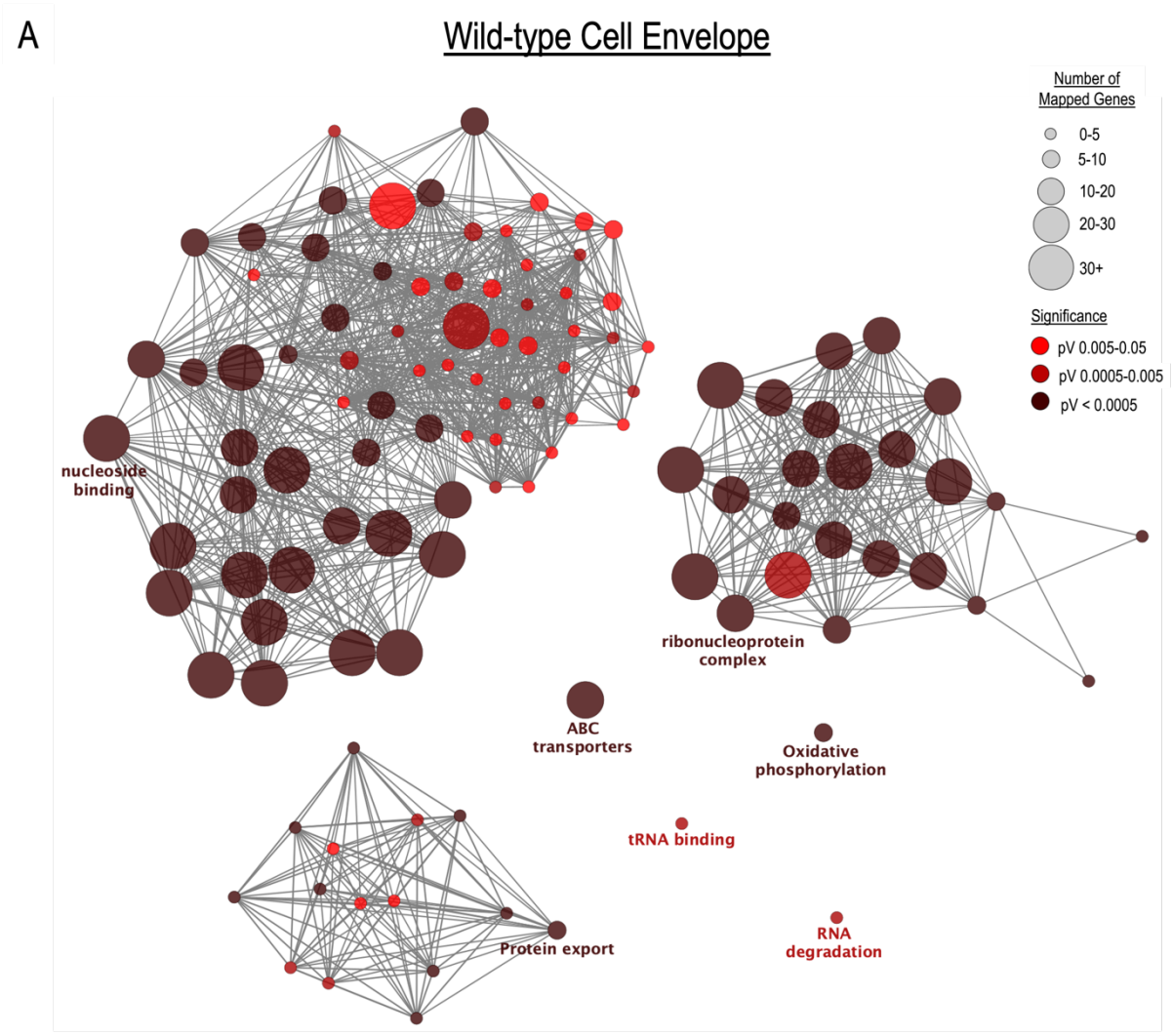

B

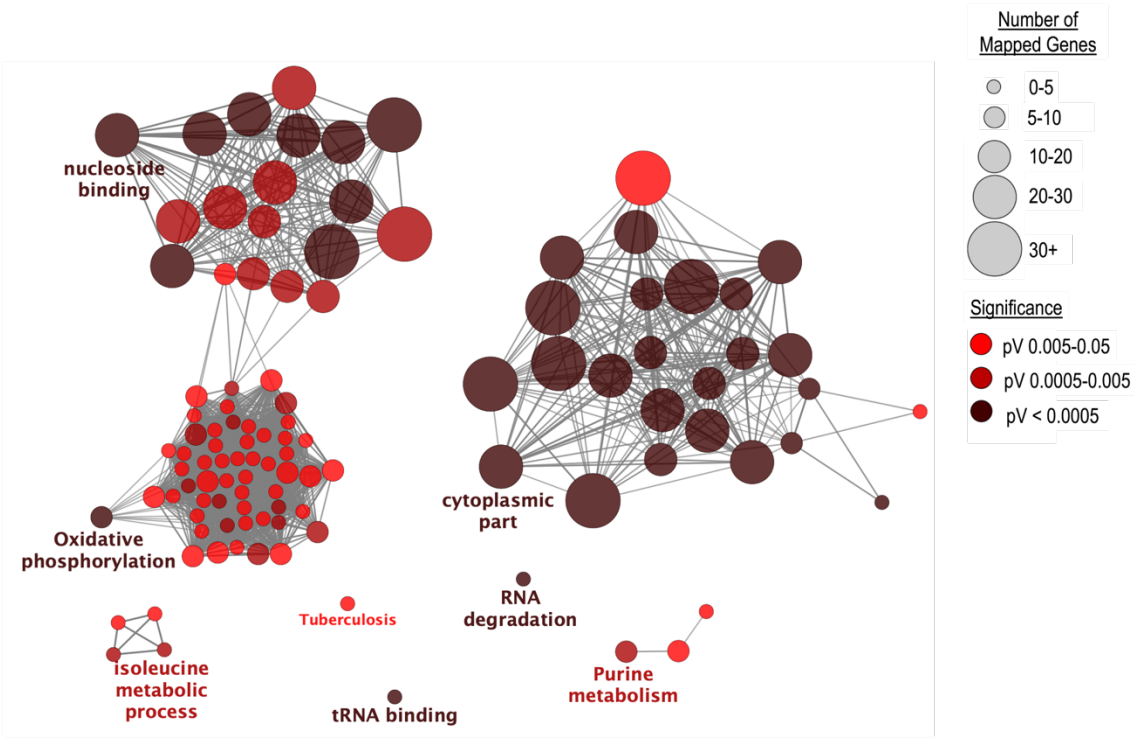
Spheroplast Cell Envelope
Number of Mapped Genes
0-5
5-10
10-20
20-30
30+
Significance
pV 0.005-0.05
pV 0.0005-0.005
pV < 0.0005
nucleoside binding
Oxidative phosphorylation
cytoplasmic part
Tuberculosis
RNA degradation
isoleucine metabolic process
tRNA binding
Purine metabolism

C

Wild-type Debris

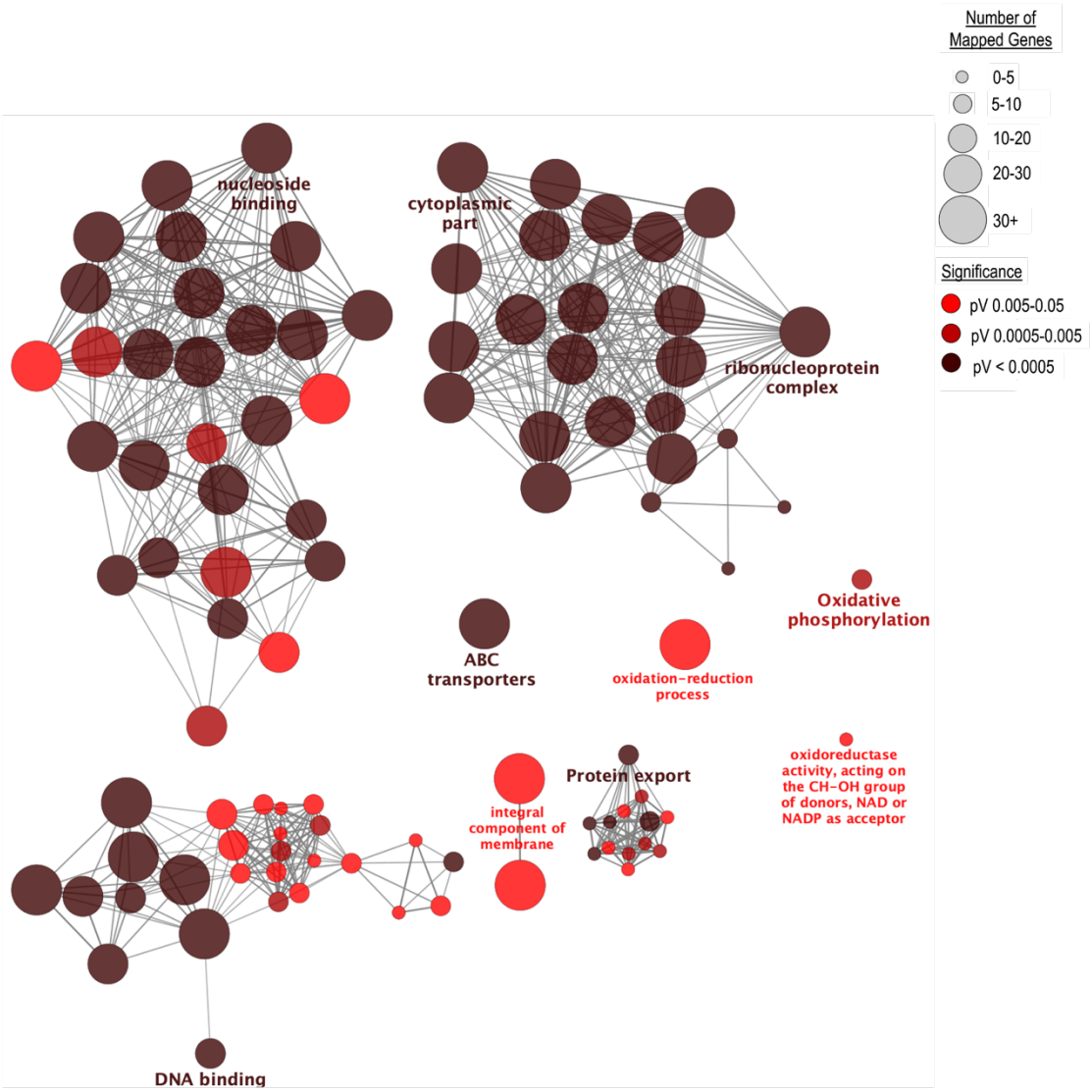

D

Spheroplast Debris

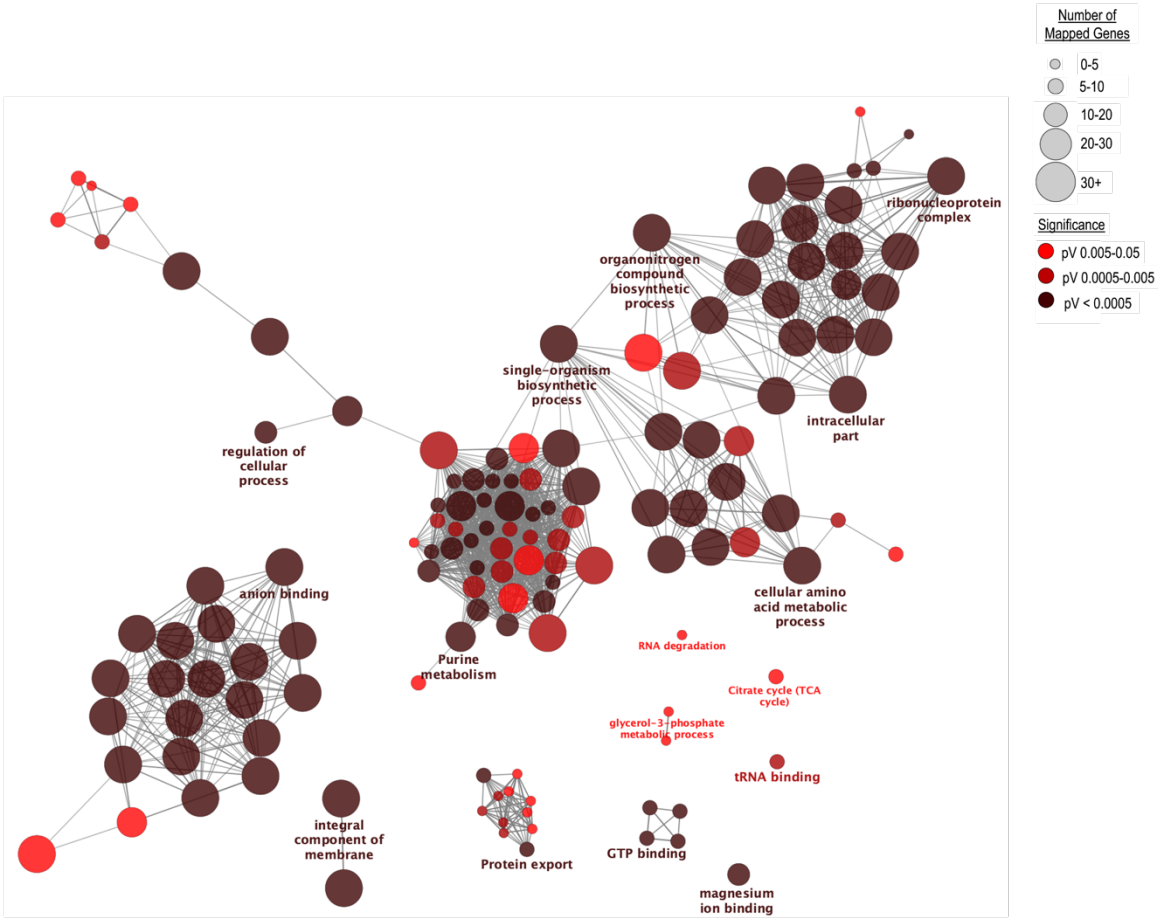

E

Wild-type Cytoplasm

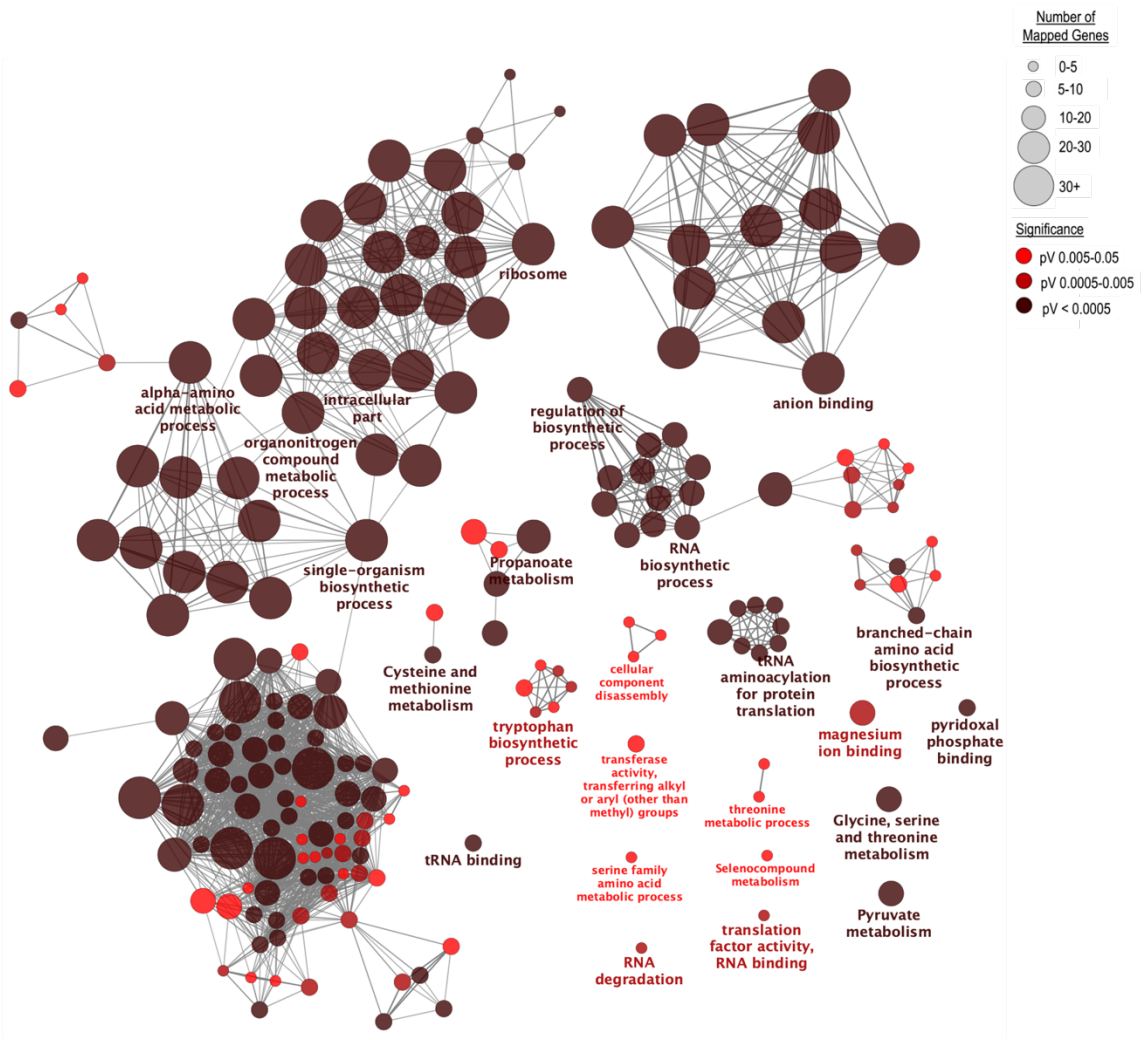

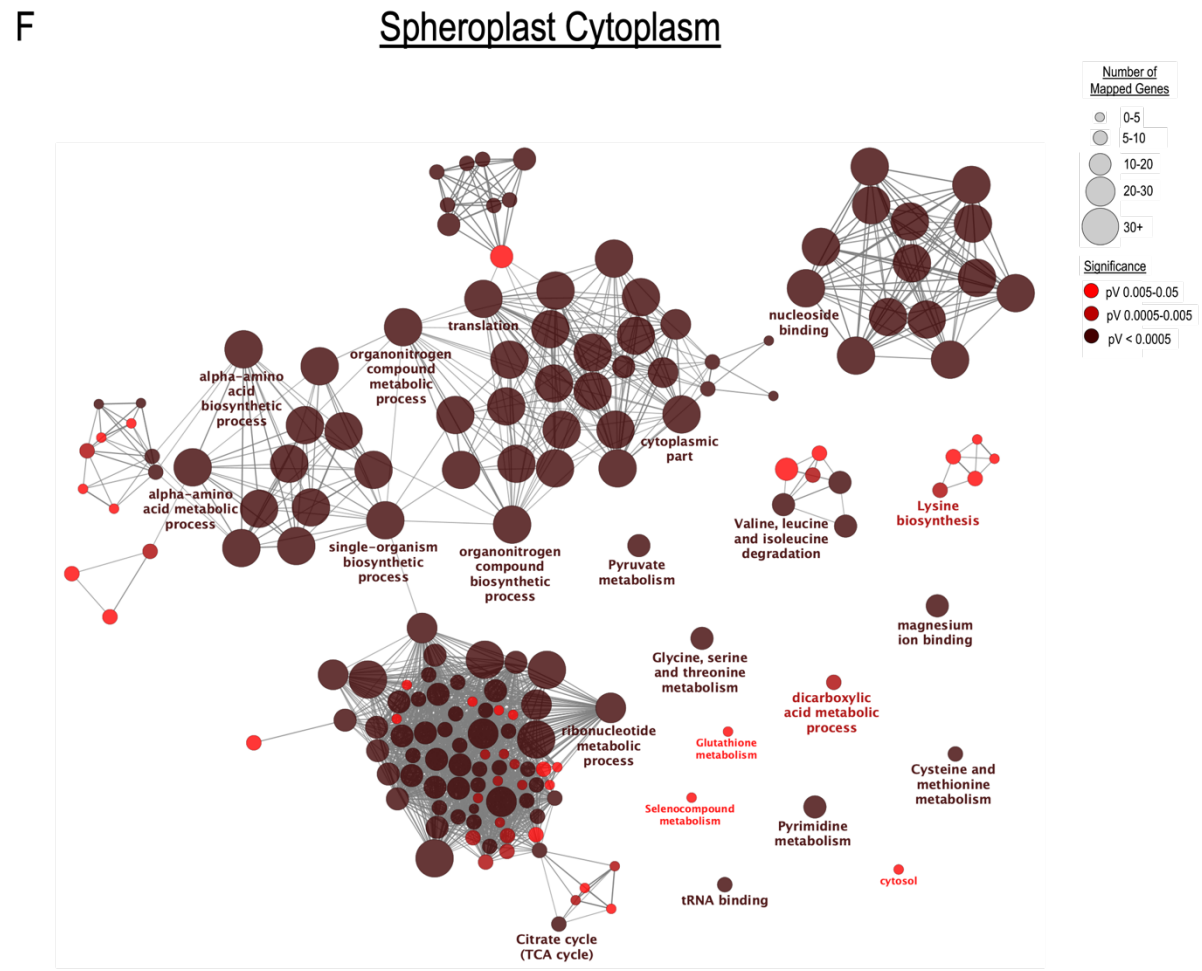

FIGURE 4.10. Altered protein content in spheroplasts. Functional categories from the Gene Ontology and KEGG databases were assigned to proteins present in each fraction for wild-type cell envelope (A), debris (C), and cytoplasm (E); or spheroplast cell envelope (B), debris (D), and cytoplasm (F). Node size represents the number of genes mapped to each functional category. Only functional categories that showed significant association ($p<0.05$) with identified proteins were included in the analysis. Analysis was carried out using ClueGO within Cytoscape.

Next, we sought to remove any cytoplasmic contaminants from the data that may have skewed the functional associations found in each fraction. To this end, we performed bioinformatic enrichment to filter out all proteins present in the cell envelope or cell debris fractions that were also found in the cytoplasmic samples. Cytoplasmic contaminants constituted 169 of the 244 proteins identified in the spheroplast cell envelope fraction and 148 of the 325 wild-type cell envelope proteins. Analysis of the proteins unique to these fractions provided further clarity on the proteins found in the cell envelope (**FIGURE 4.11**). For example, the proteins contained within the wild-type cell envelope following filtering of cytoplasmic proteins consisted solely of ABC transporters, protein exporters, and plasma membrane components (**FIGURE 4.11A**). In stark contrast, there was a notable reduction in proteins significantly linked to a functional category in the spheroplast cell envelope samples, with a few proteins assigned to protein export and transmembrane transport and others associated with cytoplasmic functions (**FIGURE 4.11B**). Of the 844 proteins present in the wild-type cell debris fraction, 523 were absent in the cytoplasmic fraction, while the spheroplast debris sample contained 476 proteins after removal of cytoplasmic contaminants. Functional annotation of these filtered protein sets showed similar results to those seen in the cell envelope. A majority of proteins found in the wild-type sample were linked to the ABC transporter superfamily, with others showing involvement in peptidoglycan biosynthesis, protein export, cell membrane and cell periphery (**FIGURE 4.11C**). In comparison, functional annotation of the spheroplast cell debris fraction revealed a subset of proteins involved in protein export, with the bulk of remaining proteins predicted to perform intracellular functions (**FIGURE 4.11D**).

A

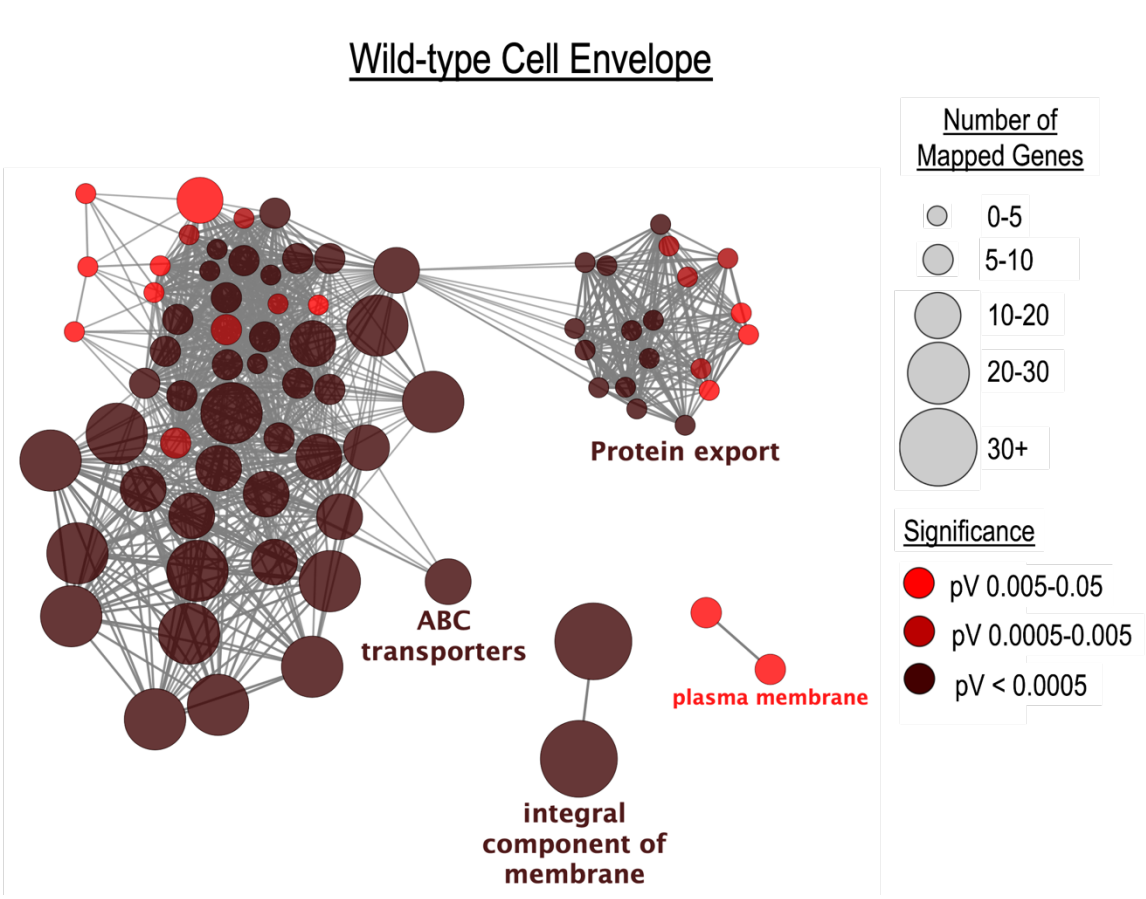
Wild-type Cell Envelope
Number of Mapped Genes
0-5
5-10
10-20
20-30
30+
Significance
pV 0.005-0.05
pV 0.0005-0.005
pV < 0.0005
Protein export
ABC transporters
plasma membrane
integral component of membrane

B

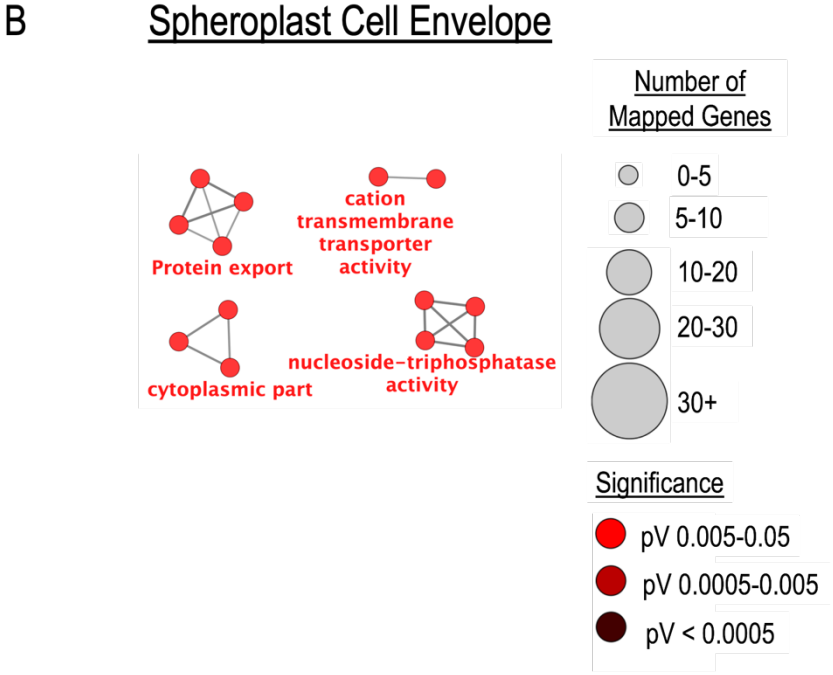
Spheroplast Cell Envelope
Number of Mapped Genes
0-5
5-10
10-20
20-30
30+
Significance
pV 0.005-0.05
pV 0.0005-0.005
pV < 0.0005
Protein export
cation transmembrane transporter activity
cytoplasmic part
nucleoside-triphosphatase activity

C

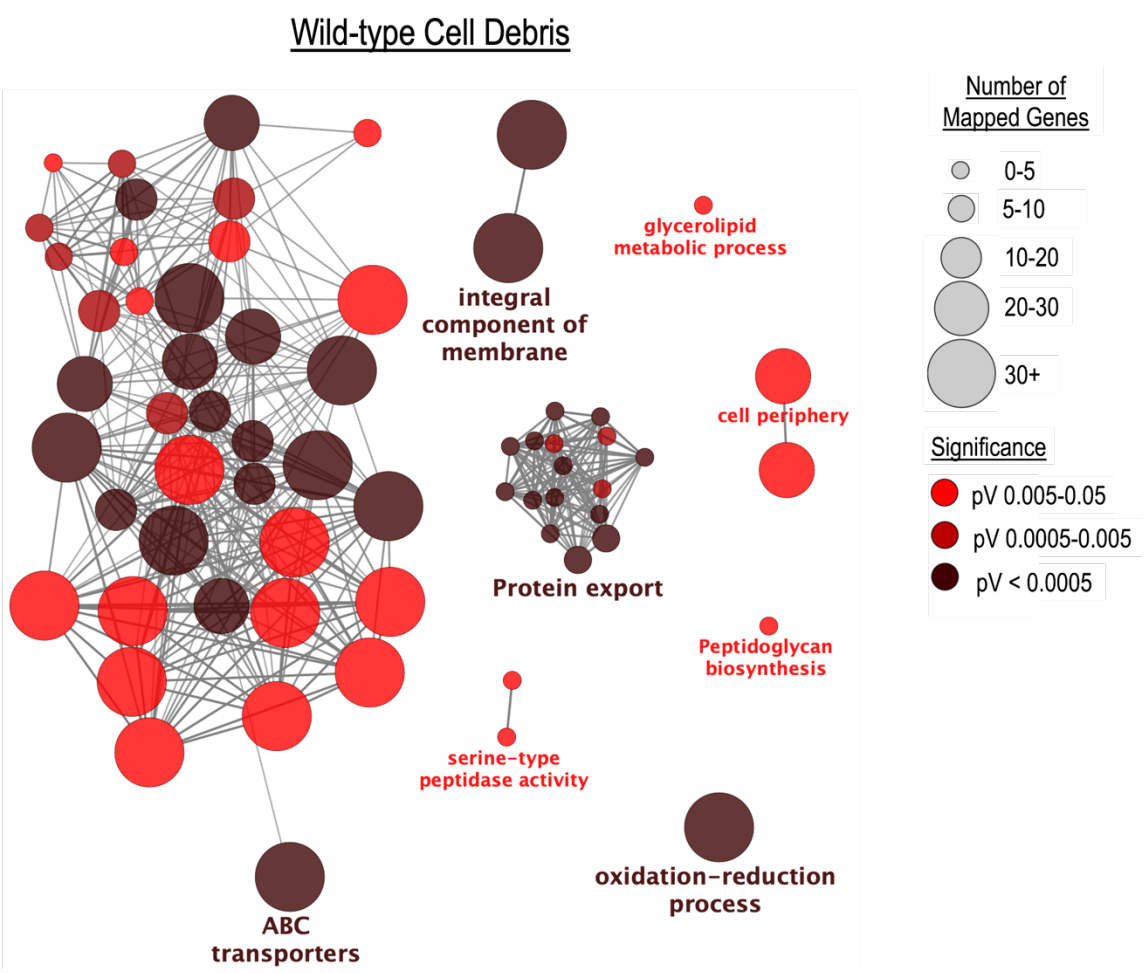
Wild-type Cell Debris
integral component of membrane
glycerolipid metabolic process
cell periphery
Protein export
Peptidoglycan biosynthesis
serine-type peptidase activity
oxidation-reduction process
ABC transporters
Number of Mapped Genes
0-5
5-10
10-20
20-30
30+
Significance
pV 0.005-0.05
pV 0.0005-0.005
pV < 0.0005

D

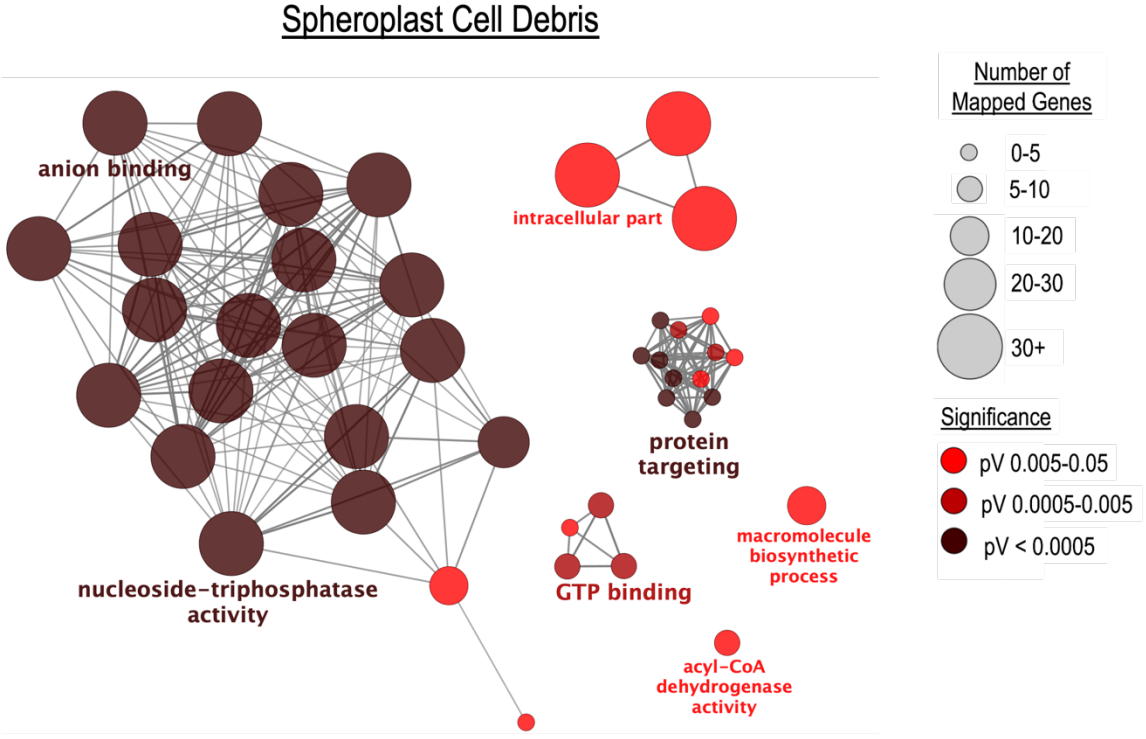
Spheroplast Cell Debris
anion binding
intracellular part
protein targeting
macromolecule biosynthetic process
GTP binding
nucleoside-triphosphatase activity
acyl-CoA dehydrogenase activity
Number of Mapped Genes
0-5
5-10
10-20
20-30
30+
Significance
pV 0.005-0.05
pV 0.0005-0.005
pV < 0.0005

FIGURE 4.11. Bioinformatic enrichment reveals absence of cell wall associated proteins in spheroplasts. Bioinformatic enrichment was performed to remove all proteins present in the cytoplasmic fractions from the debris and cell envelope protein lists. Functional categories from the Gene Ontology and KEGG databases were assigned to proteins present each fraction for wild-type cell envelope (A) and debris (C), or spheroplast cell envelope (B) and debris (D). Node size represents the number of genes mapped to each functional category. Only functional categories that showed significant association ($p<0.05$) with identified proteins were included in the analysis. Analysis performed using ClueGO within Cytoscape.

To gain insight into those proteins associated with significantly altered relative abundances in spheroplast *versus* wild-type fractions, we evaluated fold-change in label-free quantification (LFQ) values of proteins present under both conditions for each fraction. Comparison of the wild-type and spheroplast cell debris fractions yielded the most interesting findings (**FIGURE 4.12B, TABLE 4.2**), with both Ag85A and Ag85C – components of the mycolyltransferase complex necessary for mycolic acid biosynthesis[33] – showing 7.5-fold and 5-fold reductions, respectively, in relative abundance in spheroplasts. Other proteins showing decreased abundance included SubI which is involved in transmembrane transport, and the predicted secreted protein, MSMEG_3493. Within the subset of proteins exhibiting a decreased abundance of 2-fold or more in spheroplasts, 67 of the 120 cell debris proteins were known or predicted to be found in the cell envelope compartment (**TABLES 4.2 & 4.3**).

TABLE 4.2: Proteins displaying altered abundance in spheroplast debris fraction

Fold Change	Gene Name	Metabolic Function/Biological Process	Cellular Compartment	Essentiality (DeJesus[222])
-7,55	fbpB, fbpA	Antigen 85 complex	Extracellular region	GA, NE
-6,30	subI	Membrane transport	Periplasm	GD
-5,50	MSMEG 3493	Unknown	Unknown	NE
-4,95	fbpC	Antigen 85 complex	Extracellular region	NE
-4,85	cysA1	ABC transporter	Plasma membrane	GD
-4,83	cysA2	Thiosulfate sulfur-transferase	Unknown	GA
-4,49	MSMEG_6307	Glutamine-binding periplasmic protein	Periplasm	N/A
-4,49	mmplL4b	Transmembrane transport of fatty acids	Plasma membrane	NE
-4,29	MSMEG_2963	Lipoprotein	Plasma membrane	NE
-4,26	MSMEG_3599	Carbohydrate transport	Unknown	N/A
-4,22	MSMEG_3027	Conserved membrane protein	Unknown	NE
-4,21	sseC1	Sulphur metabolism	Unknown	GA
-4,20	MSMEG_3058	Lipoprotein	Unknown	N/A
-4,15	mmpL4	Transmembrane protein	Plasma membrane	NE
-4,15	oppA	Periplasmic lipoprotein	Plasma membrane	NE
-4,12	MSMEG_6242	Alcohol dehydrogenase	Unknown	N/A
-4,03	groES	Chaperone protein	Cytoplasm	ES
-3,77	MSMEG_0973	Conserved membrane protein	Integral to membrane	ES

-3,74	MSMEG_2820	Unknown	Unknown	N/A
-3,73	MSMEG_4561	Unknown	Unknown	N/A
-3,73	MSMEG_3280	Lipoprotein	Periplasm	N/A
-3,70	MSMEG_2727	Glutamate binding protein	Unknown	N/A
-3,62	MSMEG_2793	Sensor-type histidine kinase	Integral to membrane	N/A
-3,58	MSMEG_4535	Polysaccharide biosynthesis	Unknown	NE
-3,50	phoR	Sensor kinase	Integral to membrane	NE
-3,47	eccC1a	ESX conserved component	Integral to membrane	NE
-3,44	mmp14a	Transmembrane protein	Integral to membrane	N/A
-3,23	eccC3	ESX-1 type VII secretion system	Plasma membrane	ES
-3,22	MSMEG_1684	Unknown	Unknown	NE
-3,10	pknB	Transmembrane signal transduction	Integral to membrane	ES
-3,08	MSMEG_3235	ABC transporter	Periplasm	N/A
-3,02	MSMEG_4692	Unknown	Unknown	NE
-3,02	aftB	Probable conserved transmembrane protein/arabinan synthesis	Integral to membrane	ES
-3,00	MSMEG_1643	Unknown	Integral to membrane	N/A
-2,98	shdA	TCA cycle	Cytoplasm	NE
-2,95	MSMEG_3598	Periplasmic sugar-binding proteins	Periplasm	N/A
-2,94	sdhD	TCA cycle	Unknown	NE
-2,93	MSMEG_0987	Unknown	Integral to membrane	N/A
-2,92	fecB	Periplasmic binding protein	Unknown	NE
-2,89	cydA	Cytochrome	Membrane	NE
-2,87	acpM	Fatty acid biosynthesis	Cytoplasm	ES
-2,87	MSMEG_1060	DNA-binding	Unknown	N/A
-2,85	MSMEG_4560	Periplasmic binding protein	Periplasm	N/A
-2,84	MSMEG_5452	Predicted outer membrane protein	Unknown	NE
-2,82	MSMEG_5225	Unknown	Unknown	NE
-2,80	rocA	Peptidoglycan biosynthesis	Cell wall	GA
-2,78	lpqW	Lipid biosynthesis	Unknown	ES
-2,77	MSMEG_3641	Unknown	Integral to membrane	NE
-2,76	mkl	ABC transporter	Membrane	GA
-2,75	MSMEG_3103	Transketolase	Unknown	N/A
-2,75	MSMEG_2739	Possible conserved transmembrane protein	Integral to membrane	NE
-2,74	MSMEG_3250	ABC transporter	Unknown	N/A
-2,73	qcrC	Respiration, cytochrome	Plasma membrane	GD
-2,71	MSMEG_0412	Possible exported protein	Outer membrane	NE
-2,70	kanY	Unknown	Unknown	NE
-2,69	MSMEG_1517	Spfh domain/band 7 family protein, putative	Unknown	N/A

-2,68	MSMEG_4256	Unknown	Unknown	NE
-2,67	MSMEG_4484	Possible conserved transmembrane protein	Plasma membrane	GA
-2,66	ponA1	Peptidoglycan biosynthesis	Periplasm	NE
-2,65	mftD	Mycofactin synthesis	Unknown	NE
-2,60	nrdF2	Oxidation-reduction, DNA replication	Unknown	ES
-2,60	accD5	Fatty acid catabolism	Cytoplasm	ES
-2,59	MSMEG_6595	Secreted protein	Periplasm	N/A
-2,59	mspA	Porin	Extracellular region	N/A
-2,59	mspB	Porin	Extracellular region	N/A
-2,59	mspC	Porin	Extracellular region	N/A
-2,59	mspD	Porin	Extracellular region	N/A
-2,58	MSMEG_3050	Integration host factor	Unknown	N/A
-2,55	MSMEG_6518	Unknown	Unknown	N/A
-2,55	lppH	Lipoprotein	Membrane	N/A
-2,50	htrA	Serine protease	Unknown	ES
-2,50	ppiB	Protein folding	Unknown	GD
-2,48	MSMEG_6137	Non-ribosomal peptide synthetase	Unknown	N/A
-2,47	pntB	NAD(P) transhydrogenase	Unknown	N/A
-2,46	wag31	Cell division	Cytoplasm	ES
-2,46	qcrB	Respiration. Cytochrome	Plasma membrane	GD
-2,45	MSMEG_0750	Membrane protein	Plasma membrane	N/A
-2,44	rplO	Ribosomal protein	Cytoplasm	*Absent from study
-2,43	pntA	NAD(P) transhydrogenase	Integral to membrane	N/A
-2,43	MSMEG_6761	Glycerol-3-phosphate dehydrogenase 2	Unknown	N/A
-2,42	sucD	TCA cycle	Unknown	ES
-2,42	MSMEG_6942	Conserved transmembrane protein	Plasma membrane	ES
-2,41	MSMEG_0763	Antibiotic transporter	Integral to membrane	N/A
-2,41	ctaC	Cytochrome	Plasma membrane	GD
-2,38	MSMEG_6081	Probable conserved membrane protein	Integral to membrane	ES
-2,37	eccB3	Possible membrane protein	Plasma membrane	ES
-2,36	TB15.3	Stress response	Unknown	ES
-2,35	MSMEG_6502	Unknown	Unknown	N/A
-2,33	qcrA	Cytochrome	Integral to membrane	GD
-2,33	MSMEG_1053	Unknown	Unknown	N/A
-2,33	lepB	Signal peptidase	Plasma membrane	ES
-2,32	MSMEG_0643	Extracellular solute-binding protein	Periplasm	N/A
-2,31	secF	Protein export membrane protein	Plasma membrane	ES
-2,30	rpmF	Ribosomal protein	Cytoplasm	*Absent from study
-2,30	embC	Arabinan biosynthesis	Plasma membrane	ES
-2,28	MSMEG_3689	Sodium solute symporter	Plasma membrane	N/A

-2,28	moeA	Molybdopterin biosynthesis	Unknown	NE
-2,27	mmpL5	Membrane transport	Integral to membrane	N/A
-2,27	MSMEG_6929	Conserved transmembrane protein	Integral to membrane	ES
-2,26	htpX	Transmembrane protein	Plasma membrane	NE
-2,23	MSMEG_2936	Hydrolase	Unknown	ES
-2,22	bacA	ABC transporter	Plasma membrane	NE
-2,22	MSMEG_4273	Probable conserved transmembrane protein	Plasma membrane	NE
-2,22	MSMEG_1642	ABC transporter	Plasma membrane	NE
-2,22	MSMEG_3884	Probable membrane protein	Integral to membrane	NE
-2,21	MSMEG_0690	Iron-sulfur-binding reductase	Unknown	ES
-2,16	MSMEG_3247	ABC transporter substrate-binding protein	Unknown	N/A
-2,15	pstP	Phosphorylation	Plasma membrane	ES
-2,13	embB	Peptidoglycan biosynthesis	Plasma membrane	ES
-2,12	MSMEG_0007	Conserved membrane protein	Plasma membrane	NE
-2,12	embA	Arabinan biosynthesis	Plasma membrane	ES
-2,11	mmpS4	Probable conserved membrane protein	Unknown	NE
-2,09	MSMEG_3237	ATP-binding protein	Unknown	N/A
-2,09	fhaB	Signal transduction	Integral to membrane	NE
-2,09	MSMEG_5062	Probable transmembrane protein	Integral to membrane	NE
-2,08	MSMEG_1959	Membrane protein	Plasma membrane	NE
-2,05	sdhB	TCA cycle	Cytoplasm	NE
-2,04	accA3	Fatty acid biosynthesis	Cytoplasm	ES
-2,04	MSMEG_0976	Conserved hypothetical protein	Unknown	N/A
-2,01	secE1	Protein export	Plasma membrane	ES
-2,01	MSMEG_3636	ABC transporter	Periplasm	N/A
-2,01	aftC	Arabinan biosynthesis	Integral to membrane	ES
-2,00	lprG	Lipoprotein	Plasma membrane	NE
2,08	ffh	Export of extra-cytoplasmic proteins	Cytoplasm	ES
2,13	thiO	Co-factor biosynthesis	Unknown	ES
2,19	MSMEG_5782	ABC transporter	Unknown	N/A
2,22	ilvD	Valine and isoleucine biosynthesis	Cytoplasm	ES
2,26	MSMEG_3935	Unknown	Unknown	NE
2,28	rplF	Translation	Cytoplasm	ES
2,29	MSMEG_3950	Stress protein	Unknown	NE
2,30	secA2	Protein export	Plasma membrane	NE
2,34	dnaZX	DNA-binding	Cytoplasm	ES
2,36	coaA	Coenzyme-A biosynthesis	Cytoplasm	ES
2,37	MSMEG_5246	Oxidation-reduction	Unknown	NE
2,40	MSMEG_0216	3-hydroxyacyl-coa dehydrogenase	Unknown	N/A

2,40	alaS	Translation	Cytoplasm	ES
2,40	gadB	GABA production	Unknown	GA
2,42	nrdE	DNA replication	Unknown	ES
2,42	asnB	Asparagine biosynthesis	Unknown	ES
2,45	metK	Methyl cycle	Cytoplasm	ES
2,46	rho	Transcriptional regulation	Cytoplasm	ES
2,51	MSMEG_1843	Adenosylhomocysteinase	Unknown	N/A
2,56	MSMEG_1954	ABC transporter	Unknown	NE
2,58	mpa	Protein degradation	Unknown	NE
2,59	tuf	Translation	Cytoplasm	ES
2,60	MSMEG_3667	Para-nitrobenzyl esterase	Unknown	N/A
2,62	fadD32	Mycolic acid biosynthesis	Cytoplasm	ES
2,64	fgd1	F420-dependent dehydrogenase	Unknown	NE
2,64	glpX	Gluconeogenesis	Cytoplasm	NE
2,68	MSMEG_2788	Integral membrane protein	Unknown	NE
2,70	MSMEG_0415	Oxidation-reduction	Unknown	NE
2,73	MSMEG_0370	Unknown	Unknown	N/A
2,73	MSMEG_1058	Tnpr protein	Unknown	N/A
2,74	glpK	Glycerol kinase	Unknown	N/A
2,77	thrA	Threonine biosynthesis	Cytoplasm	ES
2,77	ribA2	Riboflavin biosynthesis	Unknown	ES
2,79	kasA	Fatty acid biosynthesis	Cytoplasm	ES
2,81	ispG	Oxidation-reduction	Unknown	ES
2,83	asd	Cell wall precursor biosynthesis	Cytoplasm	GD
2,84	MSMEG_1543	Aldehyde dehydrogenase	Unknown	N/A
2,84	sigA	RNA polymerase	Cytoplasm	ES
2,85	MSMEG_3952	Oxidation-reduction	Unknown	N/A
2,89	ksgA	RNA binding	Cytoplasm	NE
2,95	hadC	Fatty acid biosynthesis	Unknown	NE
3,00	dnaE1	DNA polymerase III	Cytoplasm	ES
3,01	MSMEG_2271	Hydrogenase accessory protein	Unknown	N/A
3,06	MSMEG_6512	Acyl-CoA dehydrogenase	Unknown	N/A
3,07	glnA2	Glutamine biosynthesis	Cytoplasm	NE
3,08	eccA1	ESX-1 type VII secretion system	Cytoplasm	NE
3,09	MSMEG_4645	TCA cycle	Unknown	GD
3,09	mtrA	Transcriptional regulation	Unknown	ES
3,13	clpP1	Protease	Cytoplasm	ES
3,13	deaD	Cold shock protein	Cytoplasm	NE
3,17	ftsZ	Cell division	Cytoplasm	ES
3,20	MSMEG_5199	Acyl-CoA dehydrogenase	Unknown	N/A
3,29	MSMEG_4646	Pyruvate synthase	Cytoplasm	GD
3,33	serC	Serine and pyroxidine biosynthesis	Cytoplasm	ES
3,33	crp	Transcriptional regulation	Intracellular	*Absent from study

3,41	pca	Gluconeogenesis	Cytoplasm	NE
3,43	inhA	Mycolic acid biosynthesis	Unknown	ES
3,44	MSMEG_0915	Kinase	Unknown	N/A
3,45	ilvC	Valine and isoleucine biosynthesis	Cytoplasm	ES
3,48	trpB	Tryptophan biosynthesis	Cytoplasm	ES
3,51	MSMEG_5512	Magnesium chelatase	Intracellular	NE
3,56	rpoB	RNA polymerase	Cytoplasm	ES
3,60	MSMEG_3124	ABC transporter	Unknown	ES
3,63	MSMEG_5068	ATP-binding	Unknown	ES
3,63	hupB	DNA-binding	Unknown	GD
3,63	fabG1	Fatty acid biosynthesis	Cytoplasm	ES
3,66	MSMEG_4700	ABC transporter	Unknown	ES
3,67	fadB	Fatty acid degradation	Cytoplasm	NE
3,71	MSMEG_3080	Regulation of cell shape	Cytoplasm	NE
3,76	cofD	Co-factor biosynthesis	Unknown	NE
3,77	MSMEG_3253	Unknown	Unknown	N/A
3,87	polA	DNA polymerase	Cytoplasm	ES
3,91	guaA	ATP-binding	Unknown	ES
3,94	gap	Glycolysis	Cytoplasm	GD
3,99	glyS	Translation	Cytoplasm	ES
4,02	cysH	Cysteine biosynthesis	Cytoplasm	GD
4,04	serA1	Serine biosynthesis	Cytoplasm	ES
4,07	MSMEG 3965	Unknown	Unknown	N/A
4,13	MSMEG 0688	Aspartate aminotransferase	Unknown	ES
4,17	MSMEG_0239	O-acetylhomoserine/O-acetylserine sulfhydrylase	Unknown	N/A
4,23	clpP2	Protease	Cytoplasm	ES
4,24	ilvB1	Valine and isoleucine biosynthesis	Cytoplasm	ES
4,24	prsA	Ribose-phosphate pyrophosphokinase	Cytoplasm	ES
4,29	accD6	Fatty acid biosynthesis	Cytoplasm	GD
4,34	fadE25	Lipid degradation	Unknown	NE
4,38	sufB	Fes assembly protein	Unknown	N/A
4,48	murA	Peptidoglycan biosynthesis	Cytoplasm	ES
4,65	fadA3	Lipid degradation	Unknown	GA
4,69	carB	Arginine and pyrimidine biosynthesis	Cytoplasm	ES
4,70	pyrG	Pyrimidine biosynthesis	Unknown	ES
4,72	gyrB	DNA gyrase	Cytoplasm	ES
4,77	MSMEG_1568	Glutamine biosynthesis	Cytoplasm	N/A
4,83	clpX	Protein degradation	Unknown	ES
5,07	Ercc3	Nucleotide excision repair	Unknown	NE
5,31	moeB1	Molybdopterin biosynthesis	Unknown	ES
5,44	MSMEG_1516	Thioredoxin reductase	Unknown	N/A
5,73	kasB	Fatty acid biosynthesis	Cytoplasm	NE

5,88	purL	Purine biosynthesis	Cytoplasm	ES
5,99	MSMEG_0102	Oxidation-reduction	Unknown	N/A
6,11	pafA	Ligase	Unknown	NE
6,33	MSMEG_1682	Monooxygenase activity	Unknown	N/A
6,76	guaB2	Purine biosynthesis	Cytoplasm	ES

Analysis of the proteins in the cell envelope fraction showing a significant decrease in abundance revealed a similar trend to that which was observed in the cell debris. The membrane transport protein, SubI, appears here again as well as a total of 9 of the proteins showing decreased abundance predicted to reside in the cell envelope compartment.

TABLE 4.3: Proteins displaying altered abundance in spheroplast cell envelope fraction

Fold Change	Gene Name	Metabolic Function/Biological Process	Cellular Compartment	Essentiality (DeJesus[222])
-6,61	subI	Membrane transport	Periplasm	GD
-3,04	MSMEG_3058	Lipoprotein	Unknown	N/A
-3,02	MSMEG_0643	Extracellular solute-binding protein	Periplasm	N/A
-2,99	MSMEG_2727	Glutamate binding protein	Periplasm	N/A
-2,90	MSMEG_6761	Glycerol-3-phosphate dehydrogenase 2	Unknown	N/A
-2,72	rpsL	Translation	Cytoplasm	ES
-2,62	sdhB	TCA cycle	Cytoplasm	NE
-2,62	shdA	TCA cycle	Cytoplasm	NE
-2,53	pknA	Signal transduction	Plasma membrane	ES
-2,36	MSMEG_3235	ABC transporter	Periplasm	N/A
-2,30	MSMEG_5225	Unknown	Unknown	NE
-2,22	sugC	ABC transporter	Plasma membrane	NE
-2,15	pntB	NAD(P) transhydrogenase	Integral to membrane	N/A
-2,10	MSMEG_1642	ABC transporter	Plasma membrane	NE
-2,05	MSMEG_3811	Stress response	Unknown	ES
-2,05	rpsJ	Translation	Cytoplasm	GD
2,15	hupB	DNA-binding	Extracellular region	GD
2,15	metK	Methyl cycle	Cytoplasm	ES
2,15	accD6	Fatty acid biosynthesis	Cytoplasm	GD
2,16	clpX	Protein degradation	Unknown	ES
2,17	glyS	Translation	Cytoplasm	ES
2,19	ychF	(p)ppGpp synthesis	Intracellular	NE
2,30	MSMEG_4700	ABC transporter	Unknown	ES
2,30	rplF	Translation	Cytoplasm	ES
2,39	murA	Peptidoglycan biosynthesis	Cytoplasm	ES
2,42	sppA	Proteolysis	Plasma membrane	NE

2,44	ilvC	Valine and isoleucine biosynthesis	Cytoplasm	ES
2,81	gap	Glycolysis	Cytoplasm	GD
2,90	crp	Transcriptional regulation	Intracellular	*Absent from study
2,98	pstS	ABC transporter	ABC transporter complex	N/A
3,11	sigA	RNA polymerase	Cytoplasm	ES
3,17	rpoA	RNA polymerase	Cytoplasm	ES
3,21	MSMEG_1516	Thioredoxin reductase	Unknown	N/A
3,36	cobI	Cobalamin synthesis	Cytoplasm	NE
3,41	serA1	Serine biosynthesis	Cytoplasm	ES
3,59	MSMEG_5706	Nucleotide excision repair	Unknown	NE
4,00	fas	Fatty acid biosynthesis	Cytoplasm	ES
4,99	rpoB	RNA polymerase	Cytoplasm	ES
5,52	fadA3	Lipid degradation	Unknown	GA
5,82	guaB2	Purine biosynthesis	Cytoplasm	ES

Among the proteins demonstrating lower abundances in the spheroplast cytoplasm were Ag85A, KasA and KasB, other enzymes known to be involved in mycolic acid synthesis (FIGURE 4.12C)[33,223]. However, only 2 of the 33 proteins with reduced abundance in spheroplast cytoplasm could be classified as cell envelope associated (TABLE 4.4), not unsurprising given that one wouldn't necessarily expect to find proteins associated with the cell envelope in the cytoplasmic fraction.

TABLE 4.4: Proteins displaying altered abundance in spheroplast cytoplasmic fraction

Fold Change	Gene Name	Metabolic Function/Biological Process	Cellular Compartment	Essentiality (DeJesus[222])
-5,61	MSMEG_6761	Glycerol-3-phosphate dehydrogenase 2	Unknown	N/A
-5,40	MSMEG_6242	Alcohol dehydrogenase	Unknown	N/A
-5,12	sirA	Oxidation-reduction	Unknown	NE
-4,34	kasA	Fatty acid biosynthesis	Cytoplasm	ES
-4,23	acs	Acetyl-CoA synthetase	Unknown	NE
-4,18	glpK	Glycerol kinase	Unknown	N/A
-3,93	sseC1	Sulphur metabolism	Unknown	GA
-3,70	MSMEG_4645	TCA cycle	Unknown	GD
-3,68	MSMEG_0408	Polyketide synthase	Unknown	N/A
-3,53	fadB	Fatty acid degradation	Cytoplasm	NE
-3,50	MSMEG_1543	Aldehyde dehydrogenase	Unknown	N/A
-3,49	MSMEG_2079	Oxidation-reduction	Unknown	N/A
-3,33	MSMEG_1547	Glycerol dehydratase	Unknown	N/A
-3,13	MSMEG_3945	Stress protein	Unknown	GA
-3,03	cysA2	Thiosulfate sulfur-transferase	Unknown	GA

-2,89	gltB	Glutamate synthase	Unknown	ES
-2,56	kasB	Fatty acid biosynthesis	Cytoplasm	NE
-2,53	MSMEG_0400	Mycobactin biosynthesis	Unknown	N/A
-2,52	metC	Amino acid metabolism	Unknown	NE
-2,48	ilvB1	Valine and isoleucine biosynthesis	Cytoplasm	ES
-2,48	thiG	Thiazole biosynthesis	Cytoplasm	ES
-2,45	fadE5	Lipid metabolism	Unknown	NE
-2,35	fbpB, fbpA	Antigen 85 complex	Extracellular region	GA, NE
-2,35	tuf	Translation	Cytoplasm	ES
-2,30	MSMEG_5404	Propionate-CoA ligase	Unknown	N/A
-2,26	hybC	Hydrogenase-2	Unknown	N/A
-2,21	MSMEG_0415	Oxidation-reduction	Unknown	NE
-2,19	MSMEG_6512	Acyl-CoA dehydrogenase	Unknown	N/A
-2,13	canA	Anhydrase	Unknown	NE
-2,12	MSMEG_5245	Stress response	Unknown	NE
-2,11	MSMEG_1516	Thioredoxin reductase	Unknown	N/A
-2,08	subI	Membrane transport	Periplasm	GD
-2,02	desA1	Fatty acid desaturase	Unknown	ES
2,00	MSMEG_6059	Catalytic activity	Unknown	N/A
2,01	MSMEG_4971	Possible alanine rich oxidoreductase	Unknown	NE
2,09	glfT2	Galactan biosynthesis	Unknown	ES
2,17	guaB1	Purine biosynthesis	Unknown	GA
2,20	MSMEG_4633	Peptidase	Unknown	N/A
2,24	prcA	Protein degradation	Cytoplasm	ES
2,25	MSMEG_2410	Possible conserved membrane or secreted protein	Integral to membrane	ES
2,25	atpG	ATP synthase	Plasma membrane	ES
2,31	add	Purine biosynthesis	Unknown	NE
2,37	echA8	Fatty acid oxidation	Cytoplasm	NE
2,62	atpC	ATP synthase	Plasma membrane	*Absent from study
2,91	MSMEG_5454	Hydrolase	Unknown	N/A
2,96	ndh	Electron transfer	Integral to membrane	GD
2,96	MSMEG_1517	Spfh domain/band 7 family protein, putative	Unknown	N/A
2,98	fadD31	Lipid degradation	Cytoplasm	GA
3,13	MSMEG_3620	Oxidation-reduction	Unknown	GA
3,21	ftsH	Cell division	Plasma membrane	NE
3,62	eis	Intracellular survival	Extracellular region	NE
4,76	pstS	ABC transporter	ABC transporter complex	N/A

Proteins with elevated abundance in spheroplasts were those involved in RNA and lipid metabolism and peptidoglycan biosynthesis (**FIGURE 4.12 A & B**), with GuaB, a key enzyme in purine biosynthesis, showing the greatest increase in abundance in both the cell debris and cell envelope fractions of the spheroplast samples (6,8-fold and 5,8-fold higher abundance, respectively) in comparison to the wild-type[224]. The spheroplast cytoplasmic fraction also revealed a greater abundance of the ABC transporter, MSMEG_5782, and FtsH, a transmembrane protein involved in cell division (**FIGURE 4.12C**). Neither of these proteins was expected to be located in the cytoplasm, suggesting the over-representation relative to wild-type might result from loss of the cell envelope compartment in spheroplasts. Indeed, around 37% of the proteins with increased abundance in the spheroplast cytoplasm were predicted to be cell envelope associated. Together, these data supported the notion that the spheroplasted bacilli underwent extensive loss of cell wall structure.

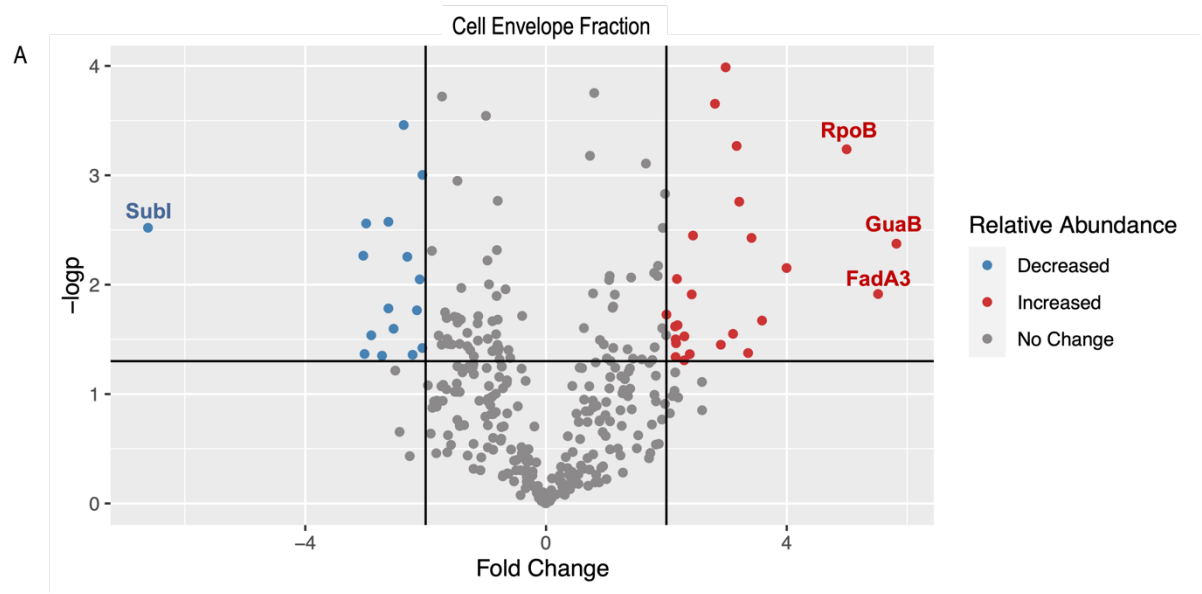

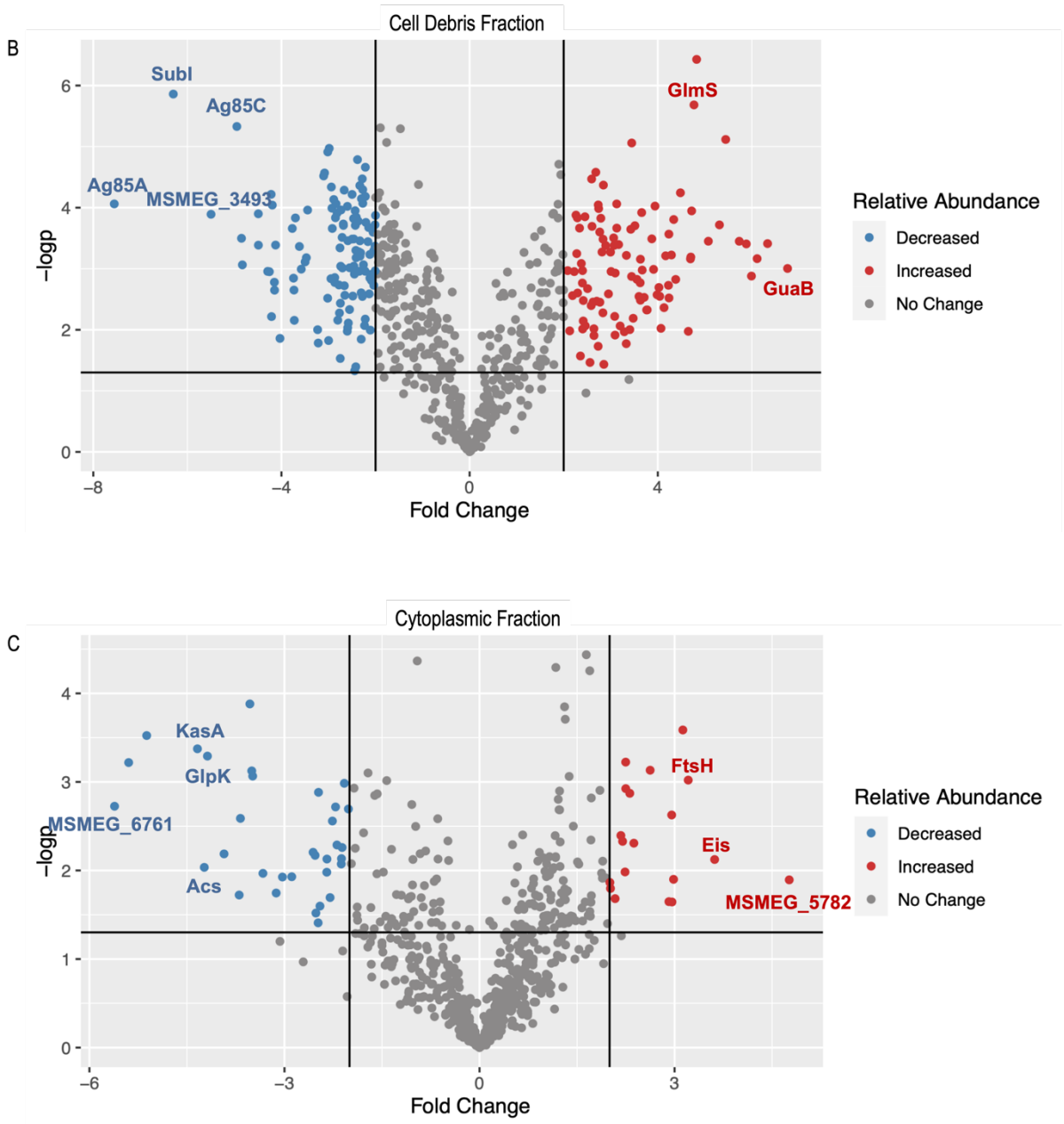

FIGURE 4.12. Spheroplasts exhibit decreased abundance of cell wall associated proteins. Protein abundances were compared between spheroplasts and wild-type cells for each fraction: (A) Cell Envelope, (B) Cell Debris, and (C) Cytoplasm. Volcano plots represent the log2 fold-change in protein abundance plotted against -logP; proteins with significant changes in abundance are represented in blue (decreased abundance) and red (increased abundance). Proteins of interest are labelled; for detailed lists, see Tables 4.2-4.4. Cutoff points were set at 2-fold change in abundance and logP 0.05. Plots were generated in R Studio (See Supp. Methods for code).

ANTIBIOTIC EFFICACY IN SPHEROPLASTS

Although we were unable to generate spheroplasts that were capable of proliferating at a rate comparable to that of wild-type *Msm*, we wanted to ascertain whether antibiotic efficacy was altered in these cell wall-deficient variants. To this end, we implemented a standard microplate Alamar Blue assay (MABA) but, owing to the near-absent replicative capacity of spheroplasts, we did not dilute these cultures before

addition to the 96-well plate. We decided to explore the efficacy of two frontline anti-TB drugs with different mechanisms of action – rifampicin, targeting RNA synthesis, and ethambutol, targeting arabinogalactan/mycolic acid synthesis – to assess the impact of cell wall deficiency on bacterial killing. Rifampicin treatment showed a high level of efficacy in spheroplasts, although only reaching 75% inhibition at the highest concentration (100μM) compared to 100% inhibition of wild-type cells observed at 50μM (**FIGURE 4.13A**). This suggested that spheroplasts still harbor some level of RNA polymerase activity which is impaired by rifampicin treatment, leading to a reduction in viability. In contrast, ethambutol displayed no inhibitory efficacy against spheroplasts but was able to reach 100% inhibition in cell wall replete bacilli at a concentration of just 6.25μM (**FIGURE 4.13B**). This result suggested that lysozyme-mediated depletion of cell wall components can result in generation of viable organisms that show resistance to cell wall-targeting antibiotics.

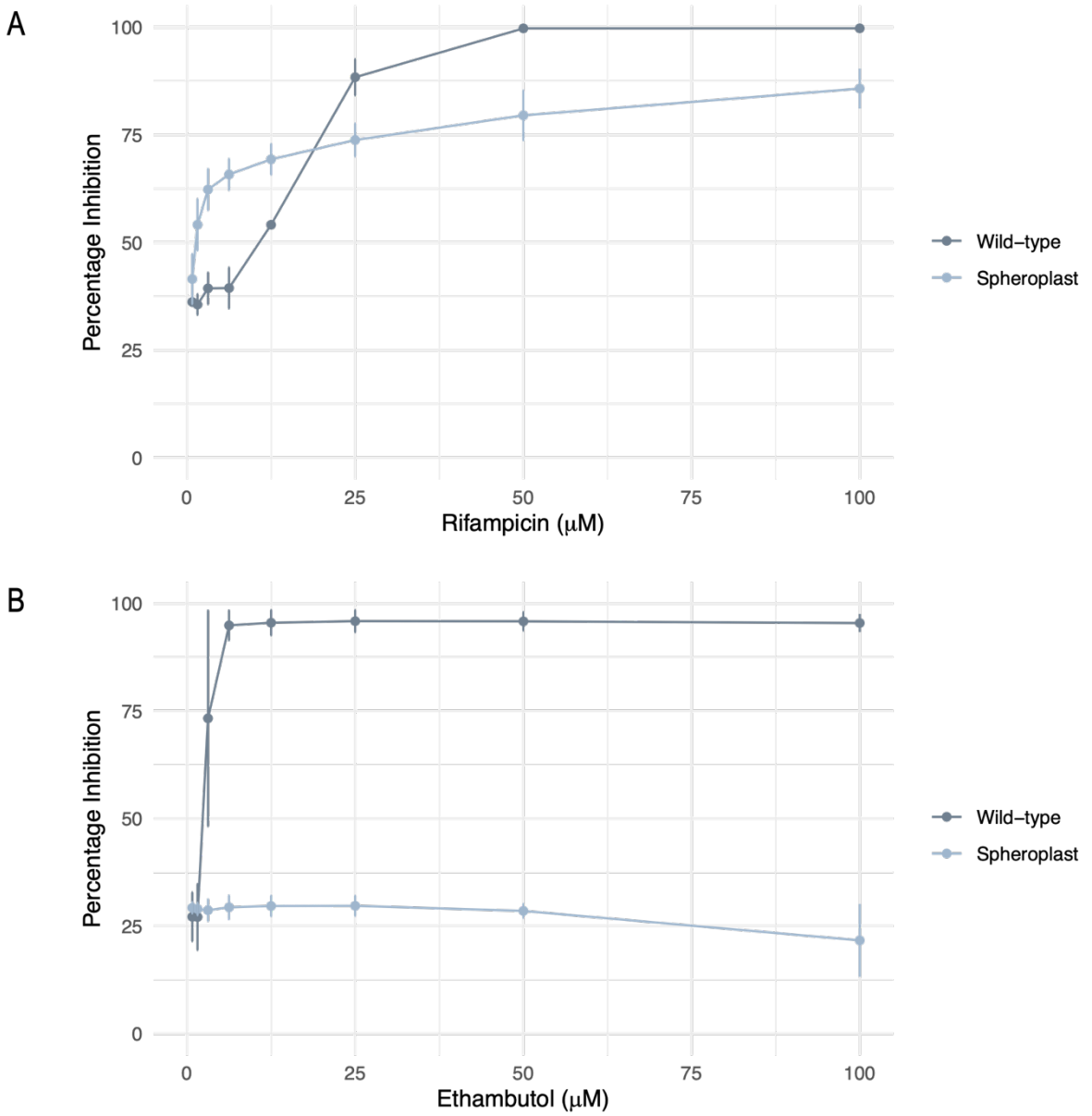

FIGURE 4.13. Altered drug efficacy in spheroplasts. Microplate Alamar Blue Assays (MABAs) were performed on wild-type and spheroplast *Msm* to evaluate the inhibitory activities of rifampicin (A) and ethambutol (B). Absorbance readings were taken using the FLUOstar OPTIMA microplate reader, and values were normalized against growth and no growth controls. All assays were performed in triplicate.

Discussion

LYSOZYME TREATMENT RESULTS IN CELL WALL DEFICIENCY

Several methods for the generation of CWD bacteria exist, including treatment with cell wall targeting antibiotics such as penicillin, cell wall degrading enzymes such as lysozyme, and genetic manipulations[170,180,207]. Owing to the innate resistance of mycobacteria to many cell wall-targeting antibiotics (resulting from a combination of cell wall impenetrability and the presence of degrading enzymes such as β-lactamases), we opted to investigate generation of spheroplasts via an enzymatic approach[225]. We adapted a protocol from Udou et al. utilizing a sucrose buffered, TSB-based medium containing lysozyme that has been adopted by several others in the field[53,180,226]. After experiencing difficulties with contamination in this nutrient-rich medium, we opted to utilize an *Msm* bioreporter mutant expressing an endogenous fluorophore that allowed microscopic validation of spheroplast formation. Using this approach, we were able to successfully generate spherical variants of *Msm*, utilizing previously established methods, that maintained fluorescence; thereafter, we proceeded to investigate the ability of these CWD variants to survive in different media. In light of reports highlighting their osmotic sensitivity, we saw this as an initial means of validating loss of cell wall components[180,227,228]. When transitioning lysozyme-treated *Msm* to standard 7H9 media, we observed lysis; in contrast, culture in any sucrose-buffered nutrient-rich medium provided a protective environment for the maintenance of spheroplasts. These findings supported the notion of cell wall deficiency, but we wished to investigate this further using quantitative techniques.

Time-lapse microscopy has been used to visualize formation of CWD variants of various bacterial species, but there are very few equivalent reports in mycobacteria[227,229]. We wished to observe the time required to undergo this transformation and the mechanisms employed by *Msm* to “escape” the cell wall and exist in a wall-deficient state. Utilization of a CellASIC® ONIX2 microfluidic device allowed us to load cell wall-replete organisms into the viewing chamber and perfuse lysozyme-containing media across the sample. Conversion to a CWD state took place as early as 7h into treatment and these variants persisted in the media for the 18h duration of the experiment. It was intriguing to observe the conversion of some bacilli into a single spherical daughter cell whereas others appeared to split into two or three spherical cells. This may be an indicator of the stage of replication within each recorded cell, with those having recently undergone cell division developing into a single spheroplast and those that have elongated and replicated their DNA in preparation for division being capable of splitting into several wall-deficient daughter cells. The influence of replicative state and/or cell cycle stage on spheroplast formation is a potential avenue for future study. In support of validating loss of cell wall components, time-lapse

microscopy revealed a notable decrease in phase contrast when rod-shaped bacilli converted to a spherical form, indicative of decreased density that could be correlated to loss of cell wall mass.

FLUORESCENCE MICROSCOPY REVEALS LOSS OF CELL WALL COMPONENTS

To quantitatively assess the loss of cell wall components in lysozyme-treated *Msm*, we used fluorescence microscopy to provide further validation of the efficacy of spheroplasting protocol. We began by assessing loss of the mycomembrane layer by applying DMN-trehalose, a stain that is metabolically incorporated into mycolic acids in place of trehalose mono- and di-mycolates[211]. Owing to the morphological changes experienced during spheroplasting, we were cautious in comparing total fluorescence read-outs between the cell wall replete rod-shaped bacteria and their cell wall deficient spherical counterparts. Our main concern revolved around the fluorescence existing in out-of-focus z-planes that may be under-represented in a 2D image, with rod-shaped *Msm* typically having a cell width/depth of ~0.6µm and the assumption that the spherical nature of the cell wall deficient bacteria would result in a z-plane depth equal to that of the diameter (1.6-1.9µm) However, owing to the nature of fluorescence detection on a wide-field microscope, such that light from all z-planes is detected in a 2D image, we proceeded to analyze whole cell fluorescence while simultaneously carrying out analyses of pixel intensity across the medial axis of each bacterium. Medial axis intensity profiling provided information about the distribution of fluorescence across each cell type while also providing a level of validation for total fluorescence calculations. While total fluorescence calculations revealed a significant decrease in DMN-tre signal in spheroplasts, medial axis profiling indicated that any residual fluorescence showed no localization to the poles and site of division as is expected for cell wall biosynthesis[230]. These findings provided a strong indication of near-complete absence of active mycomembrane synthesis in cell wall deficient *Msm*. A similar study was carried out using a metabolically incorporated D-alanine analogue, NADA, that is inserted into sites of active peptidoglycan biogenesis[213]. Quantification of whole-cell fluorescence revealed similar findings to those of DMN-tre, a significant reduction in NADA staining in spheroplasts and total loss of fluorescent localization to the poles of the cells. Together, these findings support our previous observations that lysozyme treatment results in near-complete degradation of both the mycolic acid and peptidoglycan layers of *Msm*.

As an organism cannot exist without some form of barrier from its environment, we next looked at evidence for the existence of a plasma membrane in spheroplasts. Application of FM™4-64, a non-specific styryl dye that is not metabolically incorporated, we observe no polar localization and therefore carrying out medial axis profiling was of no benefit. A comparison of whole cell fluorescence between cell

wall replete and cell wall deficient forms of *Msm* revealed a significant decrease in FM™4-64 fluorescence in spheroplasts. Given the non-specific nature of this lipophilic dye, it was unsurprising that a strong fluorescent signal was detected in the lipid-rich layers of the cell wall, surpassing that observed in organisms retaining only the plasma membrane. However, whereas the mycomembrane and peptidoglycan staining experiments displayed a level of fluorescence in spheroplasts that was invisible to the naked eye and no apparent localization patterns, the FM 4-64 dye was readily visualized in both wall replete and deficient variants and shows clear localization to the perimeter of both cell types. These results displayed retention of the plasma membrane in spheroplasts while simultaneously exhibiting an increased fluorescent signal in wall replete organisms that signified higher lipid content in the exterior of these organisms, further supporting the concept of the absence of such components in spheroplasts.

POTENTIAL MECHANISM OF REPLICATION IN CWD ORGANISMS

Detailed studies in CWD *B. subtilis* have revealed a primitive mechanism of replication that relies heavily on an overproduction of membrane components that results in an atypical surface area to volume ratio that the organism attempts to resolve by means of membrane extrusion[215]. This means of division depends on shape distortion and is postulated to represent the mode of replication employed by primitive prokaryotes before the advent of the cell wall; modern bacteria are thought to retain the ability to carry out such cell division in the event that cell wall synthesis in compromised[231]. These observations were corroborated by studies revealing that the FtsZ protein, known to be essential in canonical cell division, became redundant in a cell wall deficient background[170]. This led us to question whether the same was true in mycobacteria; to that end, time-lapse microscopy was implemented to investigate the potential for CWD *Msm* to undergo replication. We observed excess membrane synthesis and blebbing as previously described in *B. subtilis*, supporting the view that, in the absence of the rigid structural support offered by the cell wall, spheroplast bacteria implement a means of replication that does not mirror canonical processes[215].

The potential for bacteria to undergo replication in the absence of typical replicative mechanisms presents many questions regarding the ability of cell wall deficient variants to survive without implementing processes long considered to be essential to bacterial life. The replication and division machinery utilized by mycobacteria are the subject of extensive research, with evidence supporting roles for several regulatory proteins and enzymes in ensuring correct partitioning of chromosomes prior to cell division[232,233]. Essential to this process are the DNA-binding protein, ParB, which ensures appropriate chromosomal segregation and localization of newly formed replisomes; and Wag31, a protein that

recognizes membrane curvature at the poles and is thought to recruit components of the elongation complex in preparation for cell division[233,234]. Successful cell division requires migration of newly replicated chromosomes towards the poles of the cell before initiation of the division ring at the mid-cell, a process that is lost in ParB-deficient *Msm*[107]. This knowledge, accompanied by observations made about the replicative mechanisms employed by cell wall deficient bacteria, led us to question the spatial dynamics of the ParB protein in *Msm* spheroplasts. The ParB protein binds to sites near the origin of replication, and fluorescently tagged ParB can be visualized as a defined focus at this location, situated along the mid-cell following cell division and developing into two distinct foci following DNA replication which then migrate towards the poles[107]. In the absence of typical replicative mechanisms and a change in cell shape that is likely to disrupt the Wag31 signaling mechanisms that depend on membrane curvature along the cell poles, we questioned whether cell wall deficient organisms would maintain these ParB migration dynamics. Enumeration of ParB::mCherry foci revealed a loss of focus formation in spheroplast *Msm* implying some form of dysregulation that inhibits the specific binding of this protein at the origin of replication. Where distinct foci that migrated towards the poles were seen in cell wall replete bacilli as expected, the diffusion of ParB::mCherry fluorescent signal in spheroplasts indicates that the cells are under stress due to their cell wall deficient state or, as suggested previously, do not follow the canonical route for DNA replication and cell division. These results were corroborated by investigations using an exogenous nucleic acid stain, Syto9, which showed a similar capacity to form foci.

CELL WALL DEFICIENCY CAUSES OXIDATIVE STRESS

Oxidative stress is a well-reported phenomenon in bacteria, resulting in poor growth dynamics and increased mutagenesis[217]. As bacterial life evolved in an oxygen-depleted environment, the rapid oxygenation of the atmosphere that resulted from the evolution of photosynthetic organisms presented a critical turn point for bacteria, necessitating development of effective coping strategies to survive in oxygen-rich conditions[217]. Reactive oxygen species arise when oxygen is partially reduced, causing damage to key macromolecules such as nucleic acids, proteins and lipids[235]. Although bacteria have evolved several defense mechanisms to combat the oxidative stress that arises from ROS generation, including ROS scavengers and protective enzymes, damage to metabolites can result in high levels of toxicity and cause mutations to arise[235].

Oxidative stress was first recognized as playing a key role in the survival of CWD bacteria by Kawai et al. in 2015[170]. Their findings suggested that toxic levels of ROS are produced due to the metabolic imbalance created by removal of the cell wall, and that this oxidative stress is responsible for the inability

of unstable L-form bacteria to undergo replication[170]. Mutation of the *ispA* gene caused downstream synthesis inhibition of menaquinone, an electron transport chain (ETC) component resulting in stable growth of cell wall deficient *B. subtilis*[170]. The authors concluded that this mutation was essential in decreasing ETC activity to limit ROS generation, leading to a stabilizing phenotype for cell wall deficiency[170]. Our inability to generate CWD *Msm* that exhibited stable replicative ability led us to question whether elevated levels of ROS were responsible. As ROS are known to cause damage to nucleotides, proteins and lipids, we exploited a fatty acid analogue, C11-BODIPY to assess levels of lipid peroxidation in spheroplast *Msm*[217,235]. Using hydrogen peroxide (H_2O_2)-treated wild-type bacteria as a positive control for oxidative stress, we compared lipid peroxidation in spheroplasts to that of wall-replete wild type *Msm*. Our results showed a significant elevation in lipid peroxidation in cell wall deficient organisms when compared to both untreated and H_2O_2-treated wild-type bacilli. This was in agreement with studies conducted in *B. subtilis* and provided evidence of elevated levels of ROS in spheroplasts which may have a critical role to play in the fragility of these variants[170]. As the mycobacterial cell envelope constitutes 40% of the total dry mass of the organism, it is reasonable to assume that loss of these components would result in a severe metabolic imbalance that is likely have detrimental effects on survival[39].

MASS SPECTROMETRY CONFIRMS CELL WALL DEFICIENCY

Several proteomic studies into the composition of the mycobacterial cell wall have been conducted in recent years, each employing various techniques of isolating cell wall associated proteins from those found in the cytoplasmic compartment. One such approach applied sucrose density gradients to separate plasma membrane proteins that showed close association with the cell wall from those that were distinctly present in the plasma membrane alone[236]. In doing so, the authors were able to identify 626 proteins associated with the cell wall and 240 that were enriched for the plasma membrane and isolate several plasma membrane proteins that play an essential role in the biosynthesis of cell wall components[236]. In another study, a gel-free approach was implemented whereby centrifugation at high speeds allowed for separation of cell wall proteins from those of the cytoplasm to ascertain the effects of rifampicin treatment on cell wall protein levels[219]. Upregulation of peptidoglycan biosynthesis enzymes and ABC transporters in response to antibiotic exposure supported the ability of mycobacteria to establish a phenotypic response that allows for restructuring of the cell wall, with potential implications for virulence[219]. Of particular importance is the distinct lack of overlap in protein identification seen between proteomic studies, for which there are several contributing factors such as the methods of sample preparation, number of replicates carried out and bioinformatic analysis pipelines implemented[237]. Consequently, in spite of the numerous fractional proteomic studies performed in mycobacteria to identify proteins

associated with the cell wall, we are far from obtaining a defined set of proteins that are conclusively found within the mycobacterial cell envelope[237].

As we were working on a mycobacterial model that is assumed to possess a severely depleted cell wall, we set out to investigate the biochemical composition of these variants in comparison to their wall-replete counterparts. We employed the differential centrifugation method of sample preparation outlined by Hermann et al. to prepare separate protein fractions for the cell envelope, cytoplasm and debris of both cell wall-replete and CWD *Msm*, before performing tandem mass spectrometry for protein identification[219]. Functional annotation of proteins unique to each fraction presented a distinct absence of cell wall associated proteins in the spheroplast cell envelope and debris samples; of these, the loss of all proteins showing functional association with ABC transporters was of particular significance. The ABC transporter superfamily is comprised of integral membrane proteins that are essential for the import and export of many molecules, components of which make up 2.5% of the *Mtb* genome[238]. Of relevance to our proteomic analyses are the ABC transporter domains that extend into the periplasm, the loss of functional annotation of these domains in spheroplasts is indicative of cell wall loss and poses many questions regarding the survival of such variants without these crucial nutrient importers. We also observed a decrease in membrane-associated proteins and protein exporters in spheroplast samples, further validating prior microscopic observations of mycomembrane and peptidoglycan loss. A difficulty faced when allocating functional annotations to our protein lists using Gene Ontology was the paucity of information regarding cellular localization. As such, separating proteins predicted to sit within the plasma membrane from those that reside in subsequent envelope layers proved incredibly complex. Nevertheless, regarding proteins functionally annotated to be 'Integral to Membrane' as those occupying space somewhere within the cell envelope as a whole, we were able to observe a dramatic reduction in spheroplasts.

The relative abundance of proteins found in both wild-type and spheroplast samples for each fraction also yielded interesting results. The debris fraction of spheroplasts exhibited a significant reduction in abundance of Ag85A and Ag85C, members of the antigen 85 complex that are essential in the formation of mycomembrane components and some of the few enzymes known to sit within the lipid rich mycolic acid layer[32,33]. Several other proteins involved in ABC transporter systems and predicted to be periplasmic were also identified as significantly reduced in the cell envelope and debris fraction of cell wall deficient *Msm*. We were hesitant to draw conclusions regarding proteins that exhibited increased abundance in spheroplast fractions owing to their likely over-representation in these samples as a result of significant loss of biomass that resulted from removal of the cell wall. Indeed, many proteins in the cell

envelope and debris fractions that showed higher abundance in cell wall deficient samples were found to localize within the cytoplasm, making it unsurprising that these were lower in abundance in cell wall replete fractions that were likely to contain cell wall associated proteins.

Our analyses of both relative abundance and functional annotation yielded intriguing results when comparing the debris of each sample, as a surprising number of proteins were captured in this fraction. This led us to question the validity of differential centrifugation as a means of fractionation; however, in the development of this protocol, Hermann et al. made a similar observation, postulating that sonication would result in enrichment of cell wall and plasma membrane associated proteins in the debris[219]. Analysis of the properties of proteins found in the debris fraction led them to conclude that it is likely enriched for proteins that are smaller in size, exhibit decreased hydrophobicity and possess low isoelectric points[219]. Taking this into consideration, we determined the cell debris fraction to be of comparable importance to the cell envelope fraction when evaluating changes in protein composition between our samples. Application of fractional mass spectrometry to cell wall deficient mycobacteria is a promising technique that future work aims to combine with the biorthogonal tagging utilized in Chapter 3 to observe the abundance of tagged proteins in the different cellular compartments and compare these abundance profiles between cell wall replete and cell wall deficient organisms.

Conclusion

This study set out to characterize the extent of cell wall degradation in *Msm* incurred by treatment with lysozyme. Application of fluorescence microscopy coupled with quantitative image analysis provided novel insight into the loss of the peptidoglycan and mycolic acid layers through metabolic incorporation of D-alanine and trehalose analogues, respectively. These observations were validated through extensive proteomic profiling of spheroplast bacteria, showing substantial loss of cell wall associated proteins that had not been shown previously in *M. smegmatis*. These variants gave rise to numerous difficulties during experimentation due to their well-documented fragility and dependence on an osmoprotective medium to prevent lysis[105]. Despite these confounders, we were able to develop a reproducible method of spheroplast generation that allowed us to proceed with characterization assays. Previous efforts to illustrate the ability of mycobacteria to survive following treatment with cell wall degrading enzymes are outdated and used electron microscopy as the gold standard of confirming the absence of cell wall components[27,180]. We present here a more reliable means of characterization, applying modern techniques to tackle the definition of cell wall deficiency. With this characterization now established, future work aims to combine the bio-orthogonal techniques developed in Chapter 3 with

spheroplasting methods to better understand the impact of the mycobacterial cell wall on compound permeation.

Cell wall deficiency is increasingly being recognized as an under-appreciated mechanism utilized by bacteria that not only presents a possible role in pathogenesis but also provides a unique bacterial system for application in biotechnology[78,79,103,105]. CWD forms of *E. coli* and *Listeria monocytogenes* have been implicated in tolerance to antibiotics and recurrence of disease, emphasizing the potential for cell wall deficiency to present a novel form of persistence whereby shedding of cell wall components provides immunity in the face of cell wall targeting antibiotics[78,79]. Furthermore, the ability of these organisms to arise in the presence of lysozyme (a key factor involved in host immunity to TB,) combined with an apparent resilience in the face of cell wall targeting antibiotics and a potential to revert to a wall replete status after the removal of such antibiotics alludes to their prospective participation in resurgence of infection[79]. Considering the global burden of TB disease, representing the top cause of death by an infectious agent before the COVID-19 pandemic, characterization of mycobacterial spheroplasts and their potential role in antibiotic evasion and disease recalcitrance warrants further investigation[80].

SUPPLEMENTARY INFORMATION

Supplementary Table 1: https://figshare.com/s/98406fda72080626203c

Supplementary Information 1: https://figshare.com/s/b57e7330e4e9e599edd4

Supplementary Information 2: https://figshare.com/s/e107414d4046988ea673

Supplementary Information 3: https://figshare.com/s/5135e12ea433132d4146

Supplementary Movies 1-7: https://figshare.com/s/bdea81d4b2a25565e24d

REFERENCES

1. Djelouadji, Z., Raoult, D. & Drancourt, M. Palaeogenomics of Mycobacterium tuberculosis: Epidemic bursts with a degrading genome. *Lancet Infect. Dis.* **11**, 641–650 (2011).
2. Galagan, J. E. Genomic insights into tuberculosis. *Nat. Rev. Genet.* **15**, 307–20 (2014).
3. Behr, M. A. & Gagneux, S. The Rise and Fall of the Mycobacterium tuberculosis Complex. *Genet. Evol. Infect. Dis.* 651–667 (2011) doi:10.1016/B978-0-12-384890-1.00024-8.
4. Comas, I. *et al.* Out-of-Africa migration and Neolithic coexpansion of Mycobacterium tuberculosis with modern humans. *Nat. Genet.* **45**, 1176–1182 (2013).
5. Gagneux, S. Ecology and evolution of Mycobacterium tuberculosis. *Nat. Rev. Microbiol.* **16**, 1–12 (2018).
6. Boritsch, E. C. *et al.* A glimpse into the past and predictions for the future: The molecular evolution of the tuberculosis agent. *Mol. Microbiol.* **93**, 835–852 (2014).
7. Allué-Guardia, A., García, J. I. & Torrelles, J. B. Evolution of Drug-Resistant Mycobacterium tuberculosis Strains and Their Adaptation to the Human Lung Environment. *Front. Microbiol.* **12**, 1–21 (2021).
8. Allen, A. C. *et al.* Parallel in vivo experimental evolution reveals that increased stress resistance was key for the emergence of persistent tuberculosis bacilli. *Nat. Microbiol.* **6**, 1082–1093 (2021).
9. Brites, D. & Gagneux, S. Co-evolution of Mycobacterium tuberculosis and Homo sapiens. *Immunol. Rev.* **264**, 6–24 (2015).
10. Manina, G., Dhar, N. & McKinney, J. D. Stress and host immunity amplify mycobacterium tuberculosis phenotypic heterogeneity and induce nongrowing metabolically active forms. *Cell Host Microbe* **17**, 32–46 (2015).
11. Freschi, L. *et al.* Population structure, biogeography and transmissibility of Mycobacterium tuberculosis. *Nat. Commun.* **12**, 1–11 (2021).
12. Muller, B., Borrell, S., Rose, G. & Gagneux, S. The heterogeneous evolution of multidrug-resistant Mycobacterium tuberculosis. *Trends Genet.* **29**, 160–169 (2013).
13. Garcia-Vilanova, A., Chan, J. & Torrelles, J. B. Underestimated Manipulative Roles of Mycobacterium tuberculosis Cell Envelope Glycolipids During Infection. *Front. Immunol.* **10**, (2019).
14. Castro, R. A. D., Borrell, S. & Gagneux, S. The within-host evolution of antimicrobial resistance in Mycobacterium tuberculosis. *FEMS Microbiol. Rev.* **45**, 1–27 (2021).
15. Pai, M. *et al.* Tuberculosis. *Nat. Rev. Dis. Prim.* **2**, (2016).
16. Koch, A. L. Were Gram-positive rods the first bacteria? *Trends Microbiol.* **11**, 166–170 (2003).
17. Koch, A. L. Development and diversification of the Last Universal Ancestor. *Journal of Theoretical Biology* vol. 168 269–280 (1994).
18. Beveridge, T. J. Use of the Gram stain in microbiology Use of the Gram stain in microbiology. *Biotech. Histochem.* **76**, 111–118 (2001).
19. Tocheva, E. I., Ortega, D. R. & Jensen, G. J. Sporulation, bacterial cell envelopes and the origin of life. *Nat. Rev. Microbiol.* **14**, 535–542 (2016).

20. Léonard, R. R. *et al.* Was the Last Bacterial Common Ancestor a Monoderm after All? *Genes (Basel).* **13**, (2022).
21. Skophammer, R. G., Servin, J. A., Herbold, C. W. & Lake, J. A. Evidence for a Gram-positive, eubacterial root of the tree of life. *Mol. Biol. Evol.* **24**, 1761–1768 (2007).
22. Gupta, R. S. Origin of diderm (Gram-negative) bacteria: Antibiotic selection pressure rather than endosymbiosis likely led to the evolution of bacterial cells with two membranes. *Antonie van Leeuwenhoek, Int. J. Gen. Mol. Microbiol.* **100**, 171–182 (2011).
23. Trachtenberg, S. Mollicutes - Wall-less bacteria with internal cytoskeletons. *J. Struct. Biol.* **124**, 244–256 (1998).
24. Rivera-Tapia, J. A., Cedillo-Ramírez, M. L. & Gil Juárez, C. Some biological features of Mollicutes. *Rev. Latinoam. Microbiol.* **44**, 53–57 (2002).
25. Waites, K. B. & Talkington, D. F. Mycoplasma pneumoniae. *Clin. Microbiol. Rev.* **17**, 697–728 (2004).
26. Klieneberger, E. The Natural Occurrence of Pleuropneumonia-like Organisms in Apparent Symbiosis With Streptobacillus moniliformis and Other Bacteria. *J. Pathol. Bacteriol.* **40**, 93–105 (1935).
27. Mattman, L. H. *Cell Wall Deficient Forms: Stealth Pathogens*. (2000).
28. Elliott, S. P. Rat bite fever and Streptobacillus moniliformis. *Clin. Microbiol. Rev.* **20**, 13–22 (2007).
29. Ratnam, S. & Chandrasekhar, S. The Pathogenicity of Spheroplasts of Mycobacterium tuberculosis. *Am. Rev. Respir. Dis.* **114**, 549–554 (1976).
30. Klieneberger-Nobel, E. Origin, development and significance of L-forms in bacterial cultures. *J. Gen. Microbiol.* **3**, 434–443 (1949).
31. Klieneberger-Nobel, E. On streptobacillus moniliformis and the filtrability of its L-form. *J. Hyg. (Lond).* **47**, 393–395 (1949).
32. Rodriguez-Rivera, F. P., Zhou, X., Theriot, J. A. & Bertozzi, C. R. Visualization of mycobacterial membrane dynamics in live cells. *J. Am. Chem. Soc.* **139**, 3488–3495 (2017).
33. Dulberger, C. L., Rubin, E. J. & Boutte, C. C. The mycobacterial cell envelope — a moving target. *Nat. Rev. Microbiol.* **18**, 47–59 (2020).
34. Jarlier, V. & Nikaido, H. Permeability barrier to hydrophilic solutes in Mycobacterium chelonei. *J. Bacteriol.* **172**, 1418–1423 (1990).
35. Xu, W. X. *et al.* The Wag31 protein interacts with AccA3 and coordinates cell wall lipid permeability and lipophilic drug resistance in Mycobacterium smegmatis. *Biochem. Biophys. Res. Commun.* **448**, 255–260 (2014).
36. Liu, J., Barry, C. E., Besra, G. S. & Nikaido, H. Mycolic acid structure determines the fluidity of the mycobacterial cell wall. *J. Biol. Chem.* **271**, 29545–29551 (1996).
37. Daffé, M. The cell envelope of tubercle bacilli. *Tuberculosis* **95**, S155–S158 (2015).
38. Jankute, M., Cox, J. A. G., Harrison, J. & Besra, G. S. Assembly of the Mycobacterial Cell Wall. *Annu. Rev. Microbiol.* **69**, 405–23 (2015).
39. Daffé, M. & Marrakchi, H. Unraveling the Structure of the Mycobacterial Envelope. *Microbiol. Spectr.* **7**,

1087–1095 (2019).

40. Leeson, P. Drug discovery: Chemical beauty contest. *Nature* **481**, 455–456 (2012).
41. Lipinski, C. A., Lombardo, F., Dominy, B. W. & Feeney, P. J. Experimental and computational approaches to estimate solubility and permeability in drug discovery and development settings. *Adv. Drug Deliv. Rev.* **23**, 3–25 (1996).
42. Bickerton, G. R., Paolini, G. V, Besnard, J., Muresan, S. & Hopkins, A. L. Quantifying the chemical beauty of drugs. *Nat. Chem.* **4**, 90–98 (2012).
43. Mannhold, E. R., Kubinyi, H., Folkers, G. & Cruciani, G. *Molecular Drug Properties*. *Metabolism Clinical And Experimental* (2008).
44. Janardhan, S., Ram Vivek, M. & Narahari Sastry, G. Modeling the permeability of drug-like molecules through the cell wall of Mycobacterium tuberculosis: an analogue based approach. *Mol. BioSyst.* **12**, 3377–3384 (2016).
45. Dartois, V. The path of anti-tuberculosis drugs: from blood to lesions to mycobacterial cells. *Nat. Rev. Microbiol.* **12**, 159–67 (2014).
46. Chiaradia, L. *et al.* Dissecting the mycobacterial cell envelope and defining the composition of the native mycomembrane. *Sci. Rep.* **7**, 1–12 (2017).
47. Bailo, R., Bhatt, A. & Aínsa, J. A. Lipid transport in Mycobacterium tuberculosis and its implications in virulence and drug development. *Biochem. Pharmacol.* **96**, 159–167 (2015).
48. Black, P. A. *et al.* Energy metabolism and drug efflux in mycobacterium tuberculosis. *Antimicrob. Agents Chemother.* **58**, 2491–2503 (2014).
49. Rossi, E. De, Ainsa, J. A. & Riccardi, G. Role of mycobacterial efflux transporters in drug resistance: An unresolved question. *FEMS Microbiol. Rev.* **30**, 36–52 (2006).
50. Li, X. Z. & Nikaido, H. Efflux-Mediated Drug Resistance in Bacteria. *Drugs* **64**, 159–204 (2004).
51. Laws, M., Jin, P. & Rahman, K. M. Efflux pumps in Mycobacterium tuberculosis and their inhibition to tackle antimicrobial resistance. *Trends Microbiol.* **30**, 57–68 (2022).
52. Hartkoorn, R. C., Uplekar, S. & Cole, S. T. Cross-resistance between clofazimine and bedaquiline through upregulation of mmpl5 in mycobacterium tuberculosis. *Antimicrob. Agents Chemother.* **58**, 2979–2981 (2014).
53. Xu, Z., Meshcheryakov, V. A., Poce, G. & Chng, S. MmpL3 is the flippase for mycolic acids in mycobacteria. *Proc. Natl. Acad. Sci.* 1–6 (2017) doi:10.1073/pnas.1700062114.
54. Zumla, A., Nahid, P. & Cole, S. T. Advances in the development of new tuberculosis drugs and treatment regimens. *Nat. Rev. Drug Discov.* **12**, 388–404 (2013).
55. Sacchettini, J. C., Rubin, E. J. & Freundlich, J. S. Drugs versus bugs: in pursuit of the persistent predator Mycobacterium tuberculosis. *Nat. Rev. Microbiol.* **6**, 41–52 (2008).
56. Rattan, A., Kalia, A. & Ahmad, N. Multidrug-resistant Mycobacterium tuberculosis: Molecular perspectives. *Emerg. Infect. Dis.* **4**, 195–209 (1998).
57. Arbex, M. A., Varella, M. D. C. L., Siqueira, H. R. De & Mello, F. A. F. De. Antituberculosis drugs: Drug

interactions, adverse effects, and use in special situations. Part 1: First-line drugs. *J Bras Pneumol.* **36**, 626–640 (2010).

58. Hannebelle, M. T. M. *et al.* A biphasic growth model for cell pole elongation in mycobacteria. *Nat. Commun.* **11**, (2020).
59. Maisonneuve, E. & Gerdes, K. Molecular mechanisms underlying bacterial persisters. *Cell* **157**, 539–548 (2014).
60. Lennon, J. T. & Jones, S. E. Microbial seed banks: the ecological and evolutionary implications of dormancy. *Nat. Rev. Microbiol.* **9**, 119–130 (2011).
61. Ayrapetyan, M., Williams, T. C. & Oliver, J. D. Bridging the gap between viable but non-culturable and antibiotic persistent bacteria. *Trends Microbiol.* **23**, 7–13 (2015).
62. Brauner, A., Fridman, O., Gefen, O. & Balaban, N. Q. Distinguishing between resistance, tolerance and persistence to antibiotic treatment. *Nat. Rev. Microbiol.* **14**, 320–30 (2016).
63. Bigger, J. W. The Bactericidal Action of Penicillin on Staphylococcus Pyogenes. *Ir. J. Med. Sci.* (1944).
64. Balaban, N. Q., Merrin, J., Chait, R., Kowalik, L. & Leibler, S. Bacterial Persistence as a Phenotypic Switch. *Science (80-.).* **305**, 1622–1625 (2004).
65. Dörr, T. Understanding tolerance to cell wall–active antibiotics. *Ann. N. Y. Acad. Sci.* **1496**, 35–58 (2021).
66. Balaban, N. Q. *et al.* Definitions and guidelines for research on antibiotic persistence. *Nat. Rev. Microbiol.* **17**, 441–448 (2019).
67. Levin-Reisman, I. *et al.* Antibiotic tolerance facilitates the evolution of resistance. *Science (80-.).* **355**, 826–830 (2017).
68. Bergkessel, M., Basta, D. W. & Newman, D. K. The physiology of growth arrest: uniting molecular and environmental microbiology. *Nat Rev Micro* **14**, 549–562 (2016).
69. Hameed, S. & Fatima, Z. *Pathogenicity and Drug Resistance of Human Pathogens. Pathogenicity and Drug Resistance of Human Pathogens* (2019). doi:10.1007/978-981-32-9449-3.
70. Ehrt, S., Schnappinger, D. & Rhee, K. Y. Metabolic principles of persistence and pathogenicity in Mycobacterium tuberculosis. *Nat. Rev. Microbiol.* 1–12 (2018) doi:10.1038/s41579-018-0013-4.
71. Rittershaus, E. S. C., Baek, S. H. & Sassetti, C. M. The normalcy of dormancy: Common themes in microbial quiescence. *Cell Host Microbe* **13**, 643–651 (2013).
72. Chung, E. S., Johnson, W. C. & Aldridge, B. B. Types and functions of heterogeneity in mycobacteria. *Nat. Rev. Microbiol.* **0123456789**, (2022).
73. Cunningham, A. F. & Spreadbury, C. L. Mycobacterial stationary phase induced by low oxygen tension: Cell wall thickening and localization of the 16-kilodalton α-crystallin homolog. *J. Bacteriol.* **180**, 801–808 (1998).
74. Sarathy, J., Dartois, V., Dick, T. & Gengenbacher, M. Reduced drug uptake in phenotypically resistant nutrient-starved nonreplicating Mycobacterium tuberculosis. *Antimicrob. Agents Chemother.* **57**, 1648–1653 (2013).

75. Fang, X., Wallqvist, A. & Reifman, J. Modeling Phenotypic Metabolic Adaptations of Mycobacterium tuberculosis H37Rv under Hypoxia. *PLoS Comput. Biol.* **8**, (2012).
76. Petrovic Fabijan, A. *et al.* L-form switching confers antibiotic, phage and stress tolerance in pathogenic Escherichia coli. *bioRxiv* 2021.06.21.449206 (2021).
77. Slavchev, G., Michailova, L. & Markova, N. L-form transformation phenomenon in Mycobacterium tuberculosis associated with drug tolerance to ethambutol. *Int. J. Mycobacteriology* **5**, 454–459 (2016).
78. Grosboillot, V., Keller, I., Ernst, C., Loessner, M. J. & Schuppler, M. Ampicillin Treatment of Intracellular Listeria monocytogenes Triggers Formation of Persistent , Drug- Resistant L-Form Cells. **12**, 1–12 (2022).
79. Mickiewicz, K. M. *et al.* Possible role of L-form switching in recurrent urinary tract infection. *Nat. Commun.* 1–9 (2019) doi:10.1038/s41467-019-12359-3.
80. World Health Organization. *Global Tuberculosis Report 2021*. *World Health Organization* vol. 59 (2021).
81. Tiberi, S. *et al.* Accelerating development of new shorter TB treatment regimens in anticipation of a resurgence of multi-drug resistant TB due to the COVID-19 pandemic. *Int. J. Infect. Dis.* **113**, S96–S99 (2021).
82. Lechartier, B., Rybniker, J., Zumla, A. & Cole, S. T. Tuberculosis drug discovery in the post- post-genomic era. *EMBO Mol. Med.* 1–11 (2014).
83. Black, T. A. & Buchwald, U. K. The pipeline of new molecules and regimens against drug-resistant tuberculosis. *J. Clin. Tuberc. Other Mycobact. Dis.* **25**, 100285 (2021).
84. Yuan, T. & Sampson, N. S. Hit Generation in TB Drug Discovery : From Genome to Granuloma. *Chem. Rev.* **118**, 1887–1916 (2018).
85. Mdluli, K., Kaneko, T. & Upton, A. The Tuberculosis Drug Discovery and Development Pipeline and Emerging Drug Targets. *Cold Spring Harb. Perspect. Med.* **5**, 1–24 (2015).
86. Evans, J. C. & Mizrahi, V. Priming the tuberculosis drug pipeline : new antimycobacterial targets and agents. *Curr. Opin. Microbiol.* **45**, 39–46 (2018).
87. Koul, A., Arnoult, E., Lounis, N., Guillemont, J. & Andries, K. The challenge of new drug discovery for tuberculosis. *Nature* **469**, 483–490 (2011).
88. Wiegand, I., Hilpert, K. & Hancock, R. E. W. Agar and broth dilution methods to determine the minimal inhibitory concentration (MIC) of antimicrobial substances. *Nat. Protoc.* **3**, 163–175 (2008).
89. Dartois, V. & Barry, C. E. A medicinal chemists' guide to the unique difficulties of lead optimization for tuberculosis. *Bioorg. Med. Chem. Lett.* **23**, 4741–4750 (2013).
90. Kocaoglu, O. & Carlson, E. E. Progress and prospects for small-molecule probes of bacterial imaging. *Nat. Chem. Biol.* **12**, 472–478 (2016).
91. Huang, Y., Chen, W., Chung, J., Yin, J. & Yoon, J. Recent progress in fluorescent probes for bacteria. *Chem. Soc. Rev.* **50**, 7725–7744 (2021).
92. Best, M. D. Click chemistry and bioorthogonal reactions: Unprecedented selectivity in the labeling of biological molecules. *Biochemistry* **48**, 6571–6584 (2009).

93. Tyler, D. S. *et al.* Click chemistry enables preclinical evaluation of targeted epigenetic therapies. *Science (80-.).* **4**, 1397–1401 (2017).
94. Baskin, J. M. *et al.* Copper-free click chemistry for dynamic in vivo imaging. *Proc. Natl. Acad. Sci. U. S. A.* **104**, 16793–7 (2007).
95. Hatzenpichler, R. *et al.* In situ visualization of newly synthesized proteins in environmental microbes using amino acid tagging and click chemistry. *Environ. Microbiol.* **16**, 2568–2590 (2014).
96. Burke, C. *et al.* Harnessing Single Cell Sorting to Identify Cell Division Genes and Regulators in Bacteria. *PLoS One* **8**, (2013).
97. Khara, J. S. *et al.* Ultra-Short Antimicrobial Peptoids Show Propensity for Membrane Activity Against Multi-Drug Resistant Mycobacterium tuberculosis. *Front. Microbiol.* **11**, 1–11 (2020).
98. Elitas, M., Dhar, N. & McKinney, J. D. Revealing antibiotic tolerance of the mycobacterium smegmatis xanthine/uracil permease mutant using microfluidics and single-cell analysis. *Antibiotics* **10**, (2021).
99. Parish, T. In vitro drug discovery models for Mycobacterium tuberculosis relevant for host infection. *Expert Opin. Drug Discov.* **15**, 349–358 (2020).
100. Darby, C. M. *et al.* Whole Cell Screen for Inhibitors of pH Homeostasis in Mycobacterium tuberculosis. *PLoS One* **8**, (2013).
101. Nagamani, S. & Sastry, G. N. Mycobacterium tuberculosis cell wall permeability model generation using chemoinformatics and machine learning approaches. *ACS Omega* **6**, 17472–17482 (2021).
102. Merget, B., Zilian, D., Müller, T. & Sotriffer, C. A. MycPermCheck: The Mycobacterium tuberculosis permeability prediction tool for small molecules. *Bioinformatics* **29**, 62–68 (2013).
103. Kilcher, S., Studer, P., Muessner, C., Klumpp, J. & Loessner, M. J. Cross-genus rebooting of custom-made, synthetic bacteriophage genomes in L-form bacteria. *Proc. Natl. Acad. Sci.* **115**, 1–6 (2018).
104. Melzer, E. S., Sein, C. E., Chambers, J. J. & Sloan Siegrist, M. DivIVA concentrates mycobacterial cell envelope assembly for initiation and stabilization of polar growth. *Cytoskeleton* **75**, 498–507 (2018).
105. Allan, E. J., Hoischen, C. & Gumpert, J. *Bacterial L-Forms*. *Advances in Applied Microbiology* vol. 68 (Elsevier Inc., 2009).
106. Snapper, S. B., Melton, R. E., Mustafa, S., Kieser, T. & Jr, W. R. J. Isolation and characterization of efficient plasmid transformation mutants of Mycobacterium smegmatis. *Mol. Microbiol.* **4**, 1911–1919 (1990).
107. Santi, I. & McKinney, J. D. Chromosome organization and replisome dynamics in Mycobacterium smegmatis. *MBio* **6**, (2015).
108. Lee, S., Choi, M., Kim, P. & Myung, P. K. 3D-QSAR and Cell Wall Permeability of Antitubercular Nitroimidazoles against Mycobacterium tuberculosis. 13870–13885 (2013) doi:10.3390/molecules181113870.
109. McGenity, T. J., Timmis, K. N. & Nogales, B. *Hydrocarbon and Lipid Microbiology Protocols*. (2017). doi:10.1007/978-3-662-52793-1.
110. Corporation, E. M. CellASIC ® ONIX B04A-03 Microfluidic Bacteria Plate. *Merck, Millipore User Guide* 1–

5 (2007).

111. Row, R. D. & Prescher, J. A. Constructing New Bioorthogonal Reagents and Reactions. *Acc. Chem. Res.* acs.accounts.7b00606 (2018) doi:10.1021/acs.accounts.7b00606.

112. Sletten, E. M. & Bertozzi, C. R. Bioorthogonal Reactions. (2011).

113. Cserép, G. B., Herner, A. & Kele, P. Bioorthogonal fluorescent labels: a review on combined forces. *Methods Appl. Fluoresc.* **3**, 042001 (2015).

114. Shieh, P., Siegrist, M. S., Cullen, A. J. & Bertozzi, C. R. Imaging bacterial peptidoglycan with near-infrared fluorogenic azide probes. **111**, (2014).

115. Kolb, H. C., Finn, M. G. & Sharpless, K. B. Click Chemistry : Diverse Chemical Function from a Few Good Reactions. *Angew. Chemie - Int. Ed.* **40**, 2004–2021 (2001).

116. Hein, C. D., Liu, X.-M. & Wang, D. Click chemistry, a powerful tool for pharmaceutical sciences. *Pharm. Res.* **25**, 2216–30 (2008).

117. Kolb, H. C. & Sharpless, K. B. The growing impact of click chemistry on drug discovery. *Drug Discov. Today* **8**, 1128–1137 (2003).

118. Moses, J. E. & Moorhouse, A. D. The growing applications of click chemistry. *Chem. Soc. Rev.* **36**, 1249–1262 (2007).

119. Rostovtsev, V. V., Green, L. G., Fokin, V. V. & Sharpless, K. B. A stepwise huisgen cycloaddition process: Copper(I)-catalyzed regioselective 'ligation' of azides and terminal alkynes. *Angew. Chemie - Int. Ed.* **41**, 2596–2599 (2002).

120. Soriano Del Amo, D. *et al.* Biocompatible copper(I) catalysts for in vivo imaging of glycans. *J. Am. Chem. Soc.* **132**, 16893–16899 (2010).

121. Agard, N. J., Prescher, J. A. & Bertozzi, C. R. A strain-promoted [3 + 2] azide-alkyne cycloaddition for covalent modification of biomolecules in living systems. *J. Am. Chem. Soc.* **126**, 15046–15047 (2004).

122. Friscourt, F., Fahrni, C. J. & Boons, G.-J. Fluorogenic Strain-Promoted Alkyne-Diazo Cycloadditions. *Chemistry (Easton).* **40**, 1–15 (2015).

123. Jewett, J. C. & Bertozzi, C. R. Synthesis of a Fluorogenic Cyclooctyne Activated by Cu-Free Click Chemistry. *ACS Org. Lett.* **13**, 5937–5939 (2011).

124. Friscourt, F., Fahrni, C. J. & Boons, G. A Fluorogenic Probe for the Catalyst-Free Detection of Azide-Tagged Molecules. *J. Am. Chem. Soc.* **134**, 18809–18815 (2012).

125. Dommerholt, J. & Rutjes, F. P. J. T. Strain-Promoted 1,3-Dipolar Cycloaddition of Cycloalkynes and Organic Azides. *Top. Curr. Chem.* **374**, 1–20 (2016).

126. Shie, J. J., Liu, Y. C., Hsiao, J. C., Fang, J. M. & Wong, C. H. A cell-permeable and triazole-forming fluorescent probe for glycoconjugate imaging in live cells. *Chem. Commun.* **53**, 1490–1493 (2017).

127. Agarwal, P., Beahm, B. J., Shieh, P. & Bertozzi, C. R. Systemic Fluorescence Imaging of Zebrafish Glycans with Bioorthogonal Chemistry. *Angew. Chemie - Int. Ed.* **127**, 11666–11672 (2015).

128. Hatzenpichler, R. *et al.* Visualizing in situ translational activity for identifying and sorting slow-growing archaeal−bacterial consortia. *Proc. Natl. Acad. Sci.* **113**, E4069–E4078 (2016).

129. Dieterich, D. C., Link, A. J., Graumann, J., Tirrell, D. A. & Schuman, E. M. Selective identification of newly synthesized proteins in mammalian cells using bioorthogonal noncanonical amino acid tagging (BONCAT). *Proc. Natl. Acad. Sci. U. S. A.* **103**, 9482–7 (2006).
130. Lang, K. & Chin, J. W. Cellular incorporation of unnatural amino acids and bioorthogonal Labeling of Proteins. *Chem. Rev.* **114**, 4764–4806 (2014).
131. Iwasaki, S. & Ingolia, N. T. The Growing Toolbox for Protein Synthesis Studies. *Trends Biochem. Sci.* **42**, 612–624 (2017).
132. Hinz, F. I., Dietrich, D. C., Tirrell, D. A. & Schuman, E. M. Noncanonical Amino Acid\nLabeling in Vivo to Visualize\nand Affinity Purify Newly Synthesized Proteins in Larval Zebrafish. *ACS Chem. Neurosci.* **3**, 40 (2012).
133. Siegrist, M. S. *et al.* D-amino acid chemical reporters reveal peptidoglycan dynamics of an intracellular pathogen. *ACS Chem. Biol.* **8**, 500–505 (2013).
134. Berney, M. *et al.* Essential roles of methionine and S-adenosylmethionine in the autarkic lifestyle of Mycobacterium tuberculosis. *Proc. Natl. Acad. Sci. U. S. A.* **112**, 10008–13 (2015).
135. Battle, A. *et al.* Impact of regulatory variation from RNA to protein. *Science (80-.).* **347**, 664–667 (2014).
136. Sadler, N. C. & Wright, A. T. Activity-based protein profiling of microbes. *Curr. Opin. Chem. Biol.* **24**, 139–144 (2015).
137. Kokate, A., Li, X. & Jasti, B. Effect of drug lipophilicity and ionization on permeability across the buccal mucosa: A technical note. *AAPS PharmSciTech* **9**, 501–504 (2008).
138. Xing, L. & Glen, R. C. Novel methods for the prediction of logP, Pka, and logD. *J. Chem. Inf. Comput. Sci.* **42**, 796–805 (2002).
139. Giulia, C. & Giuseppe, E. Molecular descriptors for polarity: the need of going beyond polar surface area. *Future Med. Chem.* **8**, (2016).
140. Österberg, T. & Norinder, U. Prediction of Polar Surface Area and Drug Transport Processes Using Simple Parameters and PLS Statistics. *J. Chem. Inf. Comput. Sci.* **40**, 1408–1411 (2000).
141. Feher, M. & Schmidt, J. M. Property distributions: Differences between drugs, natural products, and molecules from combinatorial chemistry. *J. Chem. Inf. Comput. Sci.* **43**, 218–227 (2003).
142. Santos, G. B., Ganesan, A. & Emery, F. S. Oral Administration of Peptide-Based Drugs: Beyond Lipinski's Rule. *ChemMedChem* **11**, 2245–2251 (2016).
143. Bryant, M. J. *et al.* The CSD Drug Subset: The Changing Chemistry and Crystallography of Small Molecule Pharmaceuticals. *J. Pharm. Sci.* **108**, 1655–1662 (2019).
144. Meade, A. D. *et al.* Studies of chemical fixation effects in human cell lines using Raman microspectroscopy. *Anal. Bioanal. Chem.* **396**, 1781–1791 (2010).
145. Chao, Y. & Zhang, T. Optimization of fixation methods for observation of bacterial cell morphology and surface ultrastructures by atomic force microscopy. *Appl. Microbiol. Biotechnol.* **92**, 381–392 (2011).
146. Lambert, P. a. Cellular impermeability and uptake of biocides and antibiotics in gram-positive bacteria and mycobacteria. *J Appl Microbiol* **92**, 46S-54S (2002).

147. Meghani, N. M., Amin, H. H. & Lee, B. Mechanistic applications of click chemistry for pharmaceutical drug discovery and drug delivery. *Drug Discov. Today* **22**, 1604–1619 (2017).
148. Soliman, K., Grimm, F., Wurm, C. A. & Egner, A. Predicting the membrane permeability of organic fluorescent probes by the deep neural network based lipophilicity descriptor DeepFl-LogP. *Sci. Rep.* **11**, 1–9 (2021).
149. Pajouhesh, H. & Lenz, G. R. Medicinal Chemical Properties of Successful Central Nervous System Drugs. **2**, 541–553 (2005).
150. Benedetto Tiz, D., Kikelj, D. & Zidar, N. Overcoming problems of poor drug penetration into bacteria: challenges and strategies for medicinal chemists. *Expert Opin. Drug Discov.* **13**, 497–507 (2018).
151. Modak, B., Girkar, S., Narayan, R. & Kapoor, S. Mycobacterial Membranes as Actionable Targets for Lipid-Centric Therapy in Tuberculosis. *J. Med. Chem.* **65**, 3046–3065 (2022).
152. Cimino, M., Alamo, L. & Salazar, L. Permeabilization of the mycobacterial envelope for protein cytolocalization studies by immunofluorescence microscopy. *BMC Microbiol.* **6**, 35 (2006).
153. Rocha, R., Almeida, C. & Azevedo, N. F. nfluence of the fixation/permeabilization step on peptide nucleic acid fluorescence in situ hybridization (PNA-FISH) for the detection of bacteria. *PLoS One* **13**, 1–13 (2018).
154. Whang, I. *et al.* Characterization and expression analysis of a goose-type lysozyme from the rock bream Oplegnathus fasciatus, and antimicrobial activity of its recombinant protein. *Fish Shellfish Immunol.* **30**, 532–542 (2011).
155. Kawai, Y. *et al.* Lysozyme Counteracts b -Lactam Antibiotics by Promoting the Emergence of L-Form Bacteria Article Lysozyme Counteracts b -Lactam Antibiotics by Promoting the Emergence of L-Form Bacteria. *Cell* 1–12 (2018) doi:10.1016/j.cell.2018.01.021.
156. Uhia, I., Williams, K. J., Shahrezaei, V. & Robertson, B. D. Mycobacterial Growth. *Cold Spring Harb. Perspect. Med.* 1–14 (2015).
157. Stone, M. R. L., Butler, M. S., Phetsang, W., Cooper, M. A. & Blaskovich, M. A. T. Fluorescent Antibiotics : New Research Tools to Fight Antibiotic Resistance. *Trends Biotechnol.* 1–14 (2018) doi:10.1016/j.tibtech.2018.01.004.
158. Tiyanont, K. *et al.* Imaging peptidoglycan biosynthesis in Bacillus subtilis with fluorescent antibiotics. *Proc. Natl. Acad. Sci.* **103**, 11033–11038 (2006).
159. Daniel, R. A. & Errington, J. Control of Cell Morphogenesis in Bacteria : Two Distinct Ways to Make a Rod-Shaped Cell. *Cell* **113**, 767–776 (2003).
160. Phetsang, W. *et al.* An azido-oxazolidinone antibiotic for live bacterial cell imaging and generation of antibiotic variants. *Bioorg. Med. Chem.* **22**, 4490–4498 (2014).
161. Phetsang, W. *et al.* Fluorescent Trimethoprim Conjugate Probes To Assess Drug Accumulation in Wild Type and Mutant Escherichia coli. *ACS Infect. Dis.* **2**, 688–701 (2016).
162. Lavecchia, A. & Giovanni, C. Di. Virtual Screening Strategies in Drug Discovery : A Critical Review. 2839–2860 (2013).

163. Metchnikoff, E. Ueber die phagocytare Rolle der Tuberkelriesenzellen. *Arch. Pathol. Lab. Med.* **113**, 63–94 (1888).
164. Edward, D. G. & Freundt, E. a. The classification and nomenclature of organisms of the pleuropneumonia group. *J. Gen. Microbiol.* **14**, 197–207 (1956).
165. Dienes, L. & Edsall, G. Observations on the L-organism of Klieneberger. *Exp. Biol. Med.* **36**, 740–744 (1937).
166. Barile, M. F., Graykowski, E. A., Driscoll, E. J. & Riggs, D. B. L Form of Bacteria Isolated from Recurrent Aphthous Stomatitis Lesions. *Oral Surg. Oral Med. Oral Pathol. Oral Radiol.* **16**, 1395–1402 (1963).
167. Burnham, W. R., Lennard-Jones, J. E., Stanford, J. L. & Bird, R. G. Mycobacteria as a possible cause of inflammatory bowel disease. *Lancet* 693–696 (1978).
168. Weibull, C. Chemical analysis elucidating the structure of bacterial L forms. *Acta Pathol. Microbiol. Scand.* **42**, 324–332 (1958).
169. Cohen, M. & Panos, C. Membrane Composition of Streptococcus pyogenes and Derived L Form. *Biochemistry* **5**, 2385–2392 (1966).
170. Kawai, Y. *et al.* Cell Growth of Wall-Free L-Form Bacteria Is Limited by Oxidative Damage. *Curr. Biol.* **25**, 1613–1618 (2015).
171. Kilcher, S., Studer, P., Muessner, C., Klumpp, J. & Loessner, M. J. Supporting Information - Cross-genus rebooting of custom-made, synthetic bacteriophage genomes in L-form bacteria. *Proc. Natl. Acad. Sci.* **115**, (2018).
172. Sharp, J. T., Hijans, W. & Dienes, L. Examination of the L Forms of Group A Streptococci for the Group-Specific Polysaccharide and M Protein. *J. Exp. Med.* **105**, 153–159 (1957).
173. Jekkel, A., Csajagi, E., Ilkoy, E. & Ambrus, G. Genetic Recombination by Spheroplast Fusion of Sterol-transforming Mycobacterium Strains. *Microbiology* **135**, 1727–1733 (1989).
174. Preac Mursic, V. *et al.* Formation and cultivation of Borrelia burgdorferi spheroplast-L-form variants. *Infection* **24**, 218–226 (1996).
175. Gumpert, J. & Taubeneck, U. Characteristic properties and biological significance of stable protoplast type L-forms. *Protoplasts 1983* **46**, 227–241 (1983).
176. Dienes, L. The isolation of L type cultures from the bacteroides with the aid of penicillin and their reversion into the usual bacilli. *J. Bacteriol.* **56**, 445–456 (1948).
177. Pierce, C. H. Proceedings of the Local Branches of the Society of American Bacteriologists. *J. Bacteriol.* **43**, 780 (1942).
178. Weibull, C. The isolation of protoplasts from Bacillus megaterium by controlled treatment with lysozyme. *J. Bacteriol.* **66**, 688–695 (1953).
179. Thacore, H. & Willett, H. P. Formation of Spheroplasts of Mycobacterium tuberculosis by Lysozyme Treatment. *Exp. Biol. Med.* **114**, 43–47 (1963).
180. Udou, T., Ogawa, M. & Mizuguchi, Y. An improved method for the preparation of mycobacterial spheroplasts and the mechanism involved in the reversion to bacillary form: electron microscopic and

physiological study. *Can. J. Microbiol.* **29**, 60–8 (1983).

181. Mercier, R., Kawai, Y. & Errington, J. General principles for the formation and proliferation of a wall-free (L-form) state in bacteria. *Elife* **3**, 1–14 (2014).
182. Huber, T. W. & Brinkley, A. W. Growth of Cell Wall-Defective Variants of Escherichia coli : Comparison of Aerobic and Anaerobic Induction Frequencies. *J. Clin. Microbiol.* **6**, 166–171 (1977).
183. Kawai, Y., Mercier, R., Mickiewicz, K., Serafini, A. & De, L. P. S. Crucial role for central carbon metabolism in the bacterial L-form switch and killing by β -lactam antibiotics. *Nat. Microbiol.* (2019) doi:10.1038/s41564-019-0497-3.
184. Bourgeois, L. & Beaman, B. L. Probable L-forms of Nocardia asteroides induced in cultured mouse peritoneal macrophages. *Infect. Immun.* **9**, 576–590 (1974).
185. Onwuamaegbu, M. E., Belcher, R. A. & Soare, C. Cell wall-deficient bacteria as a cause of infections: A review of the clinical significance. *J. Int. Med. Res.* **33**, 1–20 (2005).
186. Domingue, G. J., Woody, H. B., Farris, K. B. & Schlegel, J. U. Bacterial Variants in Urinary Casts and Renal Epithelial Cells. *Arch. Intern. Med.* **139**, 1355–1360 (1979).
187. Domingue, G. J., Thomas, R., Walters, F., Serrano, A. & Heidger, P. M. Cell wall deficient bacteria as a cause of idiopathic hematuria. *J. Urol.* **150**, 483–485 (1993).
188. Domingue, G. J. & Woody, H. B. Bacterial persistence and expression of disease. *Clin. Microbiol. Rev.* **10**, 320–344 (1997).
189. Gutman, L. T., Turck, M., Petersdorf, R. G. & Wedgwood, R. J. Significance of bacterial variants in urine of patients with chronic bacteriuria. *J. Clin. Invest.* **44**, 1945–1952 (1965).
190. Demonty, J. Experimental Escherichia coli pyelonephritis: Formation of spheroplasts in the kidney of the untreated rat. *Antonie Van Leeuwenhoek* **36**, 273–284 (1970).
191. Eastridge, R. R. & Farrar, W. E. L-Form Infection of the Rat Kidney: Effect of Water Diuresis. *Exp. Biol. Med.* **128**, 1193–1196 (1968).
192. Gnarpe, H. & Edebo, L. Conditions affecting the viability of spheroplasts in urine. *Infect. Immun.* **1**, 300–304 (1970).
193. Watanakunakorn, C. & Hamburger, A. M. Induction of Spheroplasts of Pseudomonas aeruginosa by Carbenicillin. *Appl. Microbiol.* **17**, 935–937 (1969).
194. Beran, V., Havelkova, M., Kaustova, J., Dvorska, L. & Pavlik, I. Cell wall deficient forms of mycobacteria : a review. *Vet. Med. (Praha).* **51**, 365–389 (2006).
195. Errington, J., Mickiewicz, K., Kawai, Y. & Wu, L. J. L-form bacteria, chronic diseases and the origins of life. *Philos. Trans.* **371**, 1–8 (2016).
196. Naser, S. A., Ghobrial, G., Romero, C. & Valentine, J. F. Culture of Mycobacterium avium subspecies paratuberculosis from the blood of patients with Crohn's disease. *Lancet* **364**, 1039–1044 (2004).
197. Chiodini, R. J., Van Kruiningen, H. J., Thayer, W. R. & Coutu, J. A. Spheroplastic phase of mycobacteria isolated from patients with Crohn's disease. *J. Clin. Microbiol.* **24**, 357–363 (1986).
198. Little, B. P. Sarcoidosis: overview of pulmonary manifestations and imaging. *Semin. Roentgenol.* **50**, 52–

64 (2015).

199. Almenoff, P. L., Johnson, A., Lesser, M. & Mattman, L. H. Growth of acid fast L forms from the blood of patients with sarcoidosis. *Thorax* **51**, 530–533 (1996).
200. Hulten, K. *et al.* In situ hybridization method for studies of cell wall deficient M . paratuberculosis in tissue samples. *Vet. Microbiol.* **77**, 513–518 (2000).
201. Alavi, H. A. & Moscovic, E. A. Immunolocalization of cell-wall-deficient forms of Mycobacterium tuberculosis complex in sarcoidosis and in sinus histiocytosis of lymph nodes draining carcinoma. *Histol. Histopathol.* **11**, 683–694 (1996).
202. Wall, S. U. E. *et al.* Identification of Spheroplast-Like Agents Isolated from Tissues of Patients with Crohn's Disease and Control Tissues by Polymerase Chain Reaction. *J. Clin. Microbiol.* **31**, 1241–1245 (1993).
203. Swidsinski, A., Loening-Baucke, V. & Herber, A. Mucosal flora in Crohn's disease and ulcerative colitis - An overview. *J. Physiol. Pharmacol.* **60**, 61–71 (2009).
204. Mattman, L. H., Tunstall, L. H., Mathews, W. W. & Gordon, D. L. L Variation in Mycobacteria. *Am. Rev. Respir. Dis.* **82**, 202–211 (1960).
205. Markova, N., Slavchev, G. & Michailova, L. Unique biological properties of Mycobacterium tuberculosis L-form variants: Impact for survival under stress. *Int. Microbiol.* **15**, 61–68 (2012).
206. Vettiger, A., Winter, J., Lin, L. & Basler, M. The type VI secretion system sheath assembles at the end distal from the membrane anchor. *Nat. Commun.* **8**, 1–9 (2017).
207. Joseleau-Petit, D., Liebart, J.-C., Ayala, J. A. & D'Ari, R. Unstable Escherichia coli L Forms Revisited : Growth Requires Peptidoglycan Synthesis. *J. Bacteriol.* **189**, 6512–6520 (2007).
208. Markova, N., Slavchev, G., Michailova, L. & Jourdanova, M. Survival of Escherichia coli under lethal heat stress by L-form conversion. *Int. J. Biol. Sci.* **6**, 303–315 (2010).
209. Klessen, C., Schmidt, K., Gumpert, J. & Grosse, H. Complete secretion of activable bovine prochymosin by genetically engineered L forms of Proteus mirabilis. *Appl. Environ. Microbiol.* **55**, 1009–1015 (1989).
210. Kujau, M. J., Hoischen, C., Riesenberg, D. & Gumpert, J. Expression and secretion of functional miniantibodies McPC603scFvDhlx in cell-wall-less L-form strains of Proteus mirabilis and Escherichia coli: A comparison of the synthesis capacities of L-form strains with an E. coli producer strain. *Appl. Microbiol. Biotechnol.* **49**, 51–58 (1998).
211. Kamariza, M. *et al.* Rapid detection of Mycobacterium tuberculosis in sputum with a solvatochromic trehalose probe. *Sci. Transl. Med.* **10**, 1–12 (2018).
212. Maitra, A. *et al.* Cell wall peptidoglycan in Mycobacterium tuberculosis: An Achilles' heel for the TB-causing pathogen. *FEMS Microbiol. Rev.* **43**, 548–575 (2019).
213. E Kuru, S Tekkam, E. H. Synthesis of fluorescent d-amino acids and their use for probing peptidoglycan synthesis and bacterial growth in situ.pdf.
214. Garcia-Heredia, A. *et al. Sidewall cell envelope synthesis and remodeling in pole-growing mycobacteria*. (2018) doi:http://dx.doi.org/10.1101/292607.

215. Mercier, R., Kawai, Y. & Errington, J. Excess membrane synthesis drives a primitive mode of cell proliferation. *Cell* **152**, 997–1007 (2013).
216. Erickson, H. P. & Osawa, M. Cell division without FtsZ - A variety of redundant mechanismsmmi. *Mol. Microbiol.* **78**, 267–270 (2010).
217. Imlay, J. A. The molecular mechanisms and physiological consequences of oxidative stress: Lessons from a model bacterium. *Nat. Rev. Microbiol.* **11**, 443–454 (2013).
218. Ransy, C., Vaz, C., Lombès, A. & Bouillaud, F. Use of H2O2 to cause oxidative stress, the catalase issue. *Int. J. Mol. Sci.* **21**, 1–14 (2020).
219. Hermann, C., Giddey, A. D., Nel, A. J. M., Soares, N. C. & Blackburn, J. M. Cell wall enrichment unveils proteomic changes in the cell wall during treatment of Mycobacterium smegmatis with sub-lethal concentrations of rifampicin. *J. Proteomics* **191**, 166–179 (2019).
220. Shannon, P. *et al.* Cytoscape: A Software Environment for Integrated Models of Biomolecular Interaction Networks. *Genome Res.* **13**, 2498–2504 (2003).
221. Bindea, G. *et al.* ClueGO: A Cytoscape plug-in to decipher functionally grouped gene ontology and pathway annotation networks. *Bioinformatics* **25**, 1091–1093 (2009).
222. Dejesus, M. A. *et al.* Comprehensive essentiality analysis of the Mycobacterium tuberculosis genome via saturating transposon mutagenesis. *MBio* **8**, (2017).
223. Slayden, R. A. & Barry, C. E. The role of KasA and KasB in the biosynthesis of meromycolic acids and isoniazid resistance in Mycobacterium tuberculosis. *Tuberculosis* **82**, 149–160 (2002).
224. Singh, V. *et al.* The inosine monophosphate dehydrogenase, GuaB2, is a vulnerable new bactericidal drug target for tuberculosis. *ACS Infect. Dis.* **3**, 5–17 (2016).
225. Nguyen, L. & Thompson, C. J. Foundations of antibiotic resistance in bacterial physiology: the mycobacterial paradigm. *Trends Microbiol.* **14**, 304–312 (2006).
226. Ongenae, V. *et al.* Reversible bacteriophage resistance by shedding the bacterial cell wall. *bioRxiv* 2021.11.17.468999 (2021).
227. Domínguez-Cuevas, P., Mercier, R., Leaver, M., Kawai, Y. & Errington, J. The rod to L-form transition of Bacillus subtilis is limited by a requirement for the protoplast to escape from the cell wall sacculus. *Mol. Microbiol.* **83**, 52–66 (2012).
228. Errington, J. Cell wall-deficient , L-form bacteria in the 21st century : a personal perspective. **0**, 287–295 (2017).
229. Ramijan, K. *et al.* Stress-induced formation of cell wall-deficient cells in filamentous actinomycetes. *Nat. Commun.* **9**, 1–13 (2018).
230. Pohane, A. A., Carr, C. R., Garhyan, J. & Swarts, B. M. Trehalose Recycling Promotes Energy-Efficient Biosynthesis of the Mycobacterial Cell Envelope. *MBio* **12**, 1–19 (2021).
231. Errington, J. L-form bacteria, cell walls and the origins of life. *Open Biol.* **3**, 1–7 (2013).
232. Jakimowicz, D. *et al.* Characterization of the mycobacterial chromosome segregation protein ParB and identification of its target in Mycobacterium smegmatis. *Microbiology* **153**, 4050–4060 (2007).

233. Ditse, Z., Lamers, M. H. & Warner, D. F. DNA replication in Mycobacterium tuberculosis. *Tuberc. Tuber. Bacillus Second Ed.* 581–606 (2017) doi:10.1128/9781555819569.ch27.
234. Botella, H. *et al.* Distinct Spatiotemporal Dynamics of Peptidoglycan Synthesis between Mycobacterium smegmatis and Mycobacterium tuberculosis. *Am. Soc. Microbiol.* **8**, 1–12 (2017).
235. Johnson, L. A. & Hug, L. A. Distribution of reactive oxygen species defense mechanisms across domain bacteria. *Free Radic. Biol. Med.* **140**, 93–102 (2019).
236. Hayashi, J. M. *et al.* Spatially distinct and metabolically active membrane domain in mycobacteria. **113**, (2016).
237. Hermann, C., Karamchand, L., Blackburn, J. M. & Soares, N. C. Cell Envelope Proteomics of Mycobacteria. *J. Proteome Res.* **20**, 94–109 (2021).
238. de Oliveira, M. C. B. & Balan, A. The atp-binding cassette (Abc) transport systems in mycobacterium tuberculosis: Structure, function, and possible targets for therapeutics. *Biology (Basel).* **9**, 1–25 (2020).